Dissertation

submitted to the
Combined Faculties of the Natural Sciences and Mathematics
of the Ruperto-Carola-University of Heidelberg, Germany
for the degree of
Doctor of Natural Sciences

Put forward by
Dipl.-Phys. Martin Laux
born in Wittlich

Oral examination: October 24th, 2017

Photoionization in strong laser fields:

from atoms to complex molecules

Fotoionisation in starken Laserfeldern: von Atomen zu komplexen Molekülen — In der vorliegenden Arbeit werden die Ergebnisse der Fotoionisation verschiedener Gase, insbesondere von Methan, in starken Laserfeldern vorgestellt. Die Fotoionisation wurde durch Fokussierung eines zweifarbigen Laserpulses in den Überschall-Gasstrahl eines Reaktionsmikroskops erreicht. Die Fähigkeit des Reaktionsmikroskops, gleichzeitig sämtliche geladenen Ionisationsprodukte zu detektieren und zu identifizieren, macht es möglich, den Ionisationsprozess kanal- und fragmentspezifisch zu analysieren. Die einstellbare relative Phase zwischen den beiden Komponenten des Zwei-Farben-Laserfelds ist ein weiterer Kontrollparameter für das Experiment. Die Diskrepanz in der Ausbeute niedrig-energetischer Elektronen bei Ionisationskanälen des Methans mit einem koinzident gemessenen, molekularen Ion einerseits und einem atomaren Ion andererseits ähnelt den Ergebnissen von Experimenten an molekularem Wasserstoff, die durch Autoionisation eines molekularen Rydberg-Zustands unter gleichzeitiger Abgabe von Vibrationsenergie erklärt werden konnten. Trotz des Mangels an Referenzdaten für Rydberg-Zustände von Methan mit höherer Anregung als $n = 6$ war es möglich, deren Energien abzuschätzen und es konnte für einen Ionisationskanal gezeigt werden, dass durch Autoionisation von Rydberg-Zuständen zwischen $n = 9$ und $n = 12$ freigewordene Elektronen die Ursache für die erhöhte Ausbeute niedrig-energetischer Elektronen sind.

Photoionization in strong laser fields: from atoms to complex molecules — In this thesis, the results of the strong-field photoionization of various gas targets, particularly of methane are presented. The photoionization was performed by focusing an ultrashort two-color laser pulse into the supersonic gas jet of a Reaction Microscope. The capability of the Reaction Microscope of simultaneous detection and identification of all charged ionization products enables the channel- and fragment-specific analysis of the ionization process. The tunable relative phase between both components of the two-color field is an additional control parameter for the experiment. The discrepancy in the yield of low-energy photoelectrons for methane ionization channels with a coincident molecular ion on the one hand and a coincident atomic ion on the other hand resembles similar results from experiments in molecular hydrogen, which could be explained by autoionization and simultaneous vibrational relaxation of a molecular Rydberg state. Despite the lack of reference data for Rydberg states of methane with excitations higher than $n = 6$, it was possible to estimate their energies and for one ionization channel, it could be demonstrated that electrons released by autoionization of Rydberg states between $n = 9$ and $n = 12$ are the origin of the enhanced low-energy electron yield.

List of Publications

Parts of this work have been published or prepared in the following references:

Y. Mi, N. Camus, L. Fechner, M. Laux, R. Moshammer, and T. Pfeifer.
Electron-Nuclear Coupling through Autoionizing States after Strong-Field Excitation of H$_2$ Molecules.
Phys. Rev. Lett. **118**, 183201 (2017).
(for additional information see [1])

C. Ott, A. Kaldun, L. Argenti, P. Raith, K. Meyer, M. Laux, Y. Zhang, A. Blättermann, S. Hagstotz, T. Ding, R. Heck, J. Madroñero, F. Martin, and T. Pfeifer.
Reconstruction and control of a time-dependent two-electron wave packet.
Nature **516**, 374–378 (2014).
(for additional information see [2])

C. Ott, A. Kaldun, P. Raith, K. Meyer, M. Laux, J. Evers, C. H. Keitel, C. H. Greene, and T. Pfeifer.
Lorentz Meets Fano in Spectral Line Shapes: A Universal Phase and Its Laser Control.
Science **340**, 716–720 (2013).
(for additional information see [3])

Further publications with own contributions:

A. Blättermann, C. Ott, A. Kaldun, T. Ding, V. Stooß, M. Laux, M. Rebholz, and T. Pfeifer.
In situ characterization of few-cycle laser pulses in transient absorption spectroscopy.
Opt. Lett. **40**, 3464–3467 (2015).
(for additional information see [4])

A. Kaldun, C. Ott, A. Blättermann, M. Laux, K. Meyer, T. Ding, A. Fischer, and T. Pfeifer.
Extracting Phase and Amplitude Modifications of Laser-Coupled Fano Resonances.
Phys. Rev. Lett. **112**, 103001 (2014).
(for additional information see [5])

P. Raith, C. Ott, K. Meyer, A. Kaldun, M. Laux, M. Ceci, C. P. Anderson, and T. Pfeifer.
Carrier-envelope phase-and spectral control of fractional high-harmonic combs.
J. Appl. Phys. **114**, 173102 (2013).
(for additional information see [6])

C. Ott, M. Schönwald, P. Raith, A. Kaldun, G. Sansone, M. Krüger, P. Hommelhoff,
Y. Patil, Y. Zhang, K. Meyer, M. Laux, and T. Pfeifer.
Strong-field spectral interferometry using the carrier-envelope phase.
New J. Phys. **15**, 073031 (2013).
(for additional information see [7])

P. Raith, C. Ott, C. P. Anderson, A. Kaldun, K. Meyer, M. Laux, Y. Zhang, and T. Pfeifer.
Fractional high-order harmonic combs and energy tuning by attosecond-precision split-spectrum pulse control.
Appl. Phys. Lett. **100**, 121104 (2012).
(for additional information see [8])

N. Camus, E. Yakaboylu, L. Fechner, M. Klaiber, M. Laux, Y. Mi, K. Hatsagortsyan,
T. Pfeifer, C. Keitel, R. Moshammer.
Experimental evidence for Wigner's tunneling time.
submitted (2017).

Contents

Chapter 1

Introduction

The interaction of matter with light is a fundamental phenomenon and plays a key role in many processes of our everyday life. It occurs in natural processes, such as photosynthesis [9], and important applications are for example material processing or even medical imaging and treatment [10, 11]. The interaction of ultraviolet (UV) light with biomolecules can lead to mutations in the genome and the process has been important for the development and the evolution of life on earth [12]. These examples illustrate how crucial it is to correctly understand and possibly control the underlying physics of light-matter interaction. The emergence of yet more and more advanced light sources in the past decades has opened many possibilities for research and applications and the development is still going on.

The invention of lasers (**L**ight **A**mplification by **S**timulated **E**mission of **R**adiation) [13] in the 1960s has revolutionized the field of atomic and molecular spectroscopy and lasers have become the working horse of many branches in this research area. The emergence of pulsed lasers with pulse durations down to a few femtoseconds ($1\,\mathrm{fs} = 10^{-15}\,\mathrm{s}$) [14] and intensities on the order of $10^{15}\,\mathrm{W\,cm^{-2}}$ or above made it possible to observe and make use of non-linear effects, such as high-order harmonic generation (HHG) [15]. With the help of HHG it has also become a standard procedure to create pulses in the attosecond ($1\,\mathrm{as} = 10^{-18}\,\mathrm{s}$) regime [16, 17]. The current world record for the shortest pulse is even shorter than $100\,\mathrm{as}$ [18]. This is the natural time scale of electrons in an atom. In the semi-classical Bohr model for example, the orbital period of the electron in the hydrogen atom circulating the proton on the first Bohr radius a_0 amounts to

$$\tau_0 = \frac{2\pi a_0}{\alpha c_0} = 1.52 \times 10^{-16}\,\mathrm{s} = 152\,\mathrm{as} = 6.28\,\mathrm{a.u.}\,, \tag{1.1}$$

where α and c_0 denote the fine-structure constant and the speed of light in vacuum. The unit symbol a.u. stands for the atomic unit system, which is related to the physical properties of the hydrogen atom and is often used in the atomic-physics community. A short

overview of the atomic unit system and how to convert the units into SI units is given in appendix A.

The fast development of high-performance light sources, with tabletop femtosecond laser systems on the one hand, and large-scale research facilities such as synchrotrons or free-electron lasers on the other hand, has also pushed the progress of technology to handle and to manipulate precisely the light beams. The latest optomechanical components allow for an accurate and controllable displacement with sub-micrometer precision (one micrometer is the distance that light travels during 3.3 fs).

With the appropriate femto- or attosecond light sources and suitable optomechanics at hand, it has become possible to observe in real-time atomic or molecular processes with unprecedented precision. The field of femtochemistry, which was pioneered by Ahmed Zewail in the late 1980s [19] and for which he was awarded the Nobel Prize in 1999, studies chemical reactions applying the methods of ultrafast laser spectroscopy. Chemical processes involve molecular vibrations and electron rearrangement as it occurs for example during the breaking of a bond [20]. Femtochemistry covers processes in a broad time scale from a few femtoseconds to hundreds of picoseconds [21] and ultrashort laser pulses are not only used for the observation of chemical reactions [22], but also for their active control. Manipulating the behavior of a specific atomic or molecular system under the influence of an intense laser field is the domain of coherent control [23]. So-called pulse shapers are able to transform a generic few- or multicycle laser pulse into a user-defined waveform, tailored to steer a quantum system from its initial state to a desired final state [24, 25]. By decomposing the initial pulse into its spectral components by a dispersive element, the pulse shaper can act individually on each frequency component by modulating its phase, amplitude, and sometimes also its polarization. After recombination of the spectrum, the pulse has a certain waveform, which can be optimized by a computer algorithm to maximize the yield of a desired reaction product [26]. Due to the simultaneous modification of various characteristics of the pulse, the spectral and temporal structure of the optimized pulses is usually not trivial to understand. A basic variant of pulse shaping is the limitation to just one control parameter. For a few-cycle pulse, this is very often the so-called carrier-envelope phase (CEP), the phase difference between the respective maxima of the pulse envelope and of the carrier oscillation (see e.g. [16]). The CEP has a strong influence on light-matter interaction because many processes show a nonlinear response to the electric field of the pulse. An example for this is the CEP-dependent asymmetric yield of photoelectrons parallel and antiparallel to the direction of the electric field of the laser. This quantity can also be used to measure the phase [27, 28] when it is not possible to actively control and stabilize it [29]. An asymmetric response is also possible for a pulse with more cycles by superimposing on it a second pulse with a different carrier frequency. This technique was used for this work, and the characteristic parameter of the resulting two-color waveform is the relative phase between the two overlapping pulses (cf. section 6.4). There are several spectroscopic approaches to investigate ultrafast light-matter interaction with a given target system. In transient absorption spectroscopy, the absorption spectrum as a function of the pump-probe delay between two ultrashort pulses is analyzed [9]. High-harmonic spectroscopy deals with the spectrum of high-order harmonics generated by a femtosecond pulse in the target system [30]. An-

other spectroscopy technique that is not just limited to light-matter interaction is cold target recoil ion momentum spectroscopy (COLTRIMS) [31, 32]. By means of COLTRIMS, the momenta of charged particles that are released during the ionization of a cold target gas by a projectile beam are analyzed in a so-called Reaction Microscope (Remi). Remis are extremely useful to treat different ionization channels separately. This is especially important for the ionization of molecules, which can involve a multitude of dissociation pathways.

Strong-field photoionization is explained mainly by tunneling according to the ADK theory [33], which is based on previous work by Keldysh [34]. The electron motion in the laser field after ionization is often described classically by the strong-field approximation [35] neglecting the Coulomb interaction between the released electron and the remaining ion. The Three-Step Model combines quantum-mechanical tunneling with classical electron trajectories in the laser field, and makes a statement about possible recollision processes, for example high-order harmonic generation [36]. There are a lot of theoretical and experimental studies on strong-field ionization of rare gases and simple diatomic molecules (see for example [37–40]), but very few about more complicated molecular systems. The study of simple systems is of course essential to test fundamental principles of strong-field physics, such as tunneling theory [41], and chemical bond breaking is best observed in a diatomic molecule [20, 22]. The motivation to investigate larger molecules are their additional degrees of freedom, which open the possibility for alternative, yet unknown or unobserved ionization pathways. For this thesis, the photoionization of methane was experimentally investigated. Methane is an interesting compound because it is the building block for any organic molecule, and so some findings in methane could also be used to understand the chemistry and physics of much larger biomolecules. One example could be the physics of DNA strand breaks, which are important for cancer therapy. It has been shown that they can be caused by electrons with kinetic energies below the ionization threshold [42]. Such electrons can easily be created by strong-field photoionization and general models that explain the creation of low-energy electrons from methane could possibly also be applicable to DNA molecules. Besides its importance for organic chemistry, the methane molecule has a unique electronic structure and molecular symmetry, which make it susceptible to Jahn-Teller distortions [43]. This gives rise to additional possibilities for electronic and vibrational excitation.

This work shall first give a theoretical background about the relevant physical phenomena that will play a role in the experimental part, especially the generation of second-harmonic light, and a general theory about strong-field photoionization. After that, the experimental setup as a combination of a high-performance laser system, high-precision optomechanics, and its key component, a state-of-the-art Reaction Microscope, is presented in detail. Finally, in the main part, the results of two-color photoionization measurements, focusing on the methane molecule, will be presented and discussed.

Chapter 2

Ultrashort laser pulses

The field of ultrafast atomic and molecular physics relies on the generation and propagation of extremely short and intense laser pulses. The experiments for this thesis were carried out with pulses of a duration of 25 to 30 fs generated by a commercial laser system. The spectrum of an electromagnetic wave is obtained by a Fourier transform of the field from time- to frequency domain, and vice versa. On that account, a continuous-wave (cw) system, such as the helium-neon laser [44], is ideally characterized by a single frequency or in practice by a very small spectral bandwidth, and can mathematically be considered as a pulse with infinite duration. The opposite to that is an extremely short, almost delta-like pulse, and the Fourier transform yields a broad spectrum. Modern femtosecond lasers are able to produce pulses which span more than one octave of the electromagnetic spectrum [45, 46]. The spectral width of a compressed pulse has direct implication on its propagation. Due to the frequency-dependent refractive index, the pulse will temporally broaden while traveling through air, and the broader the spectrum, the more dramatic is this effect. Another side-effect of this is the decrease of the peak intensity, which is maximum for the shortest possible pulse duration for a given spectral bandwidth. Such a pulse is also called a transform-limited pulse and it features a constant phase for all its spectral components. For experiments with ultrashort laser pulses, a basic knowledge about their generation is important, but also the understanding of propagation effects to be able to compensate for them if necessary, and this chapter is intended to give an overview of these topics.

2.1   Pulse Generation and mode locking

The invention of the laser [13] triggered a fast development of new technology and only a few years later, the first mode-locking techniques were introduced [47, 48]. Mode-locking refers to establishing a phase relation between the transverse resonator modes of a laser cavity [49] and until today, it is the main principle behind the generation of femtosecond pulses. For a given cavity of length L, the active longitudinal modes fulfill the equation [49]

$$v_n = \frac{nc_0}{2L},$$
(2.1)

where n is an integer to denote the index of the mode, and c_0 the vacuum speed of light. For simplicity, the refractive index is assumed to be equal to unity. The set of longitudinal modes, also called the frequency comb, consists of a multitude of modes separated by [50]

$$\delta v = v_{n+1} - v_n = \frac{(n+1)c_0}{2L} - \frac{nc_0}{2L} = \frac{c_0}{2L} = \frac{1}{\tau_{RT}},$$
(2.2)

with τ_{RT} being the cavity round-trip period. Apart from the constraints given by the cavity geometry, which are expressed by equation 2.1, the number of lasing modes is also limited by the characteristics of the gain medium. Since a broad spectrum is needed for short pulses, a femtosecond laser is characterized by an active medium with a broad gain profile. In the case of Ti:sapphire, the bandwidth of the amplification profile ranges from 650 nm to 1050 nm [51]. The final emission spectrum of the laser consists of the modes which are sufficiently amplified by the gain medium to lie above the laser threshold. The total electric field of all contributing modes at a fixed position within the laser cavity is given by [50]

$$E(t) = \sum_{n=0}^{N-1} E_n \sin\left[2\pi(v_0 + n\delta v)t + \varphi_n(t)\right],$$
(2.3)

where N is the total number of modes, E_n and $\varphi_n(t)$ are the amplitude and phase of the nth mode, and v_0 is the frequency of the lowest active mode. In general, $\varphi_n(t)$ is randomly fluctuating and the interference between the modes is also only random. This affects negatively the output power $P(t)$, which is proportional to $E^2(t)$. In order to have constructive interference of all modes at the same time, a linear phase relation $\varphi_n = n\alpha$ has to be established, which is the so-called mode-locking condition. Assuming that all modes have the same amplitude $E_n = E_0$ and setting α to zero simplifies equation 2.3 to [50]

$$E(t) = E_0 \sin\left[2\pi\left(v_0 + \frac{N-1}{2}\delta v\right)t\right] \frac{\sin(N\pi\delta vt)}{\sin(\pi\delta vt)}.$$
(2.4)

The electric field consists of a fast oscillation at the central frequency of the mode spectrum $v_c = v_0 + \frac{N-1}{2}\delta v$, and the envelope $|\sin(N\pi\delta vt)/\sin(\pi\delta vt)|$, which oscillates with $\delta v = \frac{1}{\tau_{RT}}$ [50]. The output power is obtained by averaging the fast oscillation:

$$P(t) = P_0 \left(\frac{\sin(N\pi\delta vt)}{\sin(\pi\delta vt)}\right)^2,$$
(2.5)

with P_0 being the average power of one wave. Equation 2.5 states that the power is periodically emitted in the form of a pulse with a period of τ_{RT}. Furthermore, the maximum power is proportional to N^2, the square of the number of locked modes: $P_{max} = N^2 P_0$. And finally, the pulse duration Δt decreases linearly with N and is approximately the inverse of the gain bandwidth $\Delta v = N \delta v$ [50]:

$$\Delta t \approx \frac{\tau_{RT}}{N} = \frac{1}{N \delta v} = \frac{1}{\Delta v}. \tag{2.6}$$

Over the past decades, several mode-locking techniques have been developed [52,53], and a frequently used method in modern Ti:sapphire laser systems is Kerr-lens mode locking [45,54]. This technique makes use of the optical Kerr effect, the intensity dependence of the refractive index n [55]:

$$n = n_0 + n_2 I, \tag{2.7}$$

where n_0 is the intensity-independent component, $n_2 I$ is the intensity-dependent component. I is the time-averaged intensity of the optical field. n_2 is in the order of $10^{-13}\,\mathrm{cm^2\,W^{-1}}$ to $10^{-17}\,\mathrm{cm^2\,W^{-1}}$ [55], so the effect plays only a role at high intensities. If a sufficiently intense laser pulse propagates through a medium, the Kerr effect will lead to a self-focusing of the beam [56]. As a consequence, for a beam with a gaussian profile, the center with highest intensity is more confined. The pulse duration is also reduced because the rising and falling edges of the envelope are less affected by the Kerr effect. The response time of the Kerr effect is in the femtosecond regime [57].

2.2 Propagation effects

When propagating along z through a dispersive medium, ultrashort pulses, especially those with a very broad spectrum, will accumulate a spectral phase

$$\varphi(\omega) = \frac{n(\omega)\omega}{c_0} z, \tag{2.8}$$

where $n(\omega)$ and c_0 denote the frequency-dependent refractive index and the speed of light in vacuum, respectively. As the carrier frequency ω_0 is usually large with respect to the spectral width of even a few-cycle pulse and because $n(\omega)$ is a sufficiently smooth function, it is possible to expand the spectral phase in a Taylor series [58]:

$$\varphi(\omega) = \varphi(\omega_0) + \underbrace{\left.\frac{\partial \varphi}{\partial \omega}\right|_{\omega_0} (\omega - \omega_0)}_{\text{GD}} + \underbrace{\frac{1}{2}\left.\frac{\partial^2 \varphi}{\partial \omega^2}\right|_{\omega_0} (\omega - \omega_0)^2}_{\text{GDD}} + \underbrace{\frac{1}{6}\left.\frac{\partial^3 \varphi}{\partial \omega^3}\right|_{\omega_0} (\omega - \omega_0)^3}_{\text{TOD}} + \mathcal{O}(\omega^4).$$

(2.9)

The first three orders are called the group delay (GD), group-delay dispersion (GDD) and the third-order dispersion (TOD). The GD is the retardation of the pulse maximum induced by the propagation through the optical medium. The (GDD) is the frequency-dependent fraction of the GD. Due to the GDD, the frequency components are delayed differently in time, which causes a linear temporal chirp of the pulse. A linearly chirped pulse is characterized by a linear increase or decrease of the carrier frequency in time, depending on the sign of the GDD. Higher-order chirps caused by the TOD and effects beyond the third order can play a role and have to be considered in certain situations [16]. In order to compensate for the usually positive dispersion, a negative dispersion has to be added artificially. To this end, various concepts relying on frequency-dependent optical path lengths have been developed. One of them is the prism compressor, in which the beam is spectrally split and recombined afterwards, with different pathways depending on the frequency before recombination [59]. Another possibility is the use of chirped mirrors, from which light is reflected by different layers, and in this case, the penetration depth into the mirror before reflection is wavelength-dependent [60].

Chapter 3

Second-harmonic generation

Nonlinear physics effects are visible whenever a medium, i.e. a single atom or a macroscopic object like a crystal exhibits a nonlinear response to a sufficiently intense external stimulation. In the case of optics and especially in atomic physics, this stimulation is usually the electric field of a laser. For this reason it is not surprising that most nonlinear effects have only been discovered after the invention of the laser in 1960 [13]. In fact, second-harmonic generation (SHG), the first nonlinear optics effect found with the help of lasers, was reported just one year later [61]. The principle of SHG shall be described here briefly as it was used in the experiments for this thesis.

The actual origin of SHG (but also higher-order effects) is the induced polarization in a medium when it is exposed to an intense electric field. In the classical (i.e. linear) case, the polarization can be expressed by (in SI units) [62]

$$P(t) = \varepsilon_0 \chi^{(1)} E(t),\qquad(3.1)$$

with ε_0 being the vacuum permittivity; $\chi^{(1)}$ is the so-called linear susceptibility. In the general (i.e. non-linear) case, the last equation 3.1 is extended to higher orders of the electric field:

$$P(t) = \varepsilon_0 \sum_n \chi^{(n)} E^n(t) = \varepsilon_0 \left[\chi^{(1)} E(t) + \chi^{(2)} E^2(t) + \chi^{(3)} E^3(t) + \dots \right]$$
$$= P^{(1)}(t) + P^{(2)}(t) + P^{(3)}(t) + \dots \qquad(3.2)$$

It should be mentioned here that the electric field is in general a vectorial quantity for which the $\chi^{(n)}$ become tensors. For the understanding of SHG, the relevant term is the second-order nonlinear polarization $P^{(2)}(t)$. If the electric field is given by
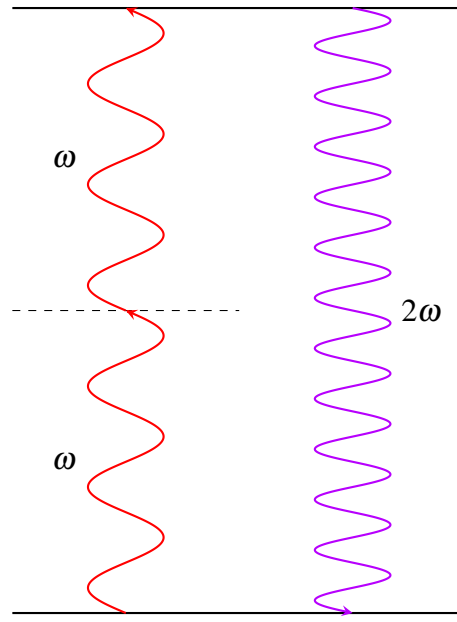
Figure 3.1: Schematic representation of second-harmonic generation: Two photons with frequency ω are absorbed while a single photon with double the initial frequency is reemitted by the medium.

$$E(t) = E_0 e^{-i\omega t} + \text{c.c.},\tag{3.3}$$

the second-order polarization is

$$P^{(2)}(t) = \varepsilon_0 \chi^{(2)} E^2(t) = 2\varepsilon_0 \chi^{(2)} E_0^2 + \left(\varepsilon_0 \chi^{(2)} E_0^2 e^{-2i\omega t} + \text{c.c.} \right).\tag{3.4}$$

This expression consists of two distinct terms: a constant term and an oscillatory term with the angular frequency 2ω. The constant part is related to a process known as optical rectification [63] in which a constant (DC) electric field is formed in the nonlinear medium. The oscillatory part can lead to SHG if the conditions are appropriate. For SHG it is absolutely essential to use a medium without a centrosymmetric crystal structure because $\chi^{(2)}$ vanishes identically in such media. Furthermore, the efficiency of SHG is strongly influenced by the wavevector mismatch Δk, which is given by

$$\Delta k = 2k(\omega) - k(2\omega).\tag{3.5}$$

Using the slowly varying amplitude approximation and assuming a weak second-harmonic conversion, i.e. a constant amplitude of the fundamental field $E(\omega)$ along the length L of the nonlinear medium, the SHG intensity varies with [64]

$$I(2\omega) = I_{\max}(2\omega) \left(\frac{\sin(\Delta k L/2)}{(\Delta k L/2)} \right)^2 = I_{\max}(2\omega) \operatorname{sinc}^2 \left(\frac{\Delta k L}{2} \right).\tag{3.6}$$
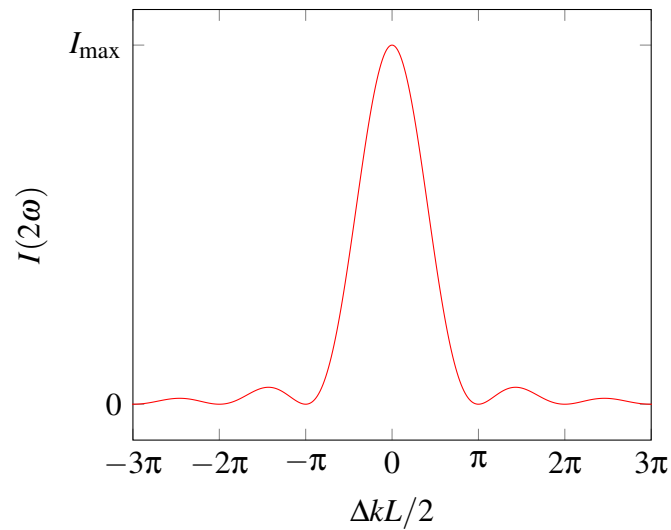
Figure 3.2: The intensity of the SHG signal as a function of $\Delta kL/2$ without depletion of the input intensity. The efficiency is strongly suppressed if the phase-matching condition $\Delta k = 0$ is not fulfilled (adapted from [64]).

This function is plotted in figure 3.2 and it clearly shows that the SHG conversion is efficient only if

$$\Delta k = 0, \tag{3.7}$$

which is known as the phase-matching condition.

Although the result from equation 3.6 is not the same for the situation with depletion of the input beam, for efficicient SHG it remains necessary that the phase-matching condition is fulfilled.

With the relation

$$k = \frac{n\omega}{c_0}, \tag{3.8}$$

the equation for the phase-matching condition in SHG writes as

$$0 = 2\frac{n(\omega) \cdot \omega}{c_0} - \frac{n(2\omega) \cdot 2\omega}{c_0}, \tag{3.9}$$

and can be simplified to

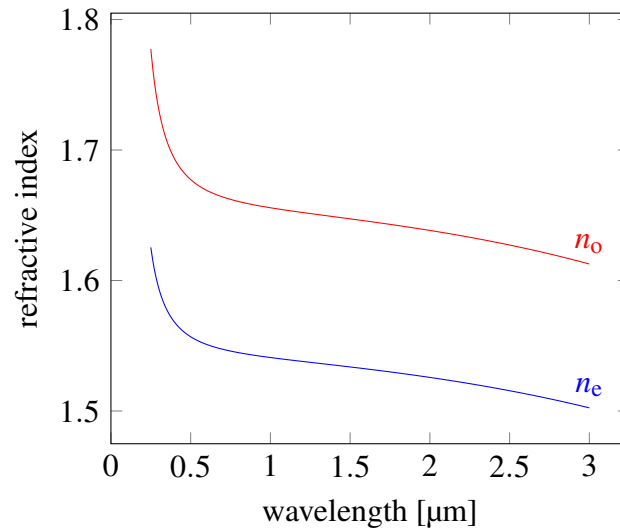$$n(\omega) = n(2\omega). \tag{3.10}$$

Figure 3.3: The ordinary and extraordinary refractive indices of β-BBO as a function of the wavelength calculated from Sellmeier coefficients taken from reference [66]

This equation looks almost trivial but in reality it is difficult to achieve because of the normal dispersion of the medium where the refractive index increases monotonically with the frequency. It would be possible to make use of anormal dispersion, which occurs close to absorption resonances, but the usual way to achieve phase matching is to exploit the birefringence properties of many crystals. In birefingent materials the refractive index depends also on the direction of polarization of the light wave. A typical medium used for SHG is β-barium borate (BBO), which is a negative uniaxial crystal. Uniaxial means that the optical properties of the crystal are characterized by one specific direction or axis, the so-called optical axis. Light that is polarized perpendicular to the optical axis is affected by the so-called ordinary refractive index n_o, light that is polarized parallel to the optical axis is influenced by the extraordinary refractive index n_e. In a negative uniaxial crystal, the birefringence given by

$$\Delta n = n_\mathrm{e} - n_\mathrm{o} \tag{3.11}$$

is negative. To achieve phase matching this means that the second-harmonic light has to have extraordinary polarization. The wavelength-dependent refractive indices can be calculated using empirically determined Sellmeier coefficients [65] and are displayed for β-BBO in figure 3.3. In a negative uniaxial crystal as β-BBO there are two possible schemes for phase matching. In type I, which was also used in the experiments described in chapter 6, both photons that are absorbed have the same polarization and the second-harmonic photon is perpendicularly polarized with respect to the fundamental ones. In type II, the polarizations of the two fundamental photons are orthogonal. The exact phase-matching condition from equation 3.10 can be achieved in two ways. In certain crystals, the birefringence is strongly temperature-dependent and by fine-tuning the crystal temperature, the phase-matching condition can be fulfilled (see for example reference [67]). A different approach is the angle-tuning method where the successful phase matching de-
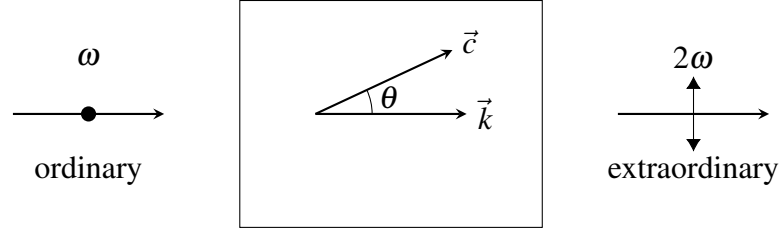
Figure 3.4: The geometric relations between the axes of polarization of the incoming fundamental (ω) and the outgoing SHG (2ω) beam, the wave vector $\vec{k}$ and the optical axis $\vec{c}$ of the crystal in the angle-tuning phase-matching method for a negative uniaxial crystal. The polarization of the incoming beam is perpendicular to the plane of projection, the polarization of the outgoing beam lies in the plane. The fundamental beam is always affected by the ordinary refractive index n_o, while the SHG beam is influenced by a mixture of n_o and n_e, which depends on the angle θ between $\vec{k}$ and $\vec{c}$ (adapted from [64]).

pends on the precise angular orientation of the crystal with respect to the optical axis. The angle θ is defined as the angle between the direction of the wave vector $\vec{k}$ of the incoming beam and the optical axis, commonly named $\vec{c}$. The beam that is polarized perpendicular to the plane spanned by $\vec{k}$ and $\vec{c}$ is influenced by n_o only, for all angles θ, as the polarization remains perpendicular to the optical axis. The beam with polarization in the plane is influenced by an effective refractive index, which is an angle-dependent mixture between n_o and n_e because the polarization vector can be decomposed in a fraction that is orthogonal and another fraction that is parallel to $\vec{c}$. The phase-matching condition in a uniaxial crystal like β-BBO with this effective refractive index is then

$$n_\mathrm{eff}(2\omega, \theta) = n_\mathrm{o}(\omega). \tag{3.12}$$

The effective refractive index is calculated according to the following formula [64]:

$$\frac{1}{n_\mathrm{eff}(\theta)^2} = \frac{\sin^2(\theta)}{n_\mathrm{e}^2} + \frac{\cos^2(\theta)}{n_\mathrm{o}^2}. \tag{3.13}$$

Combining equations 3.12 and 3.13 yields a solution for $\sin^2(\theta)$:

$$\sin^2(\theta) = \frac{\frac{1}{n_\mathrm{o}(\omega)^2} - \frac{1}{n_\mathrm{o}(2\omega)^2}}{\frac{1}{n_\mathrm{e}(2\omega)^2} - \frac{1}{n_\mathrm{o}(2\omega)^2}}. \tag{3.14}$$

This equation indicates the orientation of the nonlinear crystal in order to achieve phase matching. It does not necessarily have a solution, which means that under certain conditions, phase-matched SHG is impossible with the angle-tuning method. The geometry of angle-tuning phase-matching is displayed in figure 3.4.

Chapter 4

Strong-field photoionization

Photoionization in strong-field physics is quite different from the photoeffect described by Einstein already in 1905 [68]. In many cases ionization is not possible by the absorption of a single photon because the photon energy of the laser is smaller than the ionization potential of the target. There are two different pictures to describe strong-field photoionization, namely multiphoton ionization (MPI) and tunneling ionization. Multiphoton ionization is the simultaneous absorption of several photons to overcome the ionization barrier. Tunneling ionization can occur when the electric field of the laser distorts the Coulomb potential of the target atom such that the bound electron can tunnel through the bent potential. A special case of tunneling ionization is over-the-barrier ionization (OTBI), which occurs at such high intensities that the atomic potential is so extremely bent that the ground state of the atom is no longer bound. The electron is then able to leave the atom without even having to tunnel. The critical intensity for OTBI of hydrogen for a low-frequency laser field is $1.4 \times 10^{14}\,\mathrm{Wcm^{-2}}$ [69]. In his theory, Keldysh showed that both pictures, MPI and tunneling ionization, are effectively describing the same phenomenon and he introduced the parameter γ to indicate which of the two processes is predominant [34]. The parameter is given by the ratio between the laser frequency ω and the tunneling frequency ω_T, i.e. the inverse of the time the electron has to tunnel. For a laser with frequency ω and an electric field amplitude E_0, γ is defined as

$$\gamma = \frac{\omega}{\omega_\mathrm{T}} = \omega\sqrt{\frac{2I_\mathrm{P}}{I}} = \sqrt{\frac{I_\mathrm{P}}{2U_\mathrm{P}}},\tag{4.1}$$

where I_P is the ionization potential and $U_\mathrm{P} = \frac{E_0^2}{4\omega^2}$ is the ponderomotive energy, the quiver energy of the electron due to its oscillatory motion in the field [69]. In the case of $\gamma \ll 1$, with a relatively slow oscillation of the field, tunneling is the significant process. For $\gamma \gg 1$ the multiphoton picture yields a better description of the process. In the intermediate region at $\gamma \approx 1$, a clear statement about the main process is impossible. The two different pictures are displayed in figure 4.1. Different aspects and theoretical concepts of strong-field light-matter interaction will be explained in more detail in the following paragraphs.
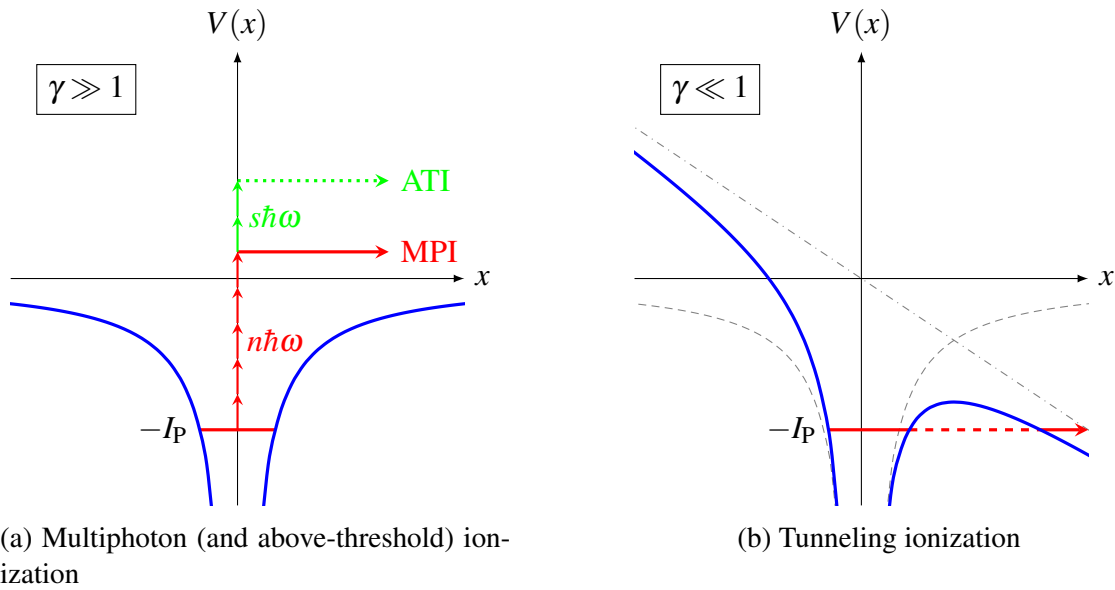
(a) Multiphoton (and above-threshold) ion-
ization

(b) Tunneling ionization

Figure 4.1: Illustration of multiphoton (a) and tunneling (b) ionization. In the MPI picture,
several photons are simultaneously absorbed to overcome the ionization threshold. ATI
stands for above-threshold ionization, the absorption of additional photons, which leads to
a higher kinetic energy of the free electron. In the tunneling picture, the binding Coulomb
potential is distorted by the laser field and the electron can tunnel through a finite barrier
into the continuum.

4.1   Multiphoton ionization

As already mentioned earlier, MPI is the simultaneous absorption of n photons with
$n\hbar\omega \geq I_P$. This leads to the transition of an electron from a bound state to a free (contin-
uum) state. The ionization rate is given by [69, 70]

$$\Gamma_n = \sigma_n I^n. \tag{4.2}$$

σ_n is a generalized cross section including higher-order perturbation terms making it
rather difficult to calculate. A special case of multiphoton absorption is above-threshold
ionization (ATI) [70, 71]. In this process more photons than needed to overcome the ion-
ization threshold are absorbed. ATI can be identified in the kinetic-energy spectrum of
the ejected electrons by discrete peaks at intervals of the photon energy. The ionization
rate of ATI is given by

$$\Gamma_{n+s} = \sigma_n I^{n+s}, \tag{4.3}$$

and the energy of the electron in the continuum is

$$E_{\text{el}} = (n+s)\hbar\omega - I_{\text{P}}^{*}. \tag{4.4}$$

$I_{\text{P}}^{*} \approx I_{\text{P}} + U_{\text{P}}$ is the modified ionization potential due to ponderomotive or AC-Stark shifts of the atomic levels [72, 73].

4.2 Tunneling ionization

According to Keldysh's theory, for $\gamma \ll 1$, i.e. a relatively high intensity and a comparably slow field oscillation, tunneling is the essential ionization mechanism. Due to the low oscillation frequency, it is allowed to treat the process in a quasi-stationary approximation [69]. The intense laser field distorts the atomic potential in such a way that a finite potential barrier is created for bound electrons which they can tunnel through. At the peak of the electric field the length of the barrier is shortest and the tunneling probability is highest. By expanding Keldysh's theory, theorists developed an expression for the tunneling rate [33, 74–77], the well-known ADK rate, named after the authors of the 1986 publication [33]. The rate for ionization by linearly polarized light from an atomic state characterized by its principal, azimuthal and magnetic quantum numbers n, l, and m (and under the conditions that $l \ll n$ and $n \gg 1$) is given by

$$\Gamma_{\text{ADK}} = \sqrt{\frac{3En^{*3}}{\pi Z^3}} \frac{Z^2}{4\pi n^{*3}} \left(\frac{2e}{n^*}\right)^{2n^*} \frac{(2l+1)(l+|m|)!}{2^{|m|}(|m|)!\,(l-|m|)!}$$
$$\times \left(\frac{2Z^3}{En^{*3}}\right)^{2n^*-|m|-1} \exp\left(-\frac{2Z^3}{3n^{*3}E}\right), \tag{4.5}$$

with the electric field of the laser E, the charge of the remaining ion Z and the effective quantum number $n^* = Z/\sqrt{2I_{\text{P}}}$. In the case of ionization from an $l=1$ state, the comparison of the rates between $m=0$ and $|m|=1$ yields

$$\frac{\Gamma_{m=0}}{\Gamma_{|m|=1}} = \frac{2Z^3}{En^{*3}} = \frac{2}{E}(2I_{\text{P}})^{\frac{3}{2}} \gg 1, \tag{4.6}$$

which means that ionization occurs preferentially from the $m=0$ orbital.

4.2.1 Classical trajectories and the Three-Step Model

Although the process of photoionization is a quantum process, a classical or semiclassical treatment of the electron's trajectory once it has been ionized often yields a good agreement with experimental results. An additional simplification can be reached by ignoring

the Coulomb interaction between the electron and the field of the remaining ion. The idea of omitting the electron-ion interaction is the key concept of the strong-field approximation (SFA) (see for example [35, 78]). It is justified for a sufficiently intense laser field because the electron is quickly accelerated to regions where the Coulomb field is negligible in comparison to the laser field. By neglecting the Coulomb interaction (and also the magnetic component of the laser field), the equation of motion of the quasi-free electron is

$$\frac{\mathrm{d}\vec{p}(t)}{\mathrm{d}t} = -\vec{E}(t). \tag{4.7}$$

Integration from the moment of ionization t_0 to a later time t yields the kinetic momentum

$$\vec{p}(t) = -\int_{t_0}^{t} \vec{E}(t')\,\mathrm{d}t'. \tag{4.8}$$

The initial momentum $\vec{p}_0 = \vec{p}(t_0)$ is assumed to be $\vec{0}$ [36, 79, 80] although this assumption has been under debate [81, 82]. The electric field $\vec{E}$ is related to the vector potential $\vec{A}$ by

$$\vec{E}(t) = -\frac{1}{c_0}\frac{\partial}{\partial t}\vec{A}(t). \tag{4.9}$$

Here, c_0 denotes the vacuum speed of light. Integration of 4.8 using 4.9 yields

$$\vec{p}(t) = -\frac{1}{c_0}(\underbrace{\vec{A}(t_0)}_{\text{time-independent}} - \underbrace{\vec{A}(t)}_{\text{time-dependent}}). \tag{4.10}$$

The first, time-independent term in equation 4.10 is the drift term, the second, time-dependent term is the so-called quiver term. Equation 4.10 makes only sense as long as the electron does not interact any further with the remaining ion. Depending on the phase of the laser field at the moment of birth, the free electron will follow different trajectories. For some phases, the electron is constantly driven further away from the residual ion while for other phases, it is driven back to recollide with the ion, which leads to additional effects that will be discussed in the next section. In the case of a non-recolliding trajectory, the momentum of the electron after a long time $t \rightarrow \infty$ can be deduced from 4.10:

$$\vec{p}(\infty) = -\frac{1}{c_0}(\vec{A}(t_0) - \vec{A}(\infty)) = -\frac{1}{c_0}\vec{A}(t_0). \tag{4.11}$$

$\vec{A}(\infty)$ is omitted because the vector potential is usually defined such that it vanishes for long times before and after the laser pulse, i.e. $\lim_{t\to\pm\infty} \vec{A}(t) = \vec{0}$. The momentum measurement in the experiments for this thesis is based on time-of-flight spectroscopy in the order of nano- or microseconds. Compared to the timescale of ultrashort laser pulses, the attosecond or femtosecond regime, this is nearly an infinite time and equation 4.11 implies that after such a long time, the momentum of the electron is proportional to the vector potential at the moment of ionization [83]. This is only the drift momentum and it depends on the phase of the laser field at the moment of ionization [84]. Equation 4.11 allows also to calculate the final kinetic energy by $E_{\text{kin}}(\infty) = \frac{\vec{p}(\infty)^2}{2}$. For a sinusoidal field it is straightforward to show that the maximum kinetic energy is [85]

$$E_{\text{kin}_{\text{max}}} = 2U_\text{P}. \tag{4.12}$$

This relation is very useful because it connects the kinetic energy spectrum of the photo-electrons to the ponderomotive potential of the laser field, which allows for an estimate of the intensity of the laser field.

 The opposite case, the case of recollision with the parent ion at a time t_{rec} after ionization at t_0, occurs if the following equation is fulfilled (the ion position is assumed to be at the origin):

$$\vec{x}(t_{\text{rec}}) = \int_{t_0}^{t_{\text{rec}}} \vec{p}(t)\,\mathrm{d}t = -\frac{1}{c_0}\left(\vec{A}(t_0)(t_{\text{rec}} - t_0) - \int_{t_0}^{t_{\text{rec}}} \vec{A}(t)\,\mathrm{d}t\right) = \vec{0}. \tag{4.13}$$

The process of ionization and recollision is described by the semi-classical Three-Step Model proposed by Corkum in 1993 [36]. In the first step, the electron tunnels through the distorted Coulomb potential and appears at the tunnel exit with zero kinetic energy (see figure 4.1b). In the second step, the electron is accelerated by the electric field of the laser pulse. The interaction between the free electron and the laser field is treated completely classically in the Three-Step Model, in contrast to the tunneling process, which has to be treated quantum-mechanically. In the last step, the electron recollides with its parent ion. Figure 4.2 shows how the electric field and the vector potential are linked and how the phase of the laser field at the moment of ionization determines the trajectory of the electron. The recollision energy also varies depending on the moment of ionization (figure 4.3). At the moment of recollision, the kinetic energy of the electron is [83]

$$E_{\text{kin}}(t_{\text{rec}}) = \frac{\vec{p}(t_{\text{rec}})^2}{2} = \frac{1}{2{c_0}^2}(\vec{A}(t_0) - \vec{A}(t_{\text{rec}}))^2. \tag{4.14}$$

In a cosine-shaped field with the maximum at $\omega t = 0$ the recollision energy is maximized for electrons that are tunnel-ionized at a phase of $\omega t \approx 0.30\,\text{rad}$. The maximum kinetic energy of the recolliding electron amounts approximately to 3.17 times the ponderomotive potential U_p [36] (see figure 4.3). Recollision energies below that maximum can always be reached by two different trajectories, often called the long and the short trajectories.
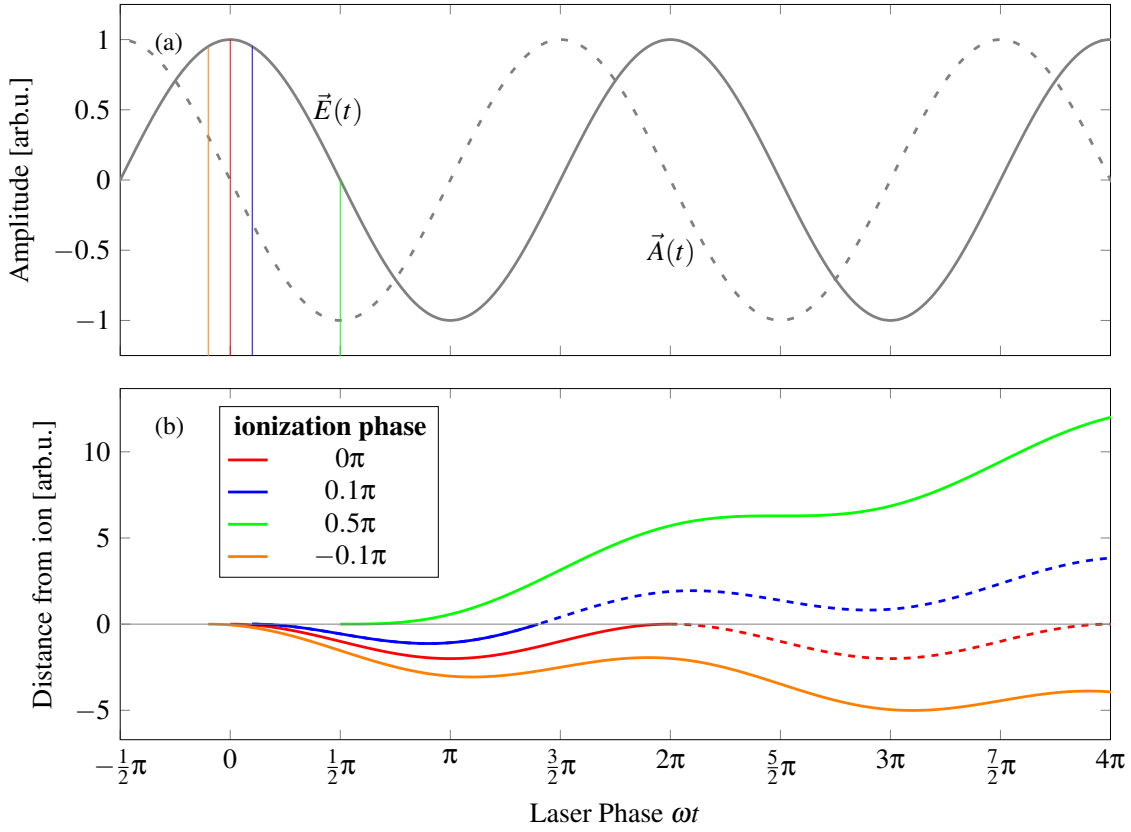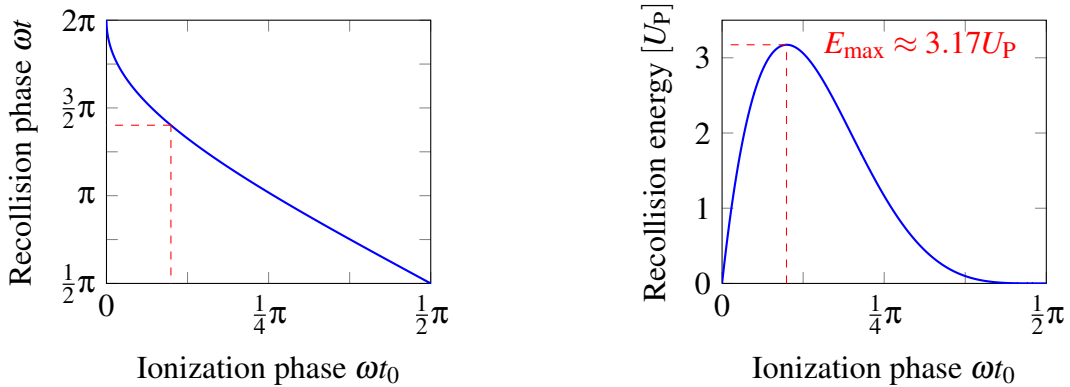
Figure 4.2: Influence of the moment of ionization on the trajectory of the electron. In (a) a cosine-shaped electric field and the corresponding vector potential are displayed for a few oscillation cycles. The colored lines refer to the moments of ionization of the classical trajectories shown in (b). Only electrons that are ionized between an extremum and the next zero crossing of the electric field are recolliding with the ion within the next step of 2π. The green trajectory is drifting away fastest but this statement is rather hypothetical because it corresponds to a vanishing initial electric field where the probability for tunneling is zero as well. The dashed lines indicate the probability of the electron to continue its trajectory without interacting with the ion.

It can be shown that the electron does not return to the ion with circularly polarized light and thus recollision does not play a role under these circumstances [36]. In the moment of recollision, several different scenarios are possible. The electron could for instance recombine into the ground state, which is accompanied by the emission of a high-energy photon ($E_\gamma = E_{rec} + I_P$). This is the principle of high-harmonic generation (HHG), the key process in the generation of ultrashort pulses in the attosecond regime [86]. A second possible recollision process is elastic scattering of the electron from the ion. This will change the momentum spectrum of the electron significantly, boosting it to kinetic energies of up to $10U_P$, the so-called high-order ATI [80]. Multiple ionization is the result of inelastic scattering in the recollision process, leading for example to nonsequential double ionization (NSDI) [78, 83]. By far, the most likely recollision process is however that the electron continues its trajectory without undergoing any of the aforementioned options because the cross sections for any of them are very small. In this case, the electron

(a) Laser phase at the moment of recollision for ionization at ωt_0

(b) Recollision energy as function of the ionization phase ωt_0

Figure 4.3: Influence of the phase of the cosine-shaped electric field at the moment of ionization on the laser phase (a) and on the kinetic energy of the electron (b) when it recollides. Recollision only occurs for ionization between an extremum of the electric field and the following zero crossing, i.e. a phase between 0 and $\frac{1}{2}\pi$ or between π and $\frac{3}{2}\pi$ in a cosine field. The maximum recollision energy amounts to approximately 3.17 times the ponderomotive potential for ionization at a phase of $\approx \frac{1}{10}\pi$ after the field maximum. This particular case is represented by the red dashed lines. All other recollision energies can be obtained from two different recolliding trajectories.

might even return to the ion several times (see the dashed lines in figure 4.2b).

4.3   Photoionization of molecules

To understand the photoionization of molecules, not only the electronic, but also the vibrational structure of the molecule has to be taken into account. Furthermore, the outcome of the ionization process is much more versatile than in atomic ionization because the molecule can break up afterwards into several charged or neutral fragments or stick together. A simple but intuitive two-step model to describe the dissociative ionization of D_2 is presented in [37]. In the first step, the D_2 molecule is ionized by the laser field and promoted to the ground state of the D_2^+ ion. The dissociation occurs in the second step by further interaction with the laser (see figure 4.4). The mechanism described by the two-step model is a general one and so the model can be used for other molecules if a stable configuration of the singly charged ion after the first step exists. Nevertheless, in the first step, which is relevant for the actual ionization, the model ignores the characteristics of molecules that distinguishes them from atoms, namely the possibility for vibrational or rotational excitation. We will see in the experimental part of this thesis that some findings about molecular photoionization cannot be explained by the two-step mechanism and that new models and mechanisms have to be developed.
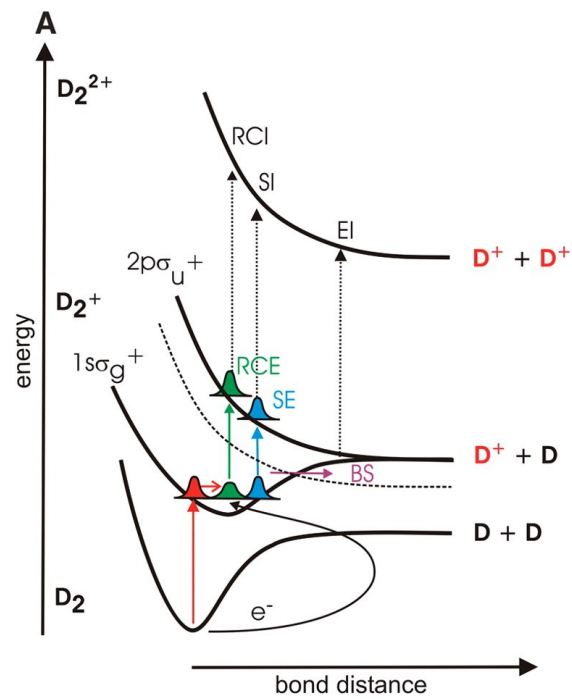
Figure 4.4: Illustration of the two-step model to describe the dissociative photoionization of D_2. After ionization in the first step, the D_2^+ ion further interacts with the laser field in the second step, which leads to dissociation, either with one neutral D atom and a D^+ ion or by Coulomb explosion and two D^+ ions. Taken from [37].

Chapter 5

The Methane Molecule

The experiments done in the framework of this thesis focus on the interaction of ultrashort two-color laser pulses with target atoms and small molecules with a certain symmetry. One goal was to see how systems with a different symmetry respond to the interaction with an asymmetrically shaped laser pulse. A large part of this thesis is dedicated to the methane molecule (CH_4). Methane is of particular interest because it is the simplest hydrocarbon molecule and fragments of the methane molecule are the key constituents of long-chain organic molecules. Those organic molecules comprise amino acids and proteins, the essential components for life on earth, as well as industrial products as for example synthetic polymers. It is important for astrobiologists because CH_4 was a key constituent of the early earth's atmosphere [87], and it is also found in the atmosphere of the Saturn moon Titan [88], a candidate for (primitive) extraterrestrial life. By simulating Titan's atmospherical conditions, it was possible to form certain basic amino acids and nucleotide bases [89]. Nowadays, methane is an important contributor to the climate change caused by the greenhouse effect: indirectly because it is a main constituent of natural gas that is used for fossil energy production with carbon dioxide (CO_2) as waste-product; and directly because the CH_4 molecule has an even higher greenhouse potential than CO_2, however its concentration in the atmosphere is lower. An overview of different greenhouse gases can for example be found in reference [90]. The CH_4 molecule is consisting of a carbon atom in the center and four hydrogen atoms located on the corners of a tetrahedron around the carbon center. This tetrahedral symmetry is also interesting with respect to the phase-dependent broken symmetry of the two-color laser field. The tetrahedral geometry can intuitively be understood by hybridization of the valence orbitals of the carbon atom [91]. In the ground state of the C atom, the 2s orbital, which is energetically a little lower than the three degenerate 2p orbitals, is occupied by two electrons and two 2p orbitals are occupied by one electron each. In this configuration, the formation of four covalent bonds is not possible, because there are only two unpaired electrons. In the hybridization picture, the 2s and all three 2p orbitals mix together, which results in four singly populated sp^3 hybrid orbitals with equal energy in tetrahedral orientation. The methane molecule is the result of the overlap of each sp^3 orbital with a 1s hydrogen orbital. Although the hybridization model is able to explain the molecular geometry, it fails to explain experimental results about the electron binding energies [92–95]. According to
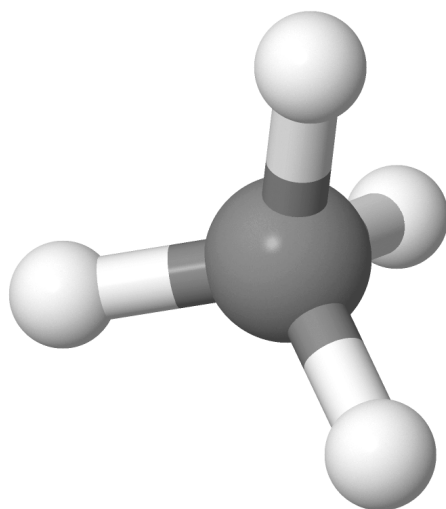
Figure 5.1: The methane molecule with a carbon atom in the center and four hydrogen atoms in the corner points of a tetrahedron

hybridization theory, there should be two different ionization potentials, i.e. one for ionization from the inner 1s-like orbital of the C atom and another one for ionization from the fourfold degenerate sp^3 hybrid orbitals shared between the carbon and hydrogen atoms. In reality, besides the predicted inner-shell energy level, which is usually termed as $1a_1$, there are two levels in the valence shell. Similar to the 2s and three degenerate 2p levels of the C atom, in methane there are the $2a_1$ valence orbital with a binding energy of ~ 23 eV, and the triply degenerate $1t_2$ levels with ~ 14 eV [94]. The three $1t_2$ orbitals form the highest occupied molecular orbital (HOMO). In the common notation, the electron configuration of the methane groundstate is $(1a_1)^2(2a_1)^2(1t_2)^6$. This looks very similar to the neon configuration $(1s)^2(2s)^2(2p)^6$. Since there are two valence energy levels, the state of the CH_4^+ ion is different depending on the orbital from which an electron is removed. The two cation states are usually called $(2a_1)^{-1}$ and $(1t_2)^{-1}$, respectively, named after the orbitals that lack one electron. Alternatively, the terminology is A for the former and X for the latter cation state [96]. As the X state is created by ionization from the HOMO, it is the CH_4^+ ground state. The X state is of particular interest because of the triple degeneracy of the $1t_2$ orbital. When an electron is removed from the HOMO the remaining CH_4^+ ion in the X state will immediately be subject to the Jahn-Teller effect [43], which will distort the ion to reduce its tetrahedral symmetry T_d and lift the degeneracy [97]. Several experimental and theoretical studies were dedicated to the geometry and the vibrational structure of the CH_4^+ ion in the X state [97–103] and there is a debate about its actual symmetry. The C_{2v}, C_{3v} and D_{2d} have been reported and some groups reported that the symmetry of the ground state of the methane cation is C_{2v} [99–102], others claim that it is D_{2d} [97, 103]. The shape of the cation in the three symmetry states is depicted in figure 5.2. The interpretation of the experimental results in chapter 7 will rely on references [97, 103], which suggest D_{2d} symmetry for the ground state of CH_4^+. Rabalais *et al.* showed that in the Franck-Condon approximation, ionization from the methane ground
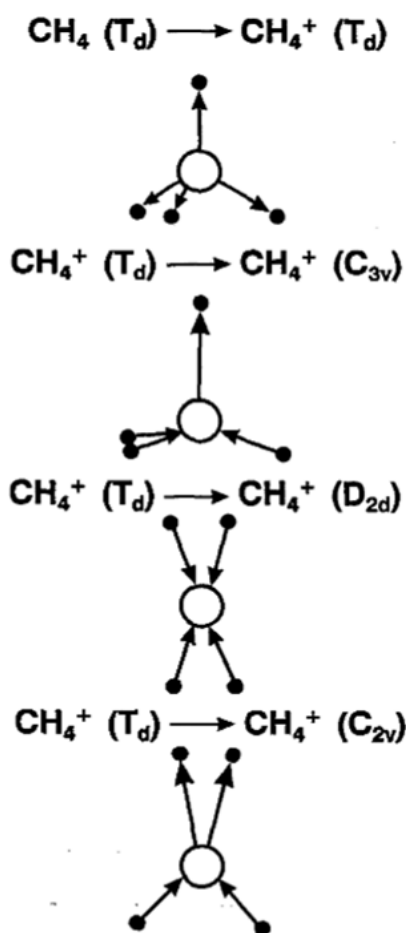
CH_4 (T_d) $\longrightarrow$ CH_4^+ (T_d)

CH_4^+ (T_d) $\longrightarrow$ CH_4^+ (C_{3v})

CH_4^+ (T_d) $\longrightarrow$ CH_4^+ (D_{2d})

CH_4^+ (T_d) $\longrightarrow$ CH_4^+ (C_{2v})

Figure 5.2: Schematic of the CH^+ ion in different symmetric arrangements caused by Jahn-Teller distortion (taken from [102]). The molecular ground state has tetrahedral symmetry T_d, the cation can have energetically different configurations which can be distinguished by their respective symmetry (C_{3v}, D_{2d} and C_{2v}).

state automatically leads to a vibrationally excited state of the CH_4^+ ion [97] due to the different equilibrium positions under influence of the Jahn-Teller effect. The effect is also triggered if a $1t_2$ electron is excited to a Rydberg state. The vibrational level structure of the ionic CH_4^+ core in a Rydberg state is nearly the same as of the bare CH_4^+ cation. Due to the simultaneous vibrational excitation, the total energy of the Rydberg system can be higher than the ionization potential of the molecule. There are several possible Rydberg series converging to the different excitation levels of the CH_4^+ ion. In each Rydberg series, the symmetry of the ion core corresponds to the symmetry of the excited ion state to which the series converges [103]. In experiments with methane, Rydberg and doubly excited states have been detected [93, 96, 104–106], and also autoionization with ejection of low-energy electrons with about $20\,meV$ has been reported [107].

Chapter 6

Experimental Setup

This chapter about the experimental setup used in the measurements for this thesis consists of five sections. The first section deals with the laser source for the generation of femtosecond pulses. It is followed by a description of the beam path, which includes a Mach-Zehnder interferometer and a setup for second-harmonic generation. The largest part is dedicated to the so-called Reaction Microscope (Remi) [31, 32, 108], a coincidence spectrometer to analyze the momenta of charged particles that are produced in certain reactions. The key components of the Reaction Microscope and also the mathematical methods for the momentum reconstruction will be discussed. The reconstructed momenta are also used to assign a two-color phase value to each detected ionization event. And lastly, the setup of a beamline for high-harmonic generation, which was built in cooperation with the university of Frankfurt, will be shown.

6.1   The Femtosecond Laser System

The femtosecond laser used for the experiments of this thesis is a commercial 'FEMTOPOWER compact PRO HP/HR' system by *Femtolasers*, which is schematically depicted in figure 6.1. The active medium is a Ti:sapphire crystal, i.e. a sapphire (Al_2O_3) crystal doped with Ti^{3+} ions. General information about this type of pulsed lasers can for example be found in refs. [53, 110]. Due to the excellent properties of Ti:sapphire, especially its large gain bandwidth, these lasers are the most frequently used sources of femtosecond pulses. The particular FEMTOPOWER system produces ultrashort pulses with a duration below 10 fs in a mirror-dispersion-controlled Ti:sapphire oscillator [111] pumped at 532 nm by a 3 W-Nd:YVO laser. The bandwidth of the oscillator pulses is about 250 nm at a central wavelength of 780 nm. The oscillator operates at high repetition rate (80 MHz), but the energy per pulse is in the order of only a nanojoule [109]. Both for ionization and second-harmonic generation, this is not sufficient, and for this reason, the pulse energy is boosted by chirped-pulse amplification [112]. This occurs in a subsequent multi-pass Ti:sapphire amplification stage, after the pulses have been temporally
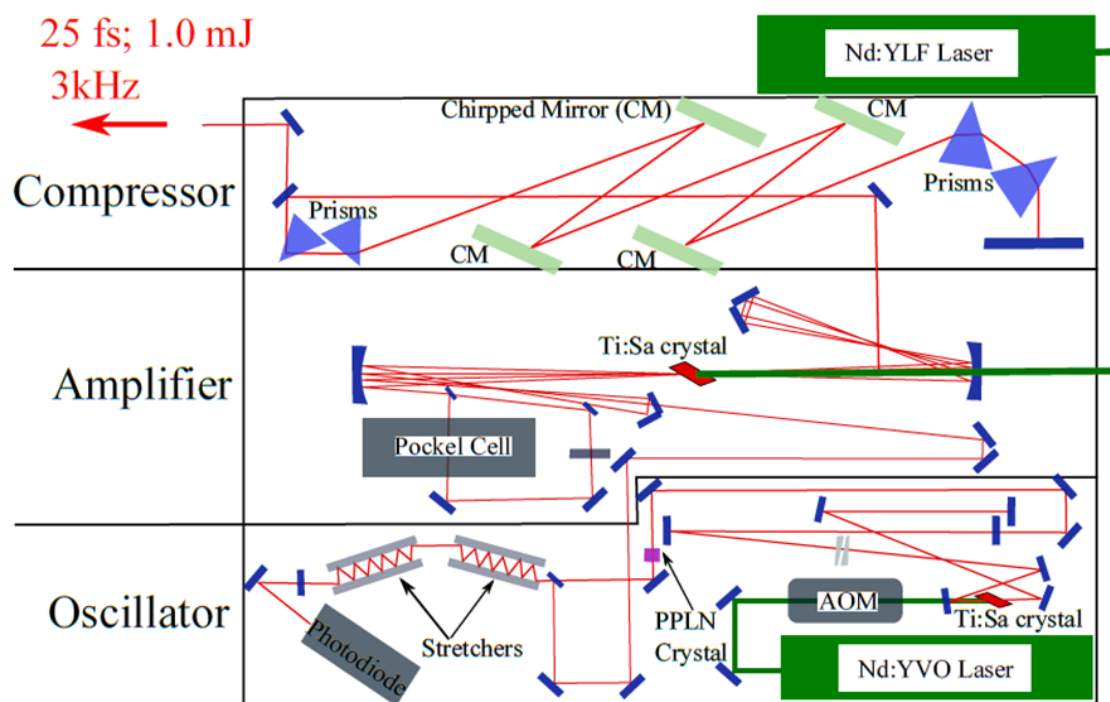
Figure 6.1: Schematic of the femtosecond laser system used during the experiments for this thesis (taken from [109]).

stretched. The stretching is necessary to reduce the peak power to protect the amplifying crystal from damage. The amplifier is pumped by a Nd:YLF laser at 527 nm with an average power of 30 W. After passing four times through the crystal, most of the pulses are sorted out by a Pockels cell, which reduces the repetition rate to 3 kHz. The remaining pulse passes five more times through the gain medium and after that, it is temporally compressed again by a combined prism and chirped-mirror compressor, which also corrects some dispersion effects [113]. The output pulses have an energy of 800 to 1000 μJ and a pulse duration of less than 30 fs. These pulses follow the beam bath described in the next section. In principle, it is possible to reduce the pulse duration to less than 10 fs by making use of self-phase modulation (cf. ref. [56]) in a gas-filled hollow-core fiber and a subsequent chirped-mirror compressor [114]. This was not done for the experiments of this thesis and will not be further explained here, but the necessary setup is described for example in [58].

6.2 Beam Path

The laser pulses provided by the commercial laser system are in the visible to near-infrared spectral regime with a center wavelength of about 800 nm and a pulse duration of about 25 fs. In order to form a phase-tunable two-color pulse, a Mach-Zehnder interferometer is used, whose principle is described in the following part. After leaving the
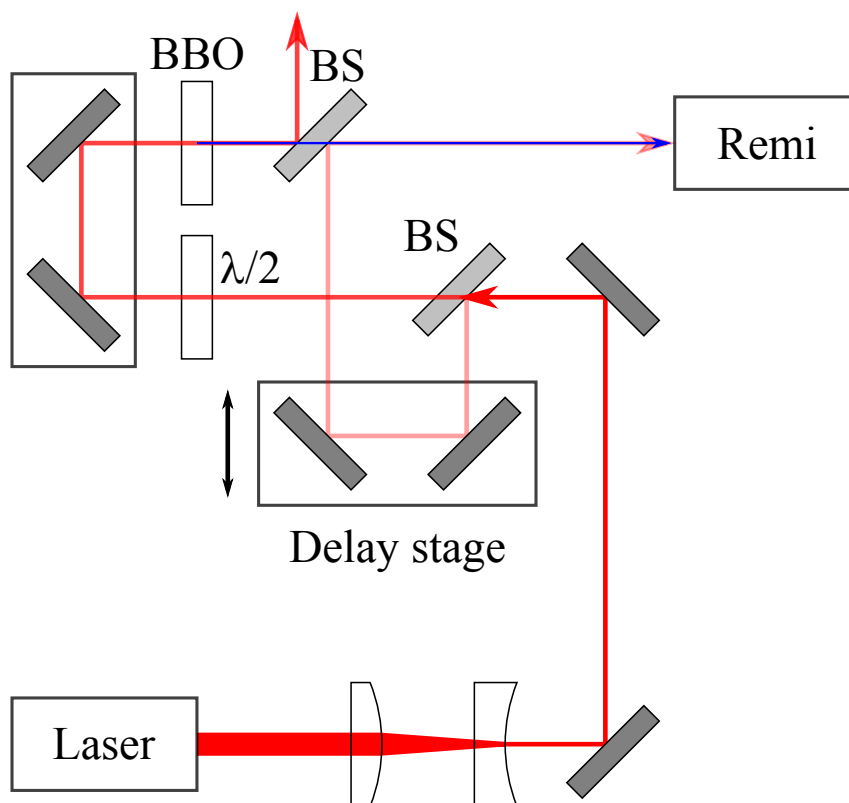
Figure 6.2: schematic of the beam path from the laser housing to the reaction microscope; normal mirrors are displayed in dark gray, beamsplitters in light gray

laser system, the infrared pulse follows the beam path depicted in figure 6.2. In the first step, the diameter of the collimated beam is reduced to a fifth of the original size by a two-lens telescope. The reduction of the beam diameter is necessary to increase the intensity and by this the efficiency of the second-harmonic generation that occurs later in the beam path. In the next step the beam is split into two parts by a beamsplitter. Each of the two partial beams travels through one of the arms of a Mach-Zehnder-type interferometer. About 10% of the initial intensity are passing two mirrors mounted on a piezo-controlled linear stage. Moving the stage back and forth changes the length of this interferometer arm. The stage has a precision of 12 nm, which is equivalent to a time delay of 80 as [115]. The first optical component in the interferometer arm of the remaining 90% of the initial intensity is a half-waveplate that rotates the polarization of the beam by 90°. Behind the wave plate, there is a stage similar to the one in the other arm, but without piezo control. For adjustment, this stage can be moved manually by a micrometer screw, but it is fixed during the experiment. After passing the stage, the beam hits a β-barium borate (BBO) crystal in which second-harmonic generation takes place. Since the polarization of the second-harmonic light is perpendicular to the one of the fundamental light, the blue to near-ultraviolet second-harmonic light after the BBO crystal is polarized along the same axis as the fundamental light before the half-waveplate. The interferometer is completed by a mirror that is highly reflective at 800 nm and nearly transparent at 400 nm. This mirror acts as a second beamsplitter that dumps the IR light in the SHG arm and recombines the remaining second-harmonic pulse with the unchanged IR pulse from the other

interferometer arm. Both the red and the blue pulse should then follow the same path to the reaction microscope. By adjusting one of the mirrors on the piezo stage and the second beamsplitter the two colors can be spatially overlapped. The temporal overlap can be found by rotating the half-waveplate by 45°, coupling out the two-color beam and sending it through another BBO crystal. The resulting beam will have two blue components that can interfere when they temporally overlap, and the interference can be observed with an optical spectrometer. To adjust the temporal overlap, the manual linear-stage is moved attentively until interferences are observed. The more straight-forward way to find the temporal overlap is to do it directly in the reaction microscope. First, the ionization rates for each color are observed separately, then simultaneously. When the two pulses do not overlap temporally the resulting rate is just the sum of the two single-color rates. In the region of temporal overlap the ionization rate increases drastically. In the end the two linear stages are fine-tuned such that the maximum rate is reached when the piezo-driven stage is nearly in its center position to have the largest possible travel range in both directions. During the experiment, the piezo stage is controlled by a program written in LabVIEW [116]. The IR pulse is delayed within a time window of approximately $\pm 10\,\mathrm{fs}$ with respect to the blue pulse, which is enough to scan over more than one IR cycle with a period of roughly $2.7\,\mathrm{fs}$.

6.3   Setup of the Reaction Microscope

The Reaction Microscope, also known as COLTRIMS (**Col**d **T**arget **R**ecoil **I**on **M**omentum **S**pectrometer) is a widely used device that was designed to investigate ionization from collisions of a projectile beam with a target. The target is usually a supersonic gas jet of atoms or molecules. With the technique of supersonic expansion, jet temperatures down to few K can be achieved. Instead of using a gas jet, the target can also consist of magneto-optically trapped atoms, which can reduce the temperature down to or even below the mK regime [117]. The setup of such a Mot-Remi (also MOTRIMS) is technically more demanding due to additional magnetic fields but will not be further discussed because the Remi used for the experiments in this thesis is using a supersonic gas jet. The projectile is usually a beam of charged particles, i.e. electrons or ions, or of intense light pulses from lasers, synchrotrons or free-electron lasers (FELs). The working principle and the precise setup of the used Remi will be presented in this chapter.

6.3.1   Supersonic gas jet

The goal of COLTRIM spectroscopy is the determination of the momenta of ions and electrons based on a precise time-of-flight and position measurement. This requires accurate knowledge of the distance between the reaction volume and the detector. The reaction volume is the region where the focused photon beam intersects with the target. The focal spot with a diameter that is typically smaller than $100\,\mu\mathrm{m}$ has to fully overlap with the target, but the spatial width of the target should not be much larger than that to avoid an

uncertainty in the distance between the target and the detectors. Another factor that could distort the result of the measurement is the temperature of the target. At room temperature, the gas particles would already have a certain thermal momentum and their average kinetic energy would be roughly $38\,\mathrm{meV}$. Even for the lightest gas species, molecular H_2, this corresponds to an average momentum of $3.2\,\mathrm{a.u.}$. In many experiments, one is however interested in measuring momenta that are smaller by at least one or two orders of magnitude. With the thermal momentum spread at room temperature, those small momenta could not be resolved. Furthermore, in molecules, there are additional degrees of freedom, vibration and rotation, that could already be excited at room temperature. A target temperature as low as technically possible is therefore essential. Both a low initial momentum spread, i.e. a low internal temperature of a few K, and a small spatial extent of the target volume are achieved with a supersonic gas jet.

The physics behind the formation of a supersonic gas jet is complex and the process is described here only very briefly. More detailed information about supersonic gas jets can be found in the literature, for example in references [118] and [119]. A simplified picture of the formation of a supersonic gas jet and its propagation through the Reaction Microscope is provided in figure 6.3. The gas is stored in a reservoir tube at room temperature and at a fairly high pressure (typically a few bars). The reservoir tube is surrounded by a low-pressure region and gas can stream from the reservoir to the low-pressure region through a small nozzle with a diameter of $30\,\mathrm{\mu m}$. If the ratio of high pressure to low pressure is larger than ~ 2.1 a supersonic expansion can occur [118]. During the experiment the low-pressure region is usually at some $10^{-3}\,\mathrm{mbar}$. After passing the nozzle, the gas expands quasistatically and adiabatically into the low-pressure region. The decrease of spatial density during expansion comes along with an increase of the momentum-space density, i.e. a reduction of temperature, as the entropy is conserved in the process [119]. In the expansion process, the disordered motion of the gas particles is transformed into a directed motion with a high momentum in jet direction and very low perpendicular momentum. The jet is called supersonic jet because there is a region behind the nozzle where it moves with supersonic speed, the so-called zone of silence with a length of a few centimeters. The jet would collapse at the end of this zone due to shock waves but by cutting out the center part of the jet before the end of the zone of silence, one can preserve it. The center of the jet is extracted by a set of skimmers. These conical apertures reduce even more the jet temperature because gas particles with a too large momentum perpendicular to the jet direction miss the aperture. Furthermore the skimmers serve as differential pumping stages to reduce the pressure from low vacuum in the first jet chamber to ultra-high vacuum (UHV) in the main chamber. The Remi described in this thesis uses two skimmers with an aperture diameter of $200\,\mathrm{\mu m}$ and $400\,\mathrm{\mu m}$. After the crossing with the laser beam in the spectrometer chamber, the jet is guided to an exhaust tube by a system of vacuum pumps (the jet dump in figure 6.3).

6.3.2 Spectrometer

After the last skimmer, the gas jet enters the spectrometer chamber, where the interaction with the projectile beam and the detection of the ionization products take place. The
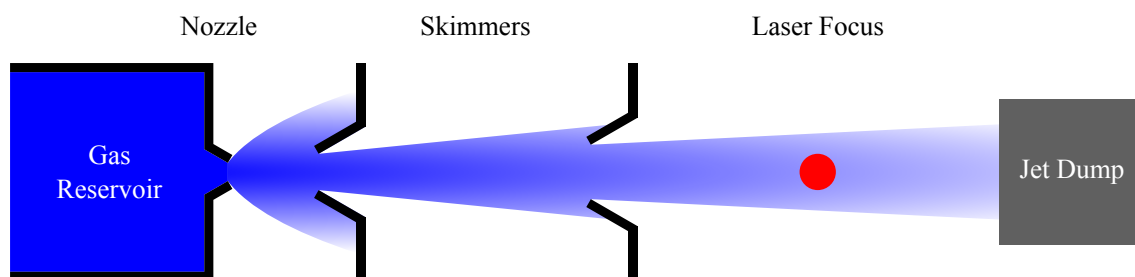
Figure 6.3: Drawing of the gas jet with nozzle and skimmers.
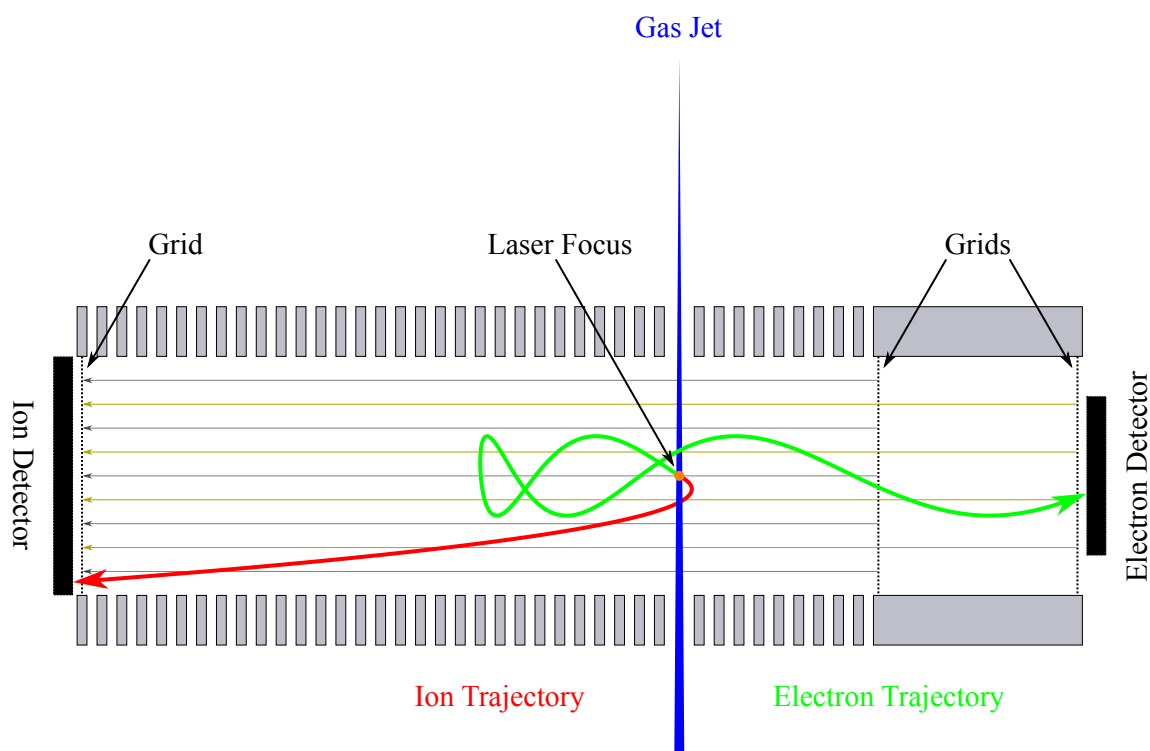
Figure 6.4: Schematic of the spectrometer in the interaction chamber of the reaction microscope with exemplary electron and ion trajectories. Ionization occurs where the laser is crossing the gas jet. The electron trajectory in the acceleration region is a superposition of a parabola from the acceleration in a homogeneous electric field (symbolized by gray arrows) and a circular motion caused by the Lorentz force induced by the magnetic field (beige-colored arrows). In the drift region, the electron only feels the influence of the magnetic field. The trajectory of the ion is nearly unaffected by the magnetic field and can in most cases be considered as a pure parabola.

pressure in the chamber has to be in the order of 10^{-11} mbar such that collisions between the charged fragments and the rest gas are very unlikely. A sketch of the spectrometer is shown in figure 6.4. It consists of an acceleration region with a homogeneous electric field. The electric field accelerates positively charged ions and negatively charged electrons into opposite directions onto two time- and position-sensitive detectors. On the side dedicated to the detection of electrons, there is an additional field-free drift region between the acceleration region and the detector. In order to shield the spectrometer from the strong electric fields in the proximity of the detectors and to separate the electron drift region from the acceleration region, there are metal grids in front of each detector and one between the acceleration and the drift region. In order to establish a homogeneous electric field, the acceleration region is built up of a stack of equally spaced metal plates. The stack has a total length of 40 cm. Each plate is connected electronically to its adjacent ones by resistors, which ideally all have exactly the same resistance in the order of kiloohms [120]. The two plates at the edge of the stack are connected to a direct-current voltage source. The interaction between projectile and target does not take place in the center of the acceleration region, but rather at a distance of 30 cm from the ion detector grid and 10 cm from the electron drift region. The fact that the ion side is longer is reasonable because in general both ions and electrons can have a trajectory with a starting direction opposite to the corresponding detector. For ions, this is a quite small effect, while electrons can cover quite a distance before the electric field forces them to return. In a shorter spectrometer, they would hit the wrong detector and would be lost. This effect could be circumvented by increasing the acceleration voltage, however at the cost of a worse momentum resolution. The length of the drift region amounts to 10 cm as well. In order to increase the acceptance for electrons with large perpendicular momenta, in addition to the electric field in the spectrometer, there is also a homogeneous magnetic field generated by a set of coils outside of the vacuum vessel [121]. The magnetic field is oriented parallel or anti-parallel to the homogeneous electric field and induces a Lorentz force that acts on all charged particles with a momentum perpendicular to the direction of the magnetic field, i.e. perpendicular to the spectrometer axis. This effect forces the particles onto a helical trajectory and hinders them from escaping the spectrometer and hitting the chamber walls. The radius and angular frequency of the helical trajectory depend on the mass of the particles and in most cases the effect is negligible for ions. However, in some measurements with very light ions like H^+ or H_2^+ for example, a considerable deviation from the unperturbed parabolic trajectory is observable.

6.3.3 Detectors

The detectors are capable of determining the impact position of a single particle on the detector and their electronic signal can also be used to measure the time-of-flight with respect to the laser trigger, which marks the moment of ionization. A complete detector that was constructed for a similar Reaction Microscope [120] is shown in figure 6.5a. The working principle of the detectors is described in the following: The upper part of a Remi detector consists of two or three stacked microchannel plates (MCP), disks made of highly resistive material with a thickness in the millimeter range and a diameter of few centime-
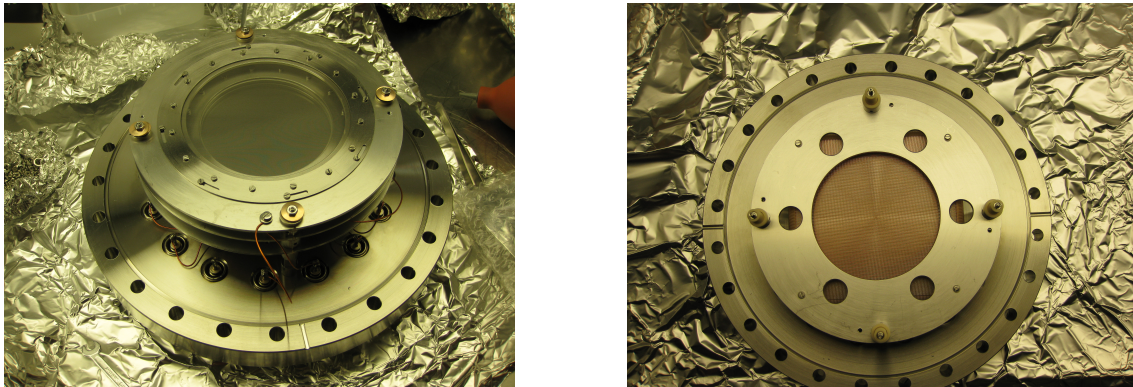
(a) Fully assembled MCP detector system   (b) Bottom of detector with delay-line anode

Figure 6.5: Photographs of a completely assembled Remi detector (a) and of the delay-line anode after removal of the top parts (b). The dark disk below the metal grid in (a) is the upper microchannel plate (MCP). The images were taken from ref. [120].

ters. An MCP features a regular array of parallel channels with a typical diameter of some 25 µm and a channel-to-channel distance of approximately 30 µm. The values mentioned here for the description of the detector system were taken from reference [122]. The channels permeate the plate under a small angle with respect to its surface normal (about 8°). A high voltage of about 1 kV to 1.5 kV per MCP is applied, with higher potential on the bottom plate. When a charged particle or a photon hits a channel wall of the top MCP, a cloud of electrons is created. The small angle increases the probability that a channel wall is hit because most particles impinge on the surface under a nearly right angle. The voltage gradient pulls the electron cloud to the bottom of the plate while the cloud hits the channel walls several times, increasing the charge of it in every step. Neighboring MCPs are usually rotated by 180° with respect to each other such that combined channels from both plates form a V-shaped channel, which is called chevron configuration, or in the case of three plates a Z-shaped channel. When the charge cloud hits the channel walls, it is possible that ions are released and accelerated in the opposite direction. These ions could generate a wrong signal on the opposite detector. By the inverted orientation of adjacent MCPs, this effect is suppressed. The Remi described in this thesis uses two MCPs with a diameter of 120 mm in chevron configuration for the ion detection and a Z-stack of 80 mm-MCPs in the electron detector. When the cloud arrives at the bottom of the MCP assembly, it has been amplified by a gain factor of typically 10^7. This is enough to generate a voltage pulse that can be coupled out and is used for the time measurement. The temporal resolution and the travel time of the electron cloud through the MCP is in the order of a few hundred ps [123]. The spatial resolution of an MCP is given by the channel diameter and distance. A single channel has a dead time in the order of 10^{-2} s. As the plate consists of 10^5 to 10^6 independent channels and because under normal experimental conditions, it is rather unlikely that the identical channel is hit repeatedly within its dead time, the effective dead time of the whole MCP is about 10^{-8} s to 10^{-7} s [124].

When the electron cloud exits the bottom of the MCP stack its position is read out with the help of a delay-line anode. This is a system of wires wrapped around a square or hexagonal anode plate [125–129] (see also figure 6.5b). In the case of a square anode,

one wire is wrapped horizontally around the plate and the other one vertically. When the electron cloud hits the two wires, the x and y-positions are encoded by the time that the induced electronic signal takes to reach either end of both wires. The reconstruction principle of the impact position for a wire of length l is as follows: Assuming the electron cloud hits the wire at a distance x from one end (and in consequence $l - x$ from the other end), the signal travels with constant velocity v towards both ends. The two arrival times are $t_1 = \frac{x}{v}$ and $t_2 = \frac{l-x}{v}$. The impact position x can be calculated from the time difference $\Delta t = t_1 - t_2$:

$$\Delta t = \frac{1}{v}(x - l + x) \Rightarrow x = \frac{v\Delta t - l}{2}. \tag{6.1}$$

It is an interesting remark that the sum of both travel times $t_1 + t_2 = t_l$ is independent of x and corresponds to the time that the signal would need to travel through the wire from one end to the other, i.e. over a distance of l. Checking if the sum of the two measured times equals t_l is useful to sort out wrong coincidences. The spatial resolution of a delay-line anode is better than $100\,\mu\mathrm{m}$, which is similar to the MCP resolution [122, 130]. Delay-line anodes are multi-hit capable as long as two signals in the wire are temporally separated [130]. In the case of a hexanode, there are three wires for the position measurement, rotated by $60°$ with respect to each other. The three wires have a higher efficiency due to redundance and a better multi-hit capability [129]. In practice there are two wires for the detection of each position coordinate, the signal and the reference wire. These two wires form a Lecher system, which efficiently reduces background noise [117].

6.3.4 Data Processing

The raw signals from the detectors consist of voltage pulses with a certain delay with respect to the trigger signal. The voltage pulses have a width of a few tens of nanoseconds and an amplitude of a few millivolts. After passing a fast amplifier, the pulse amplitudes are in the order of $100\,\mathrm{mV}$. The amplified pulses are further processed and transformed into sharp time stamps by a commercial 'fADC8/10-2' module from *RoentDek*. It contains a series of 20-bit analog-to-digital converters (ADCs) and samples the complete trace of the voltage pulses as would do a digital oscilloscope [131]. The 'CoboldPC' software package by the same company controls the device and also does some preprocessing of the data. It checks for example that the time stamps coming from the anode wires fulfill the above mentioned sum condition and converts them to position information. The software is in principle also capable of doing the momentum calculation, but this is very time-consuming as it requires to read in the complete set of data. In practice, the data analysis is accelerated by defining export conditions like for example time-of-flight and position windows and letting CoboldPC export only the data that fulfill the conditions. The actual momentum calculation for the confined data is then performed by dedicated analysis programs. In the framework of this thesis those analysis programs were scripts written in *MathWorks* 'Matlab'.

6.3.5 Momentum Reconstruction

Before the detailed explanation of how the momenta are calculated, a short remark about coordinate systems and conventions has to be made. As can be seen in figure 6.4, the spectrometer of the remi and the internal electro-magnetic fields feature a cylindrical symmetry. On that account it is consequential to decompose momenta in a component parallel and another component perpendicular to the spectrometer axis. The process of photoionization has also cylindrical symmetry if linearly polarized light is used with the direction of polarization being the cylinder axis. In the field of laser physics, it is common to define the direction of propagation of the light as the z-direction. In experiments involving a Remi, however, it is the convention that the spectrometer axis is aligned along the z-direction. In most Remi experiments, especially with a laser beam as the projectile, the spectrometer axis is perpendicular to the propagation of the projectile, such that one of the two z-axis conventions has to be chosen. If not explicitly stated differently, the Remi convention will be used in the following and throughout the thesis. For the sake of completeness, it should be mentioned that there are some Remi experiments with an electron beam projectile in which the electron beam is propagating parallel to the spectrometer axis, in order to avoid deflection by the magnetic field (see for example [132]).

Taking into account the cylindrical symmetry, the 3D-momentum of a particle after ionization $\vec{p} = \begin{pmatrix} p_x \\ p_y \\ p_z \end{pmatrix}$ can be expressed in different ways. The z-component, which is parallel to the spectrometer axis, is also called the *longitudinal momentum p_l*, sometimes also represented by $p_{\parallel}$. The vector sum of the remaining x- and y-components, which is orthogonal to p_l, is called the *transverse* or *transversal momentum p_{tr}* (or $p_{\perp}$). In the general case without cylindrical symmetry, the momenta can also be expressed in spherical coordinates involving the two angles θ and φ. The different representations are shown in figure 6.6 and the conversion is as follows:

$$\vec{p} = \begin{pmatrix} p_x \\ p_y \\ p_z \end{pmatrix} = \begin{pmatrix} p_{tr} \\ p_l \end{pmatrix} = |\vec{p}| \cdot \begin{pmatrix} \sin(\theta)\cos(\varphi) \\ \sin(\theta)\sin(\varphi) \\ \cos(\theta) \end{pmatrix} . \tag{6.2}$$

The cylindrical symmetry of the Remi spectrometer implies that the longitudinal and the transversal momentum components are reconstructed in different ways. The raw data contain information about the times-of-flight t and the impact positions x and y on the detector. These parameters depend on the initial momentum $\vec{p}$, the spectrometer geometry and the applied electric and magnetic fields. The magnetic field does not influence the time-of-flight as the Lorentz force of the field along the z-axis only acts in the xy-plane.
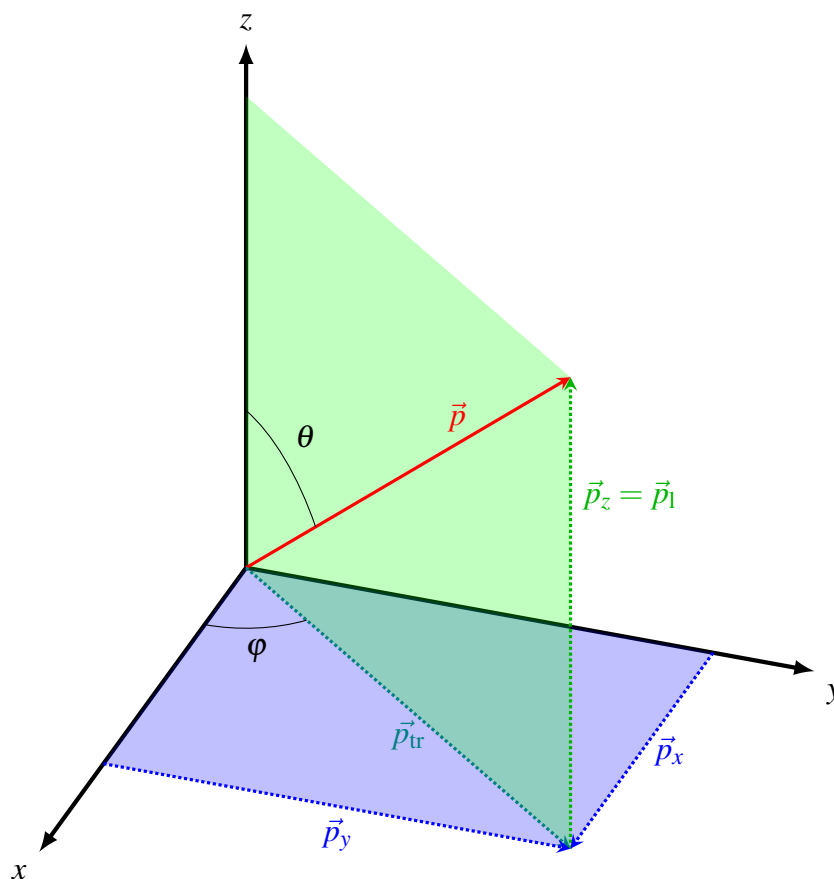
Figure 6.6: Convention of momentum axes and angles used throughout this thesis. The z-axis is parallel to the spectrometer axis and points towards the ion detector. Adapted from [58]

Longitudinal momentum

The previous explanation implies that the time-of-flight is only a function of p_l and the spectrometer geometry. A rather simple expression for the time-of-flight can be derived by solving the one-dimensional Newtonian mechanics problem and doing some mathematical transformation. For the general case of a particle with charge q and mass m that has an initial longitudinal momentum p_l and is then accelerated in a spectrometer with acceleration and drift regions of lengths l_a and l_d and a voltage drop of ΔU along l_a, the time-of-flight is

$$t(p_l) = l_a \cdot \underbrace{\frac{\sqrt{p_l^2 + 2mq\Delta U} - p_l}{q\Delta U}}_{\text{tof in acceleration region}} + l_d \cdot \underbrace{\frac{m}{\sqrt{p_l^2 + 2mq\Delta U}}}_{\text{tof in drift region}}. \tag{6.3}$$

The second term obviously vanishes when there is no drift region ($l_d = 0$). Only in that

specific case the inversion of equation 6.3, i.e. the calculation of $p_l(t)$, is analytically possible and yields

$$p_l(t) \stackrel{l_d=0}{=} \frac{ml_a}{t} - t \cdot \frac{q\Delta U}{2l_a}. \tag{6.4}$$

In the general case with a drift region the transversal momentum cannot be calculated analytically from the time-of-flight. There are several possible methods to solve this problem, which are briefly discussed in the following paragraphs.

Taylor approximation for small momenta   If the initial kinetic energy in the longitudinal direction is small compared to the energy gained in the electric field, i.e. $E_l = \frac{p_l^2}{2m} \ll q\Delta U$, or more strictly speaking $p_l \ll \sqrt{2mq\Delta U}$, equation 6.3 can be Taylor-expanded to the linear order around $p_l = 0$ (see e.g. [32, 58]). The resulting equation can be solved for p_l as a function of t:

$$p_l(t) \approx \frac{q\Delta U}{l_a} \cdot (t_0 - t), \tag{6.5}$$

with t_0 being the zeroth order term of the Taylor expansion corresponding to the time-of-flight of a particle with $p_l = 0$:

$$t_0 = \sqrt{\frac{2m}{q\Delta U}} \cdot \left(l_a + \frac{l_d}{2}\right). \tag{6.6}$$

As already mentioned above the linear approximation is only good for very low momenta. This condition is quite well fulfilled by heavy rare gas ions from photoionization but usually not by ions from molecular dissociation and electrons.

Numerical Solution   A more general method to reconstruct the longitudinal momentum is solving equation 6.3 numerically with the help of Newton's method. This method can be implemented into a computer algorithm and modern computer systems are able to perform the calculation already during the measurement. The momentum reconstruction with Newton's method is explained for example in references [133, 134].

Interpolation with lookup table   The method used in the analysis of the data presented in this thesis is the use of a lookup table. The first of its two columns contains equally spaced values of p_l and the second column contains the corresponding time-of-flight $t(p_l)$ according to equation 6.3. For every measured time-of-flight value a computer program

searches the two pairs $(p_l, t(p_l))$ with the time-of-flight neighboring the measured value. The program then performs an interpolation to determine the corresponding longitudinal momentum value that lies between the two picked momenta. This method is a fast way to determine p_l. The only prerequisite of the lookup table is that the momentum array is large enough to cover the whole range of possible times-of-flight and that the difference between two neighboring values is smaller than the resolution of the spectrometer. The temporal resolution of the described system is not better than 0.1 ns. If these conditions are fulfilled the method provides an accurate momentum calculation. It can be used for the calculation of the longitudinal momenta of ions and for electrons as well.

Transverse momentum

For the calculation of the transverse momentum the Lorentz force induced by the magnetic field has to be taken into account. The effect of the magnetic field B on a charged particle with mass M and charge q is a cyclotron motion with an angular frequency of $\omega_c = \frac{qB}{m}$. The cyclotron angle $\alpha = \omega_c t$ is proportional to the time-of-flight. As the time-of-flight roughly scales with $\sqrt{m}$ the cyclotron angle is approximately proportional to $\frac{1}{\sqrt{m}}$. This means that the cyclotron angle of even the lightest possible ion, H^+, is smaller by a factor of $\sqrt{1836} \approx 43$ compared to electrons. In a typical measurement the electrons perform about three to five full cyclotron cycles. In the case of heavier ions, this would lead to a small angle and the circular motion is negligible. In the case of H^+, the effect has to be considered, however. The different methods for (heavier) ions, electrons and light ions will be discussed in the following paragraphs.

Heavy ions   The calculation of the transverse momenta is very simple for heavy ions because the magnetic field can be neglected. As in this case there is no force changing the motion in the transverse xy-plane the ion essentially moves with constant velocity from the starting point $(0,0)$ to a spot (x,y) on the detector. The distance $R = \sqrt{(x - x_0)^2 + (y - y_0)^2}$ between (x_0, y_0), the center of the distribution of arrival positions of ions with mass m, and the actual arrival position (x,y) is connected to the transverse momentum component by the following relationship:

$$R = \frac{p_{tr} \cdot t}{m},\tag{6.7}$$

where t denotes the measured time-of-flight. It is important to note that (x_0, y_0) is not coinciding with the starting coordinates $(0,0)$ because the ions always carry the initial momentum of the gas jet. The center of the ion distribution is therefore shifted in the direction of jet propagation. Rearranging equation 6.7 yields

$$p_{tr} = \frac{m \cdot R}{t}.\tag{6.8}$$

The components p_x and p_y are obtained analogously and can also be expressed in cylindrical coordinates:

$$p_\mathrm{x} = \frac{m \cdot (x - x_0)}{t} = \frac{m \cdot R \cdot \cos \varphi}{t}, \tag{6.9}$$

$$p_\mathrm{y} = \frac{m \cdot (y - y_0)}{t} = \frac{m \cdot R \cdot \sin \varphi}{t}. \tag{6.10}$$

Electrons   For the calculation of the transverse electron momentum the magnetic field B is essential. As already mentioned, the B-field determines the angular frequency of the cyclotron motion. As the Lorentz force is always directed perpendicular to both the magnetic field lines and the current velocity vector of the electron, it does not change the absolute value of the transverse momentum but only its direction. In a projection onto the detector plane, as in figure 6.7, the electron is doing a circular motion starting from $(0,0)$ on a circle whose radius is proportional to the starting momentum ([32]):

$$R_\mathrm{cyc} = \frac{p_{\mathrm{tr}_\mathrm{e}}}{e \cdot B}. \tag{6.11}$$

In this equation, e stands for the elementary charge. In order to determine $p_{\mathrm{tr}_\mathrm{e}}$, the cyclotron trajectory has to be reconstructed from the measured information, i.e. the time-of-flight of the electron t_e and its impact position on the detector $(x_\mathrm{e}, y_\mathrm{e})$. Figure 6.7 displays the geometrical relations between the measured and the unknown quantities. In this analysis again, it is useful to work with cylindrical coordinates. Instead of the coordinates $(x_\mathrm{e}, y_\mathrm{e})$, the impact position is represented by $(R_\mathrm{e}, \theta_\mathrm{e})$. The symbol φ_e will be used to denote the azimuthal angle of the transverse momentum with respect to the x-axis.

The following relation between the angle $\alpha = \omega_\mathrm{c} t_\mathrm{e}$, the cyclotron radius R_cyc and the distance from the origin to the impact position of the electron R_e can be read from figure 6.7:

$$\frac{R_\mathrm{e}}{2R_\mathrm{cyc}} = \left| \cos \left(\frac{\alpha}{2} - 90° \right) \right| = \left| \sin \left(\frac{\alpha}{2} \right) \right|. \tag{6.12}$$

This can be solved for R_cyc:

$$R_\mathrm{cyc} = \frac{R_\mathrm{e}}{2 \left| \sin \left(\frac{1}{2} \omega_\mathrm{c} t_\mathrm{e} \right) \right|}. \tag{6.13}$$

After inserting equation 6.11 into this last expression, one obtains a solution for the absolute value of the transverse momentum:
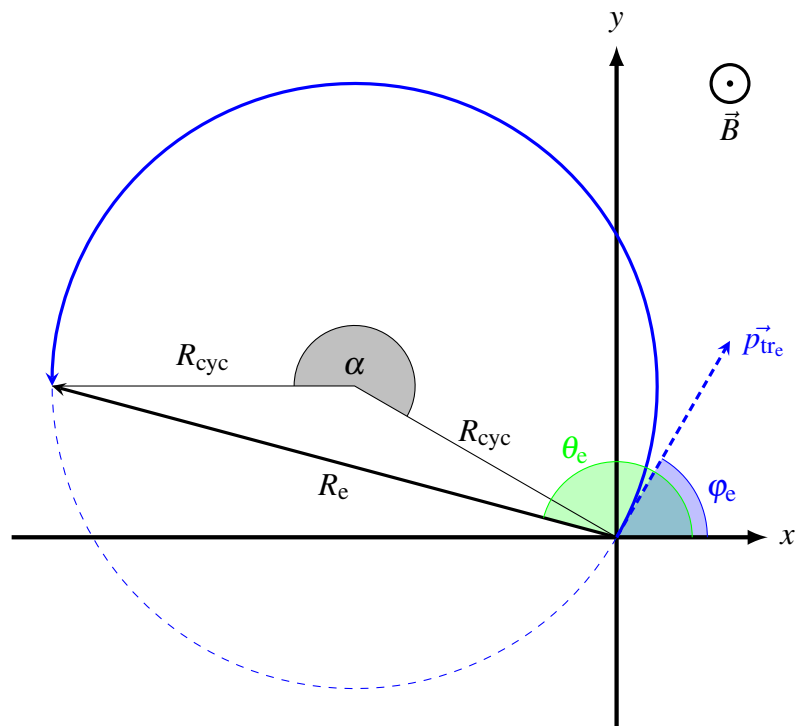
Figure 6.7: Projection of the electron motion towards the detector; after starting from the origin with $\vec{p}_{\mathrm{tr_e}}$, the magnetic field forces the electron on a circular trajectory. The radius of the circle is proportional to $|\vec{p}_{\mathrm{tr_e}}|$ (adapted from [32]).

$$p_{\mathrm{tr_e}} = \frac{R_{\mathrm{e}} eB}{2 \left| \sin\left(\frac{1}{2}\omega_{\mathrm{c}} t_{\mathrm{e}}\right)\right|}. \tag{6.14}$$

In practice, the magnetic field is not known. The measured quantity is the cyclotron frequency ω_{c}, the description of the method how to determine it follows later (6.3.6). With $B = \frac{\omega_{\mathrm{c}} m_{\mathrm{e}}}{e}$, equation 6.14 transforms to

$$p_{\mathrm{tr_e}} = \frac{R_{\mathrm{e}} \omega_{\mathrm{c}} m_{\mathrm{e}}}{2 \left| \sin\left(\frac{1}{2}\omega_{\mathrm{c}} t_{\mathrm{e}}\right)\right|}. \tag{6.15}$$

The only remaining problem, the calculation of the azimuthal angle φ_{e}, can be solved by the relation

$$\varphi_{\mathrm{e}} = \theta_{\mathrm{e}} - \frac{1}{2}\alpha = \theta_{\mathrm{e}} - \frac{1}{2}\omega_{\mathrm{c}} t_{\mathrm{e}}, \tag{6.16}$$

which also results from figure 6.7. The complete derivation of the last equations was done

for a magnetic field pointing out of the *xy*-plane as displayed in the figure. For the case of a magnetic field oriented in the opposite direction equation 6.16 changes to

$$\varphi_e = \theta_e + \frac{1}{2}\omega_c t_e. \tag{6.17}$$

This is in principle also consistent with equation 6.16 because mathematically the sign of ω_c changes when the direction of $\vec{B}$ is inverted. It is also important to check that the two coordinate systems used for electrons and ions are the same. Otherwise the coincidence conditions will not be fulfilled correctly for all three vector components. The consistency can for example be achieved by rotating one of the two systems or by other measures if necessary at all.

6.3.6   Calibration procedure

All of the previously mentioned methods are based on the precise knowledge of the spectrometer geometry and perfectly homogenous fields. Under real conditions, such exact knowledge is not possible. Especially the homogeneity of the applied fields is not realized in the whole setup, which is in particular a problem in the determination of p_l. The results of inserting the known input parameters, i.e. the measured data and the experimental parameters such as the spectrometer dimensions and the applied voltage, into the formulas are in general only approximating the correct momenta. To find out whether the calculated results are reasonable it has to be checked that the calculated momenta of coincidently measured particles fulfill the conditions of momentum conservation. In the case of single ionization one has to plot the pairs of the longitudinal momenta of the electron and the ion in a 2-dimensional histogram, as is done in figure 6.8. The majority of the counts has to lie on a diagonal line such that $p_{l_e} + p_{l_{ion}} = 0$. If this is not the case, the experimental parameters are wrong. The adjustment of these parameters has been done as follows: First, the geometrical parameters of the spectrometer, i.e. the lengths of the acceleration and drift regions are assumed to be constants according to the construction plans of the Remi. In the next step, the experimental value of the acceleration voltage and the value of a temporal offset in the raw time-of-flight spectra of the ions, caused by electronic delays, are determined. For that purpose, two peaks of a known ion species are selected in the raw time-of-flight spectrum. This can be the single- and double-ionization peak of the same species in a pure gas, or two single ionization peaks of different species in a mixture. In general, it is useful to select two large peaks with a reasonable temporal distance. The time values minus the yet unknown temporal offset t_0 at the center of the two peaks are inserted into the formula 6.3. The centers of the peaks correspond to a vanishing longitudinal momentum, $p_l = 0$, which is also inserted into the formula. In the end, with the masses m_i and the charges q_i of the different ions, two equations with two unknowns are obtained:
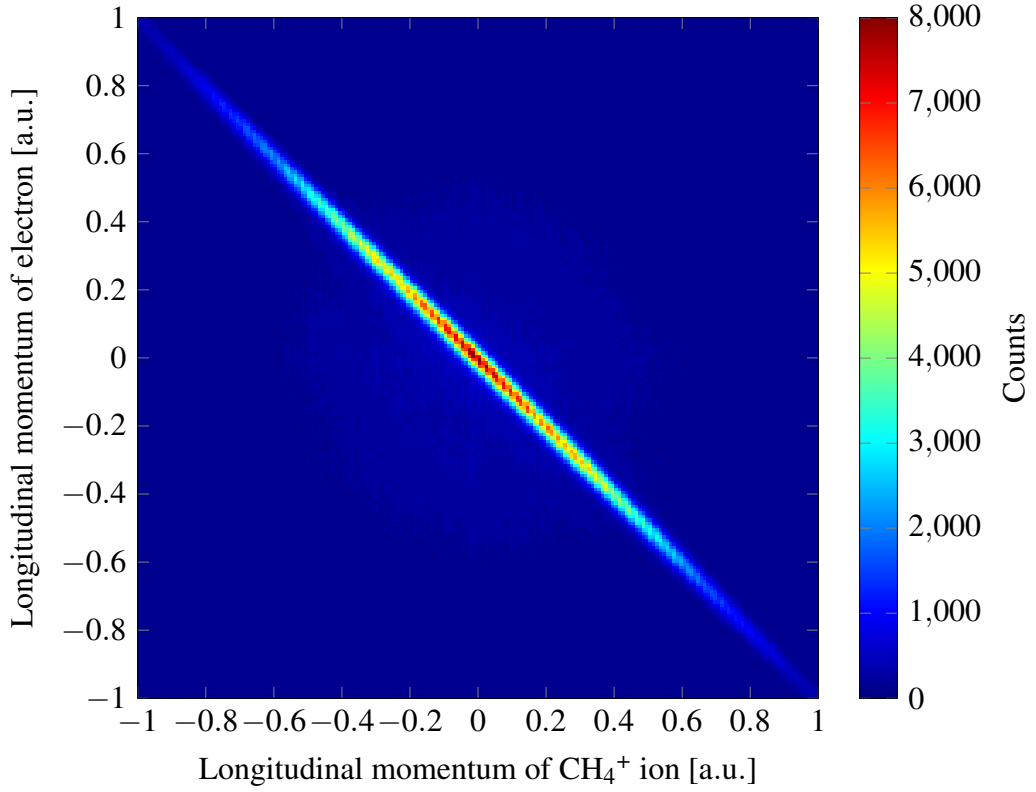
Figure 6.8: CH_4^+-electron longitudinal momentum coincidence map. True coincidences fullfill momentum conservation. In this plot, they are located on a thin diagonal line with $p_{l_{ion}} + p_{l_e} = 0$, which indicates a good selection of the calibration parameters. By defining a condition for the sum of the longitudinal momenta, wrong coincidences that are not lying on the diagonal can be excluded in the further data analysis.

$$t_1 - t_0 = l_{a_{ion}} \cdot \frac{\sqrt{2m_1 q_1 \Delta U_{ion}}}{q_1 \Delta U_{ion}} \tag{6.18}$$

$$t_2 - t_0 = l_{a_{ion}} \cdot \frac{\sqrt{2m_2 q_2 \Delta U_{ion}}}{q_2 \Delta U_{ion}}. \tag{6.19}$$

Solving these two equations is possible analytically and yields a result for the time offset t_0 and the potential difference along the length of the ion acceleration region. Note that the length of the ion drift region is 0. As the electric field is the same in the acceleration region for the electrons, its potential difference can be deduced from U_{ion} by multiplying it with the factor $\frac{l_{a_{el}}}{l_{a_{ion}}}$, the ratio of the lengths of the acceleration regions. For the electrons, there is also an unknown temporal offset. The method to determine this makes use of the helical trajectory of the electrons in the magnetic field. The projection of the trajectory onto the xy-plane is a circle for every electron. All of these circles have one point in common, which is the projection of the interaction volume, where the photoionization takes place and the trajectory starts (see figure 6.7). The 2D-histogram of the electron time-

of-flight and the x-, y- or R-coordinate ($R = \sqrt{x^2 + y^2}$) of the impact position shows a characteristic 'wiggle' structure with nodes of high count density that are equally spaced in time (cf. figure 6.9). The times-of-flight at these nodes correspond to the moments
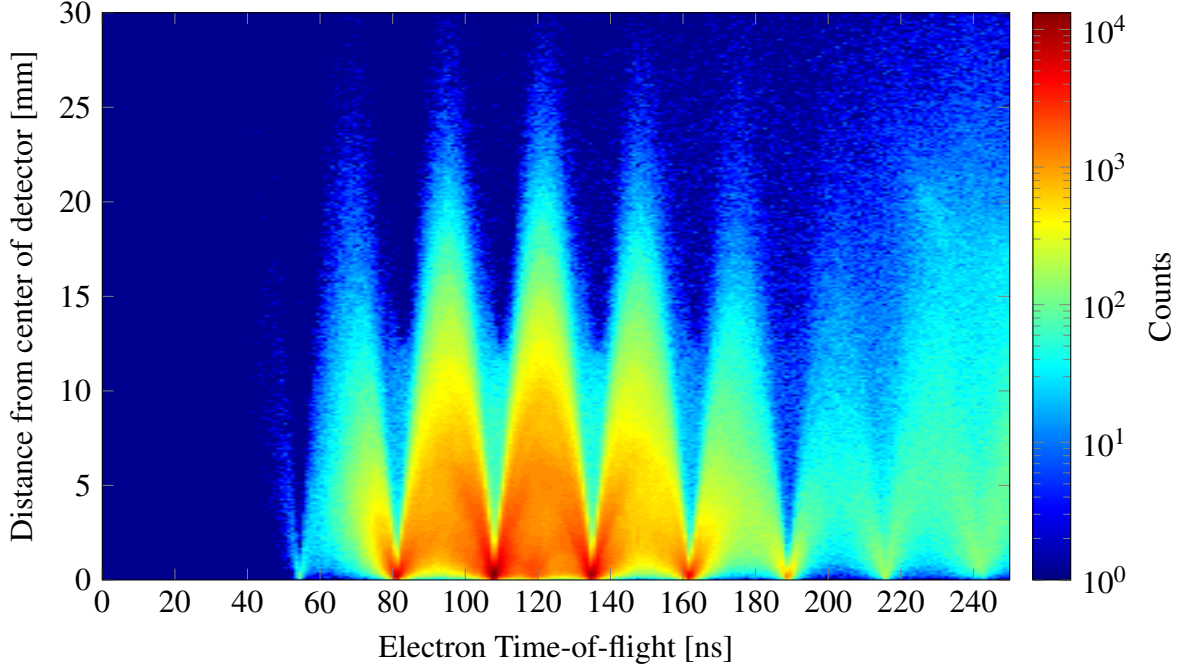

Figure 6.9: Wiggles plot: Distance between impact position of the electron and center of the detector plotted as a function of its time-of-flight. The oscillation represents the cyclotron motion of the electrons in the magnetic field. After a full cycle, the electron returns to its starting point at $R = 0$. The temporal difference between the nodes is the cyclotron period τ_c.

when the electron completes an integer number of cyclotron orbits. Hence, the time difference τ_c between subsequent nodes allows for the calculation of the cyclotron frequency $\omega_c = \frac{2\pi}{\tau_c}$. In practice, it is determined by a linear fit of the node position as the function of the time-of-flight. With the help of this fit, it is also possible to find the temporal offset because the electron time-of-flight starts with the 0th node and the other nodes have to occur at integer multiples of the cyclotron period τ_c. As a first step, the nodes are shifted to such a position by subtracting a certain value from the measured time-of-flight. The time value is then corrected up to an integer multiple n of τ_c. Whether the right n has been chosen can be decided from the coincidence plot of the longitudinal momenta of the electron and the corresponding ion. When the events are lying on a diagonal line such that $p_{l_e} + p_{l_{ion}} = 0$, n is chosen correctly and so is the time offset of the electrons. At this point, the longitudinal calibration and also parts of the transverse calibration are finished. What remains left is the spatial orientation of the detector arrays with respect to the frame of reference given by the geometry of the remi and the polarization of the laser pulse. As the impact position of most ions from the gas jet ionized by the laser is confined to a small area on the detector pointing along the direction of jet propagation, it is possible to mathematically rotate the detector image such that the jet propagates along the negative

y-direction. The electrons, however, can hit the detector at any spot and the mathematical rotation is done after the calculation of the transverse momentum by verifying again the momentum conservation with the corresponding ions.

6.4 Determination of the two-color phase

The experiments on photoionization were performed with laser pulses consisting of a linearly polarized 800 nm fundamental pulse of a duration of about 30 fs and overlapped with its second harmonic, which had the same direction of linear polarization. By tuning the time delay between the two pulses on a subcycle scale, the shape of the two-color pulse could be varied. This variation is expressed by the relative phase φ between the two pulses. How the relative phase between two pulses of the same amplitude influences the resulting electric field is shown in figure 6.10. The figure shows how strongly the field shape and maximum amplitude change when the phase delay φ is varied, and a strong influence of the phase delay on the photoionization can be expected because of the non-linearity of the process, even if one of the two pulses has a relatively small amplitude compared to the other one. Figure 6.10 also shows that the resulting electric field can be treated as a superposition of two continuous waves (cw) if only a few cycles around the maximum of the field envelope are considered. Considering cw fields, the shape of the resulting field is 2π-periodic with respect to the phase delay φ and so should be the physical response of the investigated system, i.e. the molecules exposed to the laser field. In the experimental setup presented in this chapter, there is no device to measure explicitly the value of φ. The raw dataset of a remi measurement is a list of registered ionization events. Each event contains the time-of-flight of at least one charged particle, as well as the time signal that corresponds to the particle's impact position on the detector. In most cases, the event contains the information of an electron-ion pair. A last raw information that is saved for each event is the position of the translation stage of the Mach-Zehnder interferometer (see section 6.2) that is used to tune the delay between the red and the blue pulses. This position information is directly correlated with the phase of the two-color laser field, but it has to be converted into a real phase value in a certain way, which will be described below. It can be expected that the relation between the position of the translation stage and the phase is linear and a certain position always corresponds to a certain phase value. This assumption is correct only for very short measurements that do not take much longer than about one hour. However, to collect enough statistics, the usual duration of an experiment with reaction microscopes is much longer, in the order of days. During this long time, inevitable variations of the temperature or pressure of the air that the laser pulse is passing through change the refractive index, introducing an additional delay, and it becomes impossible to directly convert a position value into a phase value. To solve this problem, the complete dataset is split up into smaller parts corresponding to a duration of about one hour, and the phase calibration is done for each part separately. In order to be able to calibrate the phase of the two-color field for each part of the dataset, it is necessary to introduce and analyze a physical quantity that varies with the phase. Such a quantity can for example be the ionization yield because strong-field ionization highly depends on the electric field strength, as can be seen in chapter 4. A yet better
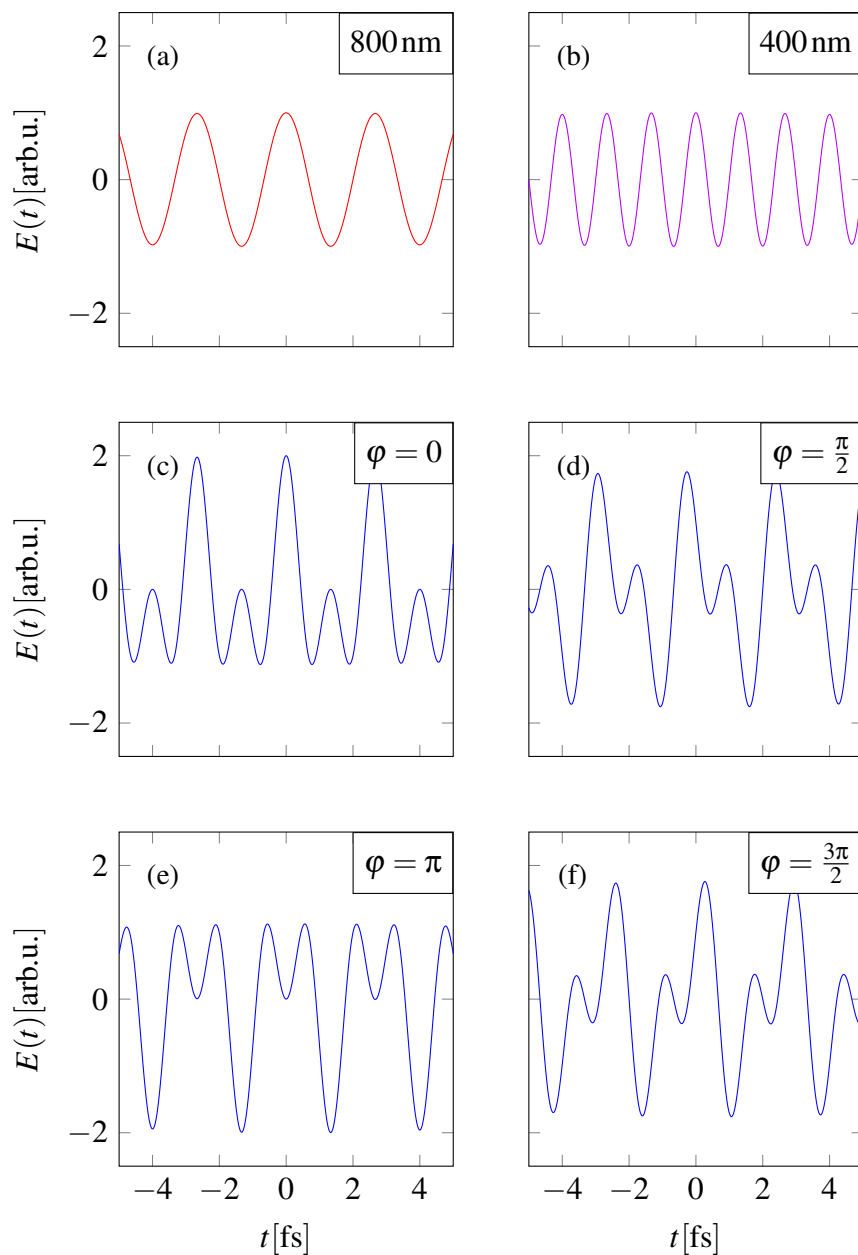
Figure 6.10: Electric field of a fundamental (800 nm, a) and second harmonic (400 nm, b) pulse with a pulse duration of 30 fs. Within a few cycles around the maximum of the pulse envelope, the amplitude is nearly constant and the field can be treated as a continuous wave. By overlapping the two pulses and varying the relative delay between them on a subcycle scale, the field shape is changed significantly (c to f). The delay between the pulses is expressed by the relative phase φ, where a change of 2π corresponds to a shift of one cycle of the SHG pulse. As $\Delta\varphi = 2\pi$ is also the periodicity of the resulting electric field, the electron momentum distributions after photoionization by this field will have the same periodicity.
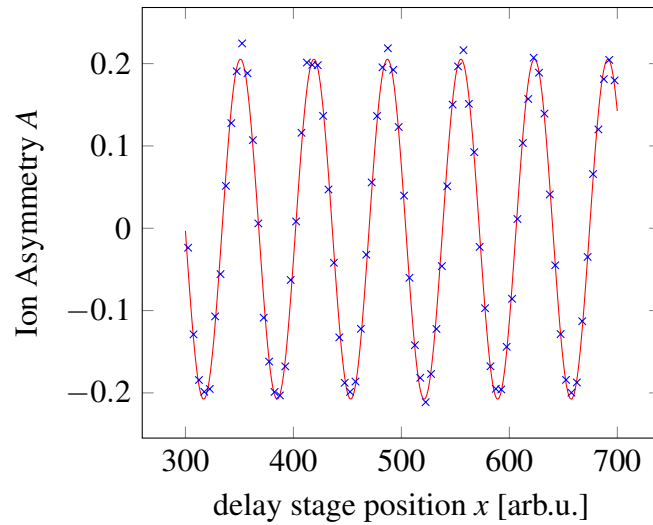
Figure 6.11: Photoion asymmetry of the longitudinal momentum of singly charged Ar⁺ ions plotted as a function of the position of the Mach-Zehnder delay stage for one data subset of about one hour of measurement time. One full cycle of the sinusoidal asymmetry corresponds to a 2π-shift between the red and the blue laser pulses. The fitted sine function in red yields the parameters to convert the raw position values into a phase value.

quantity is the so-called asymmetry parameter A, which compares the ionization yield of photoelectrons or -ions being emitted with positive longitudinal momentum by the yield of emission with negative longitudinal momentum (see for example [37]). A is defined as

$$A(\varphi) = \frac{n_+(\varphi) - n_-(\varphi)}{n_+(\varphi) + n_-(\varphi)}, \tag{6.20}$$

where n_+ and n_- denote the amount of electrons emitted with a positive or negative longitudinal momentum, respectively. Asymmetric ionization yields can be explained by the phase-dependent break of inversion symmetry of the two-color laser field [27]. The asymmetry parameter is therefore 2π-periodic as the electric field and is well-suited for the calibration of the phase. Calculating A for a reference process, for example the single ionization of the target molecule, and plotting the points versus the Mach-Zehnder stage position yields a sinusoidally shaped scatter plot with a few oscillations. The coefficients a_i of the fit function

$$f = a_1 + a_2 \cdot \sin(a_3 x + a_4) \tag{6.21}$$

allow for the transformation of the stage position x into a phase, which is the argument of the sine. The coefficient a_1 is by definition of the asymmetry very close to 0 and large deviations from that value indicate a wrong momentum calibration. The amplitude of the asymmetry, a_2, strongly depends on the underlying process. The 'frequency' of the sine, a_3, is nearly constant throughout all partial datasets, which reflects the assumption of a linear relation between the stage position and the phase. The last coefficient, a_4, is a time-dependent phase offset whose origin are the above-mentioned thermal effects. The obtained fitting coefficients of all data subsets can be used to calculate an explicit phase for each single event of the complete dataset. Assuming that the thermal drifts are a continuous process without sudden jumps, it is possible to interpolate between the

coefficients a_4, which yields a phase offset b for each event. As a next step, the phase is calculated for each event by the formula

$$\varphi = a \cdot x + b, \tag{6.22}$$

where a=$\overline{a_3}$ is the arithmetic mean of the coefficients a_3 of all data subsets. Finally, the phase values calculated with the help of equation 6.22 are wrapped such that they are lying in an interval from 0 to 2π. An important remark is that φ is still containing an unknown but constant phase offset, which is determined by the physical reference process used for calibration. A determination of the absolute phase of the electric field is hence not possible. However, as long as phase differences are considered, this is sufficient, and the above method is a good way to attribute a consistent phase value to each event of the measurement. The comparison of the phase offset of the asymmetry parameter of different ionization processes can contain information about the physical mechanisms and is part of the analysis chapter.

6.5   Setup of a beamline for high-harmonic generation

An additional experimental part of this thesis' work was the construction of a beamline for the generation of high harmonics from an ultrashort infrared laser pulse. The design of the first part of the beamline was basically a copy of an HHG beamline, which was already in use in the Interatto research group at MPIK in Heidelberg. A brief description of this original beam line is given in the next paragraph. Its design is discussed in great detail in [135], and a schematic of it is displayed in figure 6.12. Similar to the measurements with a reaction microscope, a vacuum is needed for HHG experiments because the photons in the vacuum ultraviolet (VUV) and extreme ultraviolet (XUV) spectral range ($\sim$5 to $\sim$120 eV) are absorbed in air. The beamline consists of a sequence of vacuum chambers that are equipped with various tubings, optical and electronic components to generate the high-harmonic light and to analyze its interaction with a target. The high harmonics are generated in the very first chamber of the beamline setup. The generation is achieved by focusing a few-fs IR pulse into a gas cell that is typically filled with a rare gas. The gas cell is a small tube with two holes in the tube wall such that the IR and HHG light can pass. The backing pressure inside the tube is about 10 to 100 mbar, depending on the target gas. Some quantity of the gas is leaking through the holes into the vacuum, which is maintained by a high-performance $2000 \, \mathrm{L \, s^{-1}}$ turbomolecular pump, such that the pressure in the chamber is below 10^{-3} mbar. The IR focus where HHG takes place can be considered as an almost pointlike source spot from which both IR and HHG beams start propagating in the same direction. If the generating IR pulse is sufficiently short, ideally only one full cycle of the electric field, and with proper gating techniques (see for example [136]), it is possible to generate an isolated HHG pulse, with a duration in the order of hundreds of attoseconds. With an IR pulse consisting of multiple cycles, a train of attosecond pulses is generated. Since their divergence is different, the profile of the combined IR-XUV beam consists of the HHG beam in the center overlapped by the IR beam with a larger diameter. After passing through a
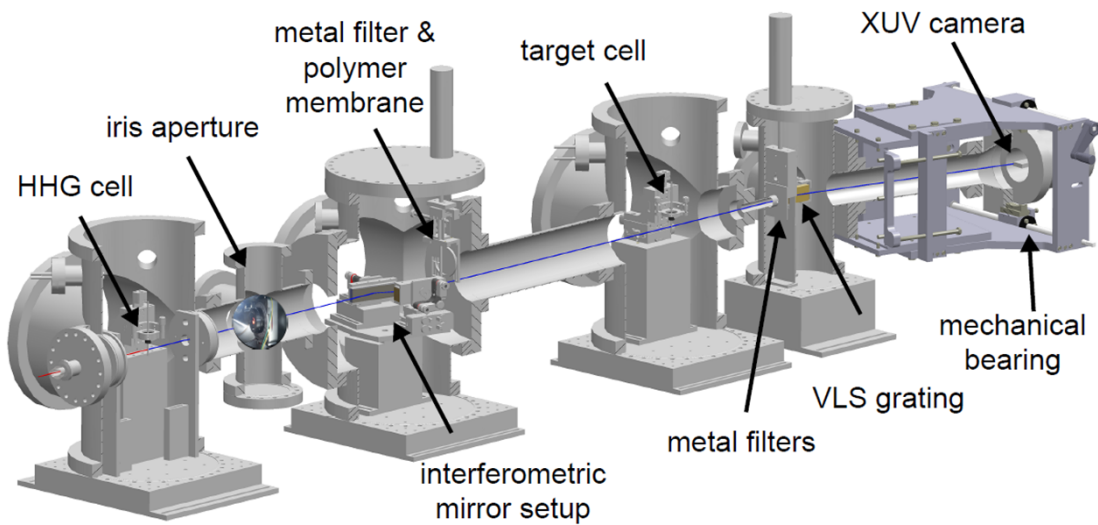
Figure 6.12: Schematic of the attosecond transient absorption spectroscopy beamline at MPIK in Heidelberg. The IR beam enters the vacuum system from the left and is focused into the gas cell for high-harmonic generation. IR and XUV light copropagate through a controllable iris to adjust the IR intensity. The light is refocused by a toroidal mirror and a time delay between XUV and IR is introduced by the interferometric mirror setup. Metal and polymer filters are used to separate the beams spatially. The refocused XUV and IR pulses interact with the target in a second gas cell. The remaining IR light is blocked by another metal foil and the transmitted XUV light is spectrally resolved and imaged by a grating and a CCD camera system (taken from [135]).

differential pumping tube the beam reaches a chamber with an electronically controlled iris aperture. The iris is able to steer the intensity of the infrared pulse without reducing the HHG intensity because of the different beam diameters. The interferometric mirror setup in the following chamber consists of two main parts. The first part is a toroidal mirror for the refocusing of the beam into the next chamber where a second gas cell filled with a target gas is located. Technically, the toroidal mirror is not refocusing the beam but it does a one-to-one image of the HHG source spot. The second part is composed of a large flat mirror with a small hole in its center. In this hole there is another mirror, which can be translated back and forth by a piezoelectric actuator with nm precision. This setup allows to temporally delay or advance the inner (XUV) beam with respect to the outer (IR) beam. Both the toroidal mirror and the time-delay mirror system are hit by the beam under grazing incidence in order to maximize the reflectivity for HHG light. Between the mirror and the target chamber, an assembly of thin metal and polymer foils allows to block the IR beam or to select a certain energy range from the high-harmonics spectrum. The metal filter is only a few hundred nanometers thick, which is enough to efficiently block the IR light and be transmissive for XUV light. The transmissivity is frequency- and material-dependent, therefore filters of different metals are used for the desired experimental conditions. The target chamber is basically a copy of the HHG chamber, also separated from the other chambers by differential pumping tubes. After passing the target, another metal filter blocks the remaining IR light to prevent the subsequent spectrometer from suffering damage. The spectrometer is built of a grating with variable

line spacing that spectrally splits the high-harmonics beam and images the spectrum into a plane. The CCD chip of a UV and X-ray sensitive camera coincides with this imaging plane. As the spectral plane of the grating is wider than the CCD chip, the camera position can be moved in the plane to the spectral region of interest. The combination of the iris aperture and the interferometric mirror setup allows for experiments to investigate the XUV absorption of the target, as a function of the IR-XUV time-delay and of the IR-intensity. Based on pump-probe type methods like (attosecond) transient absorption spectroscopy ([137, 138]), experiments with this beamline could for example demonstrate how a symmetric Lorentzian absorption line can be converted into an asymmetric Fano line and vice versa ([3, 139, 140]). In a different experiment, the correlated dynamics of both electrons in doubly excited states in helium could be studied ([2]).

Based on this first beamline setup, a second one was designed. Initially planned as an exact copy of the original one with a reaction microscope in place of the target gas cell, the design was finally modified when it came to a collaboration with the group of Prof. Reinhard Dörner at the university of Frankfurt. The group in Frankfurt needed a tabletop low-flux XUV light source for electron time-of-flight spectroscopy in solids and superconductors ([141–144]), as a compact alternative to a synchrotron. Since only XUV light was needed for the experiments, the differential pumping tube behind the HHG chamber was replaced by a vacuum valve with included mount for a metal filter to block the IR light. The iris aperture was kept for the control of the XUV intensity and was also used for alignment purposes. The main modification of the beamline design was the replacement of the time-delay mirror setup by a grating mounted on a rotatable goniometer. The initially used grating had a groove density of $600\,\mathrm{mm}^{-}1$, but it can be replaced easily by another grating. The modified mirror chamber is shown in figure 6.13. Depending on the angle position of the goniometer, either the zeroth or the first diffraction order of the incident XUV light is passed to the toroidal mirror. From there, the light passes a slit and finally reaches the target. By rotating the goniometer, a specific photon energy can be selected. The beamline was tested and was able to generate high harmonics, which was proven by a home-built MCP/phosphor screen detector. Figure 6.14 shows the fluorescence signal of the first diffraction order of high-harmonic light impinging on the phosphor screen. In figure 6.15, the spectrum with assignment of the harmonic orders is shown. Due to the relatively long pulse duration of the IR pulse (40 fs), the harmonics show up as discrete spikes in the spectrum. With a shorter generating pulse, the high-harmonic peaks would be broader. The results demonstrate the capability of the beamline setup to provide XUV photons in the energy range of 20 to 50 eV, as was requested by our coworkers in Frankfurt. The spectral range of the setup is limited by the rotation angle of the goniometer, but by using a grating with a different groove density, the spectral range and resolution can be modified.
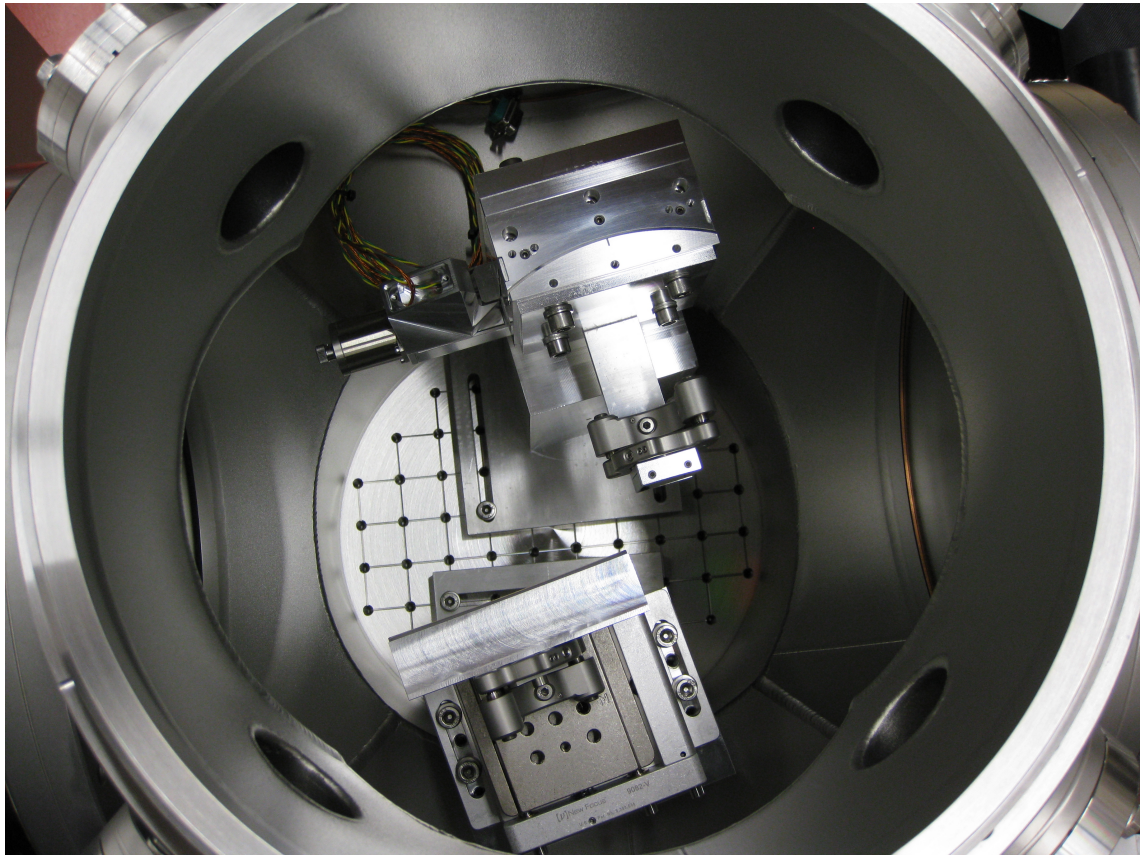
Figure 6.13: Modified mirror chamber with grating mounted on a goniometer instead of the time-delay mirror setup.

Figure 6.14: First diffraction order of XUV pulse detected by an MCP/phosphor screen assembly. The electron clouds generated in the MCP when an XUV photon hits the detector are amplified and initiate fluorescence in the phosphor screen (By courtesy of Phillip Klaus).

Figure 6.15: High-harmonics spectrum recorded at the setup in Frankfurt. The different harmonic orders are indicated (By courtesy of Phillip Klaus).

Chapter 7

Results

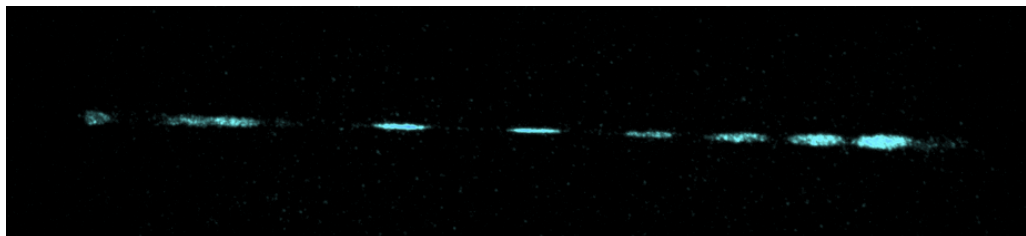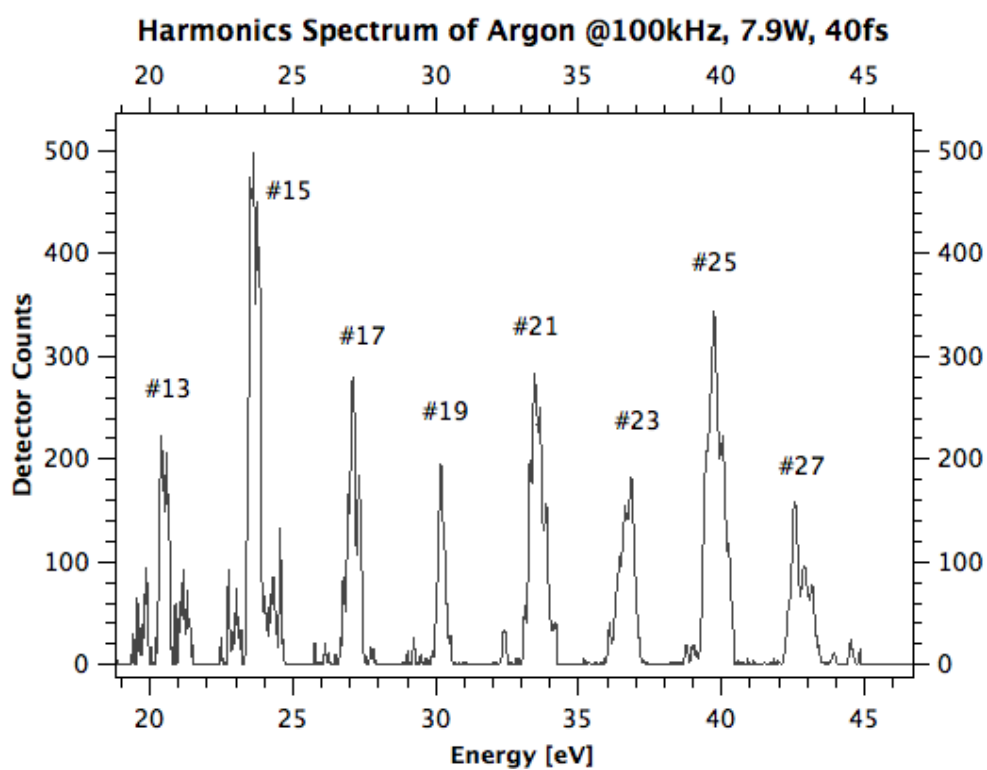The typical data set of a measurement with a reaction microscope contains information about time-of-flight and impact position of all electrons and ions detected in coincidence during one trigger event. Especially for the case of photoionization of molecules, a lot of ionization and fragmentation channels are imaginable. Each channel is characterized by its end products, the number and species of produced fragments, i.e. ions, electrons and neutral fragments, which are not detectable with the Remi. By the coincidence technique of the Reaction Microscope, it is possible to select only those events that are relevant for a certain ionization channel. The time-of-flight of a certain ion is directly linked to its mass, more precisely to its mass-to-charge ratio $\frac{m}{q}$, and this allows to define a time-of-flight window which corresponds to the arrival time of one specific ion species. If all fragments of an ionization event are detectable, wrong coincidences can be effectively sorted out by checking for the conservation of momentum. In some cases, this method is not possible because of one or more neutral fragments, which are missing in the calculation of the momentum sum. As certain ions can be produced in several processes, it is possible to further limit the data set, for example by only looking at events with electrons with a very small energy. The coincidence technique was used to analyze different phenomena that were found in photoionization experiments with argon, methane, and hydrogen, with a particular focus on methane and the generation of photoelectrons with kinetic energies below $\sim 200 \, \mathrm{meV}$. These results will be discussed in this chapter.

7.1 Preparatory measurements with an argon-methane mixture

Before the actual measurements with pure methane, some experiments intended as a test were performed with a mixture consisting of $90\,\%$ argon and $10\,\%$ methane. The goal of doing experiments with a gas mixture was to compare the actual molecule of interest, CH_4, to a well-studied simpler system, in this case the Ar atom. The particular mixing ratio was chosen because a bottle of this mixture was in stock when the experiments

were performed. And despite the low percentage of methane in the mixture a significant amount of ionization events from methane was expected due to the different ionization potentials: 15.8 eV for argon compared to 12.6 eV for methane. The ion time-of-flight spectrum shows however that the count rate for methane ions is still relatively low (figure 7.1). Although a lot of fragment ions are detected, a good statistics is only obtained
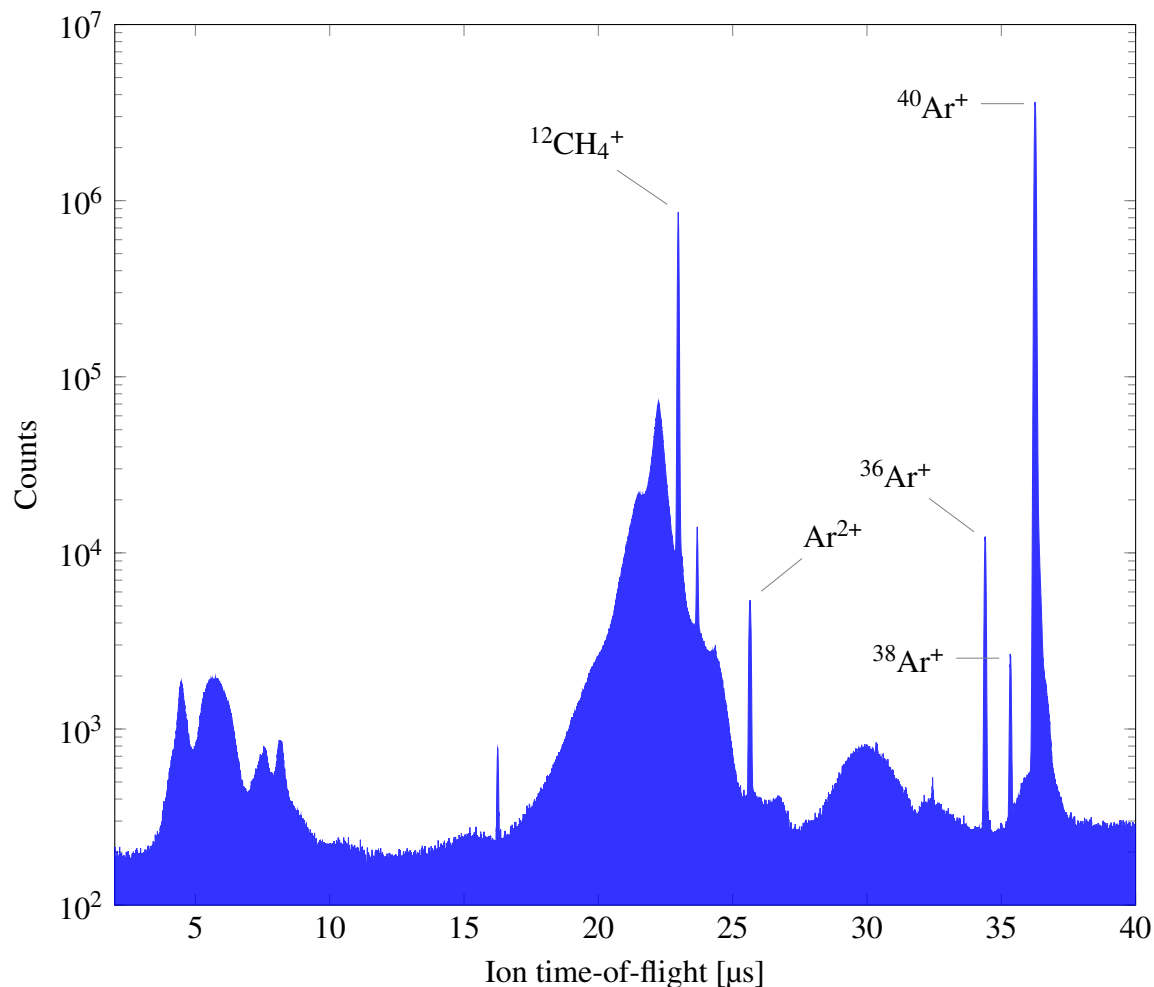

Figure 7.1: Raw time-of-flight spectrum of two-color photoionization of an argon/methane mixture. The Ar and CH_4 ion peaks are marked. The time-of-flight spectrum of ions arriving before CH_4^+ belongs to lighter methane fragments and will be discussed in section 7.2 (cf. figure 7.3).

for the CH_4^+ ion. So, at first, the analysis of the experiments with the Ar/CH_4 mixture was limited to the comparison of the non-fragmenting single ionization of both target species. To investigate the influence of the phase of the two-color field on the ionization process of the two target species the longitudinal momentum asymmetries were calculated and compared (figure 7.2). The data and the fitted sine curves show differences both in the asymmetry amplitudes (CH_4^+: (0.2510 ± 0.0016) rad, Ar^+: (0.2941 ± 0.0009) radian) and the offset phases. The difference of the phase offsets is $\Delta\varphi = (0.2845 \pm 0.0071)$ rad. A difference in the momentum asymmetry for the two species could be expected due to the different ionization potentials. The different asymmetry amplitudes give an indication
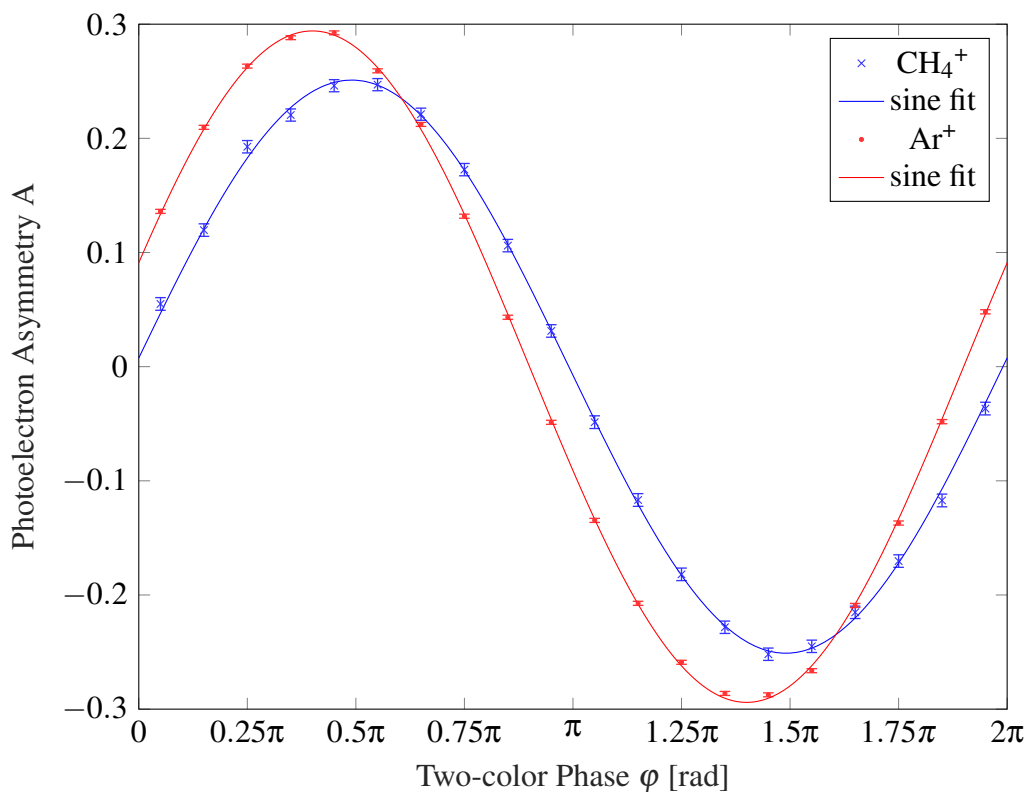
Figure 7.2: Comparison of the longitudinal momentum asymmetry of photoelectrons measured in coincidence with CH_4^+ (blue crosses) and Ar^+ (red dots) in the same measurement. The sinusoidal fit of the asymmetry data yielded a phase difference of $\Delta\varphi = (0.2845 \pm 0.0071)\,\text{rad}$, which the Ar^+ curve advances the CH_4^+ curve.

of how strongly the asymmetric laser field is influencing the target atom or molecule. The lower amplitude in the CH_4^+ photoelectrons could indicate a fundamentally different ionization mechanism between argon and methane, involving intermediate states with a comparably long lifetime, such that the electron is released when the laser pulse has already passed.

7.2 Two-color photoionization of pure methane

7.2.1 Overview of ionization channels

As the main goal of the experiment was the investigation of different ionization channels of the methane molecule and due to the unfavorable mixing ratio of the argon-methane mixture, the experiment was redone with pure methane. The time-of-flight spectrum of the detected ions looks the same for this gas, without of course the peaks corresponding to argon ions. But due to the better statistics, it is now also possible to have a deeper look at

ions other than CH_4^+. The time-of-flight spectrum is shown in figure 7.3. The sharp peak
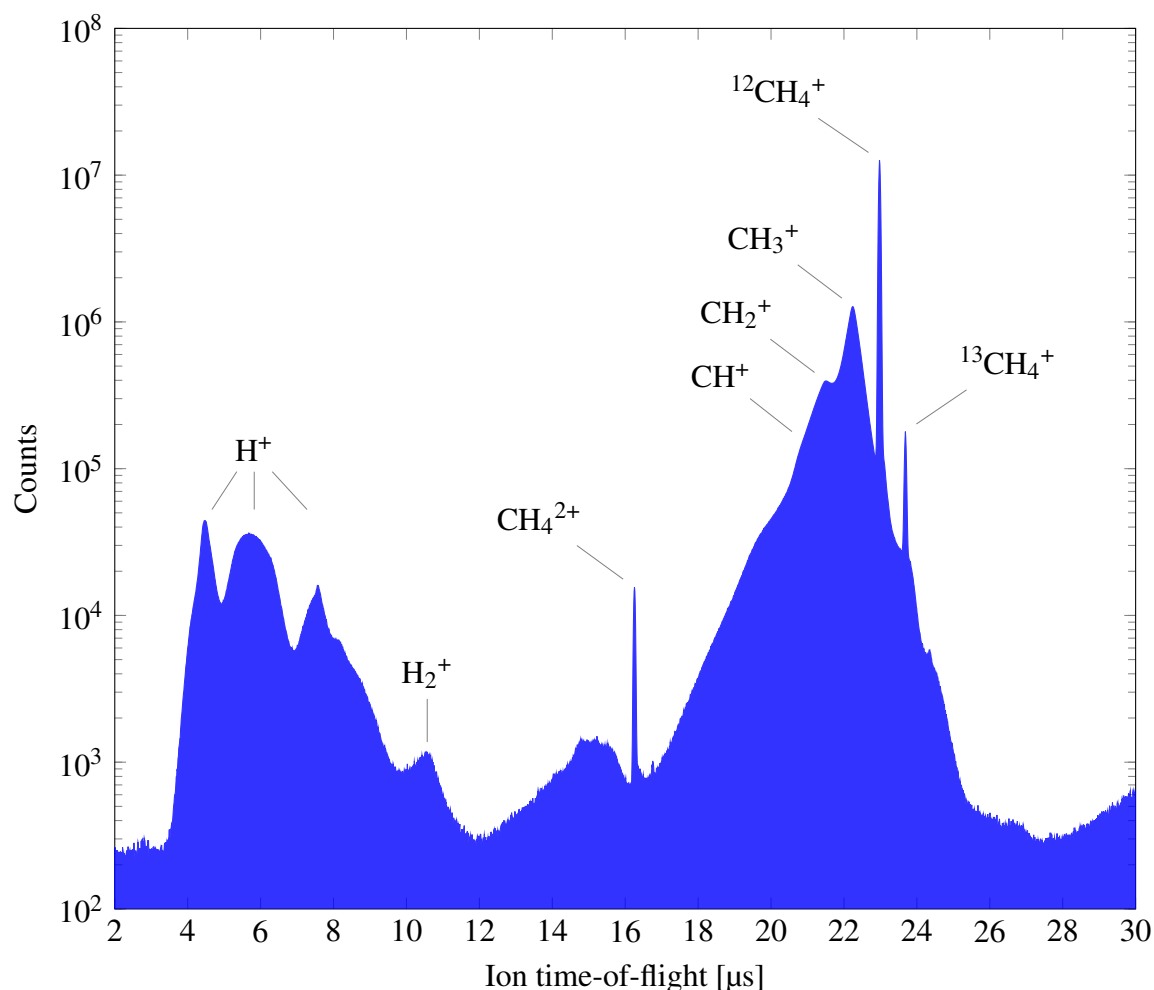

Figure 7.3: Raw time-of-flight spectrum of the two-color photoionization of methane. The most important peaks are marked.

of the CH_4^+ ion at around $23\,\mu s$ is sitting at the right edge of a broad multi-peak structure that is formed by the lighter fragment ions which lack one or more hydrogen atoms. In the logarithmic representation, the maxima of the CH^+, CH_2^+, and CH_3^+ can be located. Another sharp peak with about 1 % of the intensity of the CH_4^+ peak shows up right next to this one. It also corresponds to a CH_4^+ ion, but not containing the standard ^{12}C atom, but instead the heavier ^{13}C. The intensity ratio between the two CH_4^+ peaks corresponds to the natural isotope ratio between ^{12}C and ^{13}C. A contribution of methane containing a deuterium atom to the heavy CH_4^+ peak is possible, but can be neglected because the isotope ratio between ^1H and ^2H is about 10 000. Another sharp peak with a rather low intensity can be found at about $17\,\mu s$. This peak corresponds to the doubly charged CH_4^{2+} ion. At even smaller times-of-flight, different forms of hydrogen ions can be found. The molecular H_2^+ ion peaks at about $11\,\mu s$, while protons arrive in a broad time window between approximately 4 to $8\,\mu s$. The H^+ tof spectrum has a characteristic shape, which is also observed in other Remi experiments with hydrogen (see for example [58]). It consists of a central peak, and two outer peaks. The two outer peaks correspond to protons with

high kinetic energy, probably created in a Coulomb explosion process. The protons in the center peak have lower kinetic energy and are part of a reaction with another, in the reaction microscope not detectable, neutral fragment. Given this multitude of ionization products, it is worth thinking about the possible reaction channels which lead to the creation of each ion species. The easiest ionization channel is of course the single ionization without any further reaction of the molecular ion, which leads to the two CH_4^+ peaks in the time-of-flight spectrum. This channel can be analyzed best, because all ionization products can be detected, and most wrong coincidences can be efficiently removed. However, many more single ionization channels are imaginable with at least one neutral fragment involved. The analysis of these channels is more complicated, and wrong coincidences cannot be removed almost completely. By setting smart conditions for time-of-flight and the momenta of the detectable fragments, it is at least possible to remove obviously wrong coincidences. In addition, for fragment ions which lack more than one atom compared to the target molecule, it is impossible to determine in which form those missing atoms have left the ion. In the case of the CH_2^+ ion for example, this means that either two separate H atoms are missing or an H_2 molecule. An even more sophisticated role is played by the charged hydrogen fragments. In a perfectly evacuated reaction microscope with no background gas, the hydrogenous fragments have to stem from the methane molecule hit by the laser pulse. In reality, even after baking-out of the Remi, a certain amount of gas remains in the vacuum system. This residual gas mainly consists of molecular hydrogen and water vapor, which can both also interact with the laser and create hydrogen ions. In the case of double ionization of methane, there is also a large set of conceivable reaction channels. The easiest channel is again the double ionization without fragmentation. Slightly more complicated are Coulomb explosion channels where the doubly charged CH_4^{2+} ion splits up into two singly charged fragments, for example a CH_3^+ ion and a proton or a CH_2^+ ion and an H_2^+ molecular ion. All double ionization channels mentioned so far have the advantage that they do not involve any neutral fragments. But as can be seen from the time-of-flight spectrum, the double ionization cross section is much lower than the single ionization and the statistics will automatically be worse. In addition, even if a measurement of all ionization products is possible, it requires the detection of (at least) four particles, and with an estimated detection probability of about 50 % for one particle, the statistics is reduced even more drastically. Double ionization channels involving neutrals have not been looked at as the analysis would have become too complicated with no guarantee of being able to extract any information. Coulomb explosion channels can be identified by plotting the times-of-flight of both ions in a coincidence plot as in figure 7.4. In the time-of-flight coincidence spectrum, the Coulomb explosion events are lying on characteristic parabolas. The extrapolation of these parabolas to the diagonal of the graph leads to the time-of-flight of the doubly or multiply charged parent ion before the Coulomb explosion. The measurements reported in this thesis involved an extraction field of the Remi spectrometer of about $2\,\mathrm{V\,cm^{-1}}$. This relatively low field has the disadvantage of a poor acceptance for ions with high kinetic energies, especially if they are not initially emitted parallel to the spectrometer. This affects in particular the light fragment ions from Coulomb explosions (e.g. H^+ and H_2^+), as they carry most of the repulsion energy. If their transverse momentum component is too large, the ions cannot be guided to the detectors by the weak electric field and are lost. This effect can be observed in figure 7.4 as the two highlighted Coulomb explosion channels are not forming
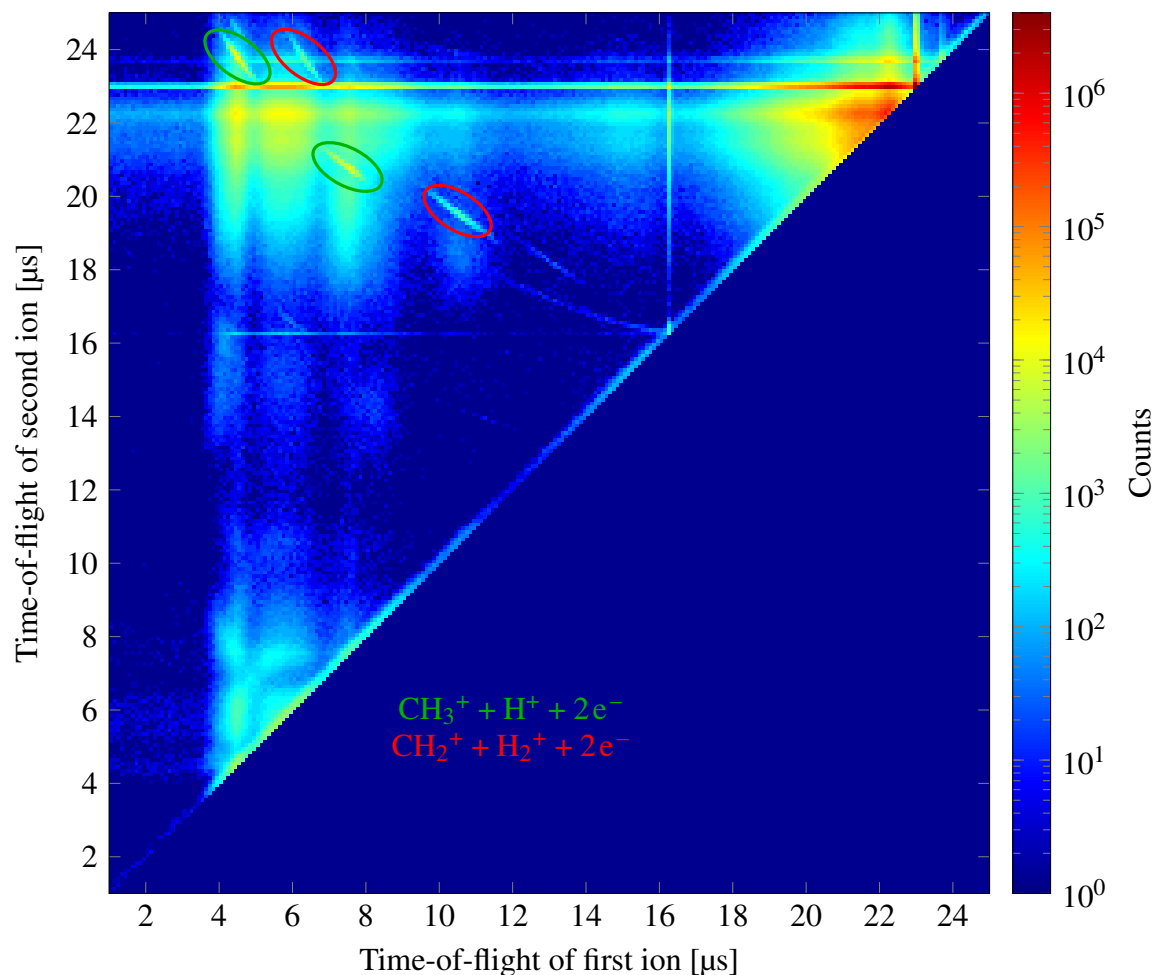
Figure 7.4: Ion-ion time-of-flight coincidence plot. Two Coulomb explosion channels are marked in green and red. In this representation, Coulomb explosion events lie on parabolic lines which intersect with the diagonal at the time of-flight corresponding to the multiply charged mother ion. For the two marked channels, this is the CH_4^{2+} ion. In the present dataset, the parabolas are not continuous because of the low electric extraction field in the reaction microscope causing the loss of ions with large transverse momentum. The faint parabola close to the diagonal is probably the trace of a metastable CH_4^{2+} ion, which has a lifetime before Coulomb explosion comparable to the time-of-flight.

a continuous parabola but instead two separated areas. Normally the ion time-of-flight spectrum of Coulomb explosion should cover the whole range between the two extreme times-of-flight, where the Coulomb energy is completely deposited to the longitudinal momentum component of the fragments. The two separate spots in figure 7.4 correspond exactly to this situation. Ion pairs with larger transverse momentum components would lie in the gaps in between, and most likely the lighter fragment is lost. The drawback of a low acceptance for ions with high kinetic energies is compensated by a very good energy resolution for the particles that are detected. Hence, the used Remi configuration is better suited for the investigation of low-energy phenomena. A list of the possible ionization channels of methane can be found in table 7.1.

single ionization	
$CH_4 + \gamma \longrightarrow$	$CH_4^+ + e^-$ $CH_3^+ + e^- + H$ $H^+ + e^- + CH_3$ $CH_2^+ + e^- + 2H$ $CH_2^+ + e^- + H_2$ ...
double ionization	
$CH_4 + \gamma \longrightarrow$	$CH_4^{2+} + 2e^-$ $CH_3^+ + H^+ + 2e^-$ $CH_2^+ + H_2^+ 2e^-$ ...

Table 7.1: List of certain possible single and double ionization channels of the methane molecule. The table only contains ions or channels that can be found in the present data. There are of course more possible ionization channels but their detection and analysis becomes more and more difficult. Note that the reaction microscope is only able to detect charged fragments.

7.2.2 Photoelectron spectra of CH_4^+, CH_3^+, and H^+

Since the statistics for the comparison of the double ionization channels, particularly of Coulomb explosion channels, was insufficient, the data analysis was focused on the analysis of electrons measured in coincidence with different methane fragment ions. As a starting point for this analysis, the 2-dimensional momentum distributions of electrons measured in coincidence with CH_4^+, CH_3^+, and H^+ were compared (see figure 7.5). Note that the distributions use different bin sizes for count statistics reason. The CH_4^+ distribution is in general sharper than the two other ones because the channel can be measured with a momentum sum coincidence condition. In the remaining channels, the coincidence condition only relies on the time-of-flight of the ion, which is weaker. In addition, the H^+ ions detected for the third spectrum can have several origin channels, blurring the spectrum even more. Despite the differences in the sharpness of the momentum distributions,
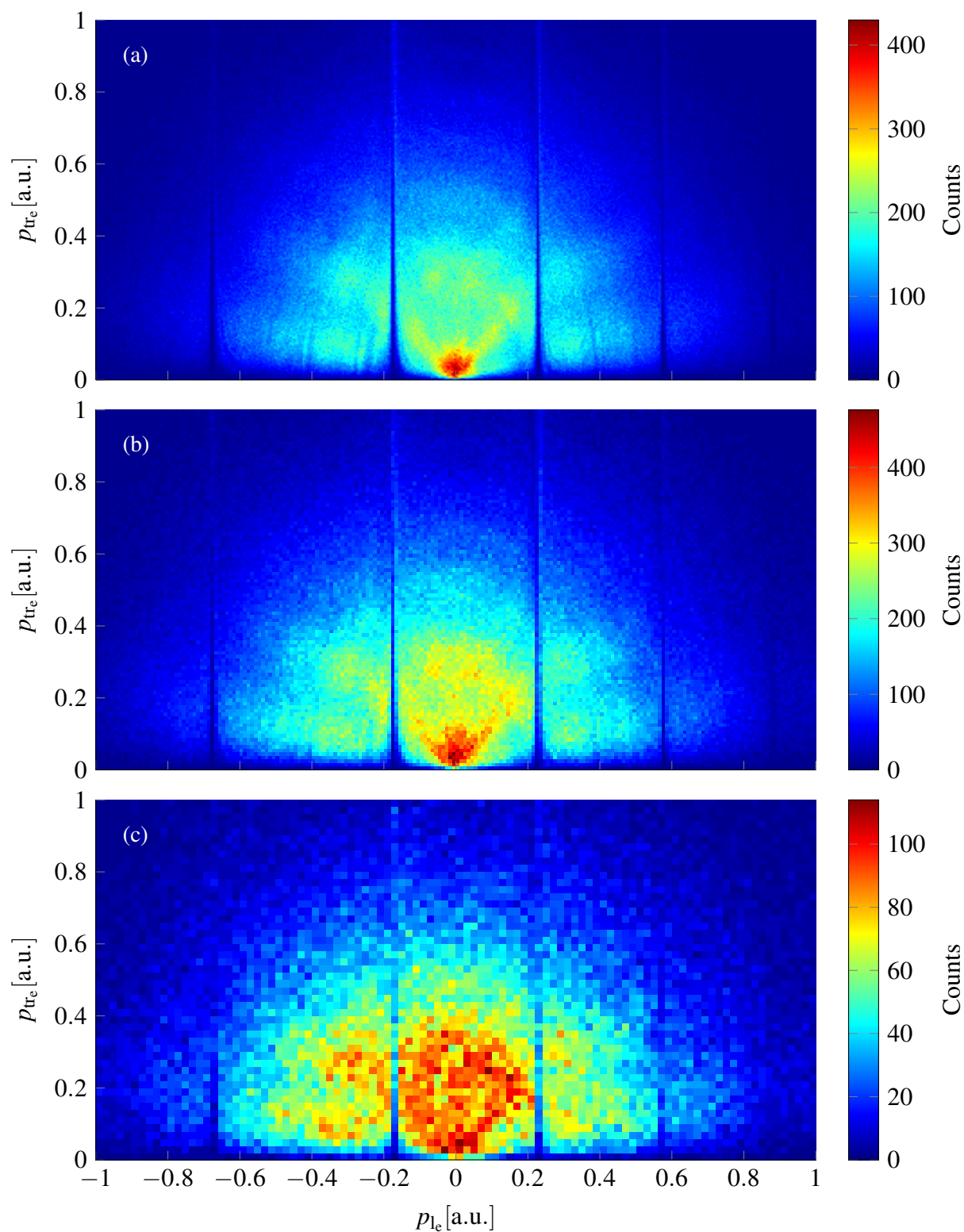
Figure 7.5: Photoelectron momentum spectra measured in coincidence with different CH_4 fragment ions: CH_4^+(a), CH_3^+(b), and H^+(c). The vertical lines at certain longitudinal momenta are the results of the cyclotron motion induced by the magnetic field.

all three spectra have in common a similar width with a maximum total momentum of about 0.8 a.u.. This value can be used to calculate an estimation of the laser intensity during the measurement using equation 4.12. For this particular measurement, the intensity lies at about $7.5 \times 10^{13}\,\mathrm{W\,cm^{-2}}$. Although looking similar at rather high momenta, the momentum distributions are clearly different from each other at very low momenta. The CH_4^+ photoelectrons seem to have a sharp maximum close to the origin. In the CH_3^+ case, this maximum seems to be still present but not as pronounced as in the previous case because structures of electrons with a total momentum of about 0.2 to 0.3 a.u. are showing up with a larger intensity compared to the maximum. The maximum at very low momenta is completely lost in the case of H^+ photoelectrons and there is a nearly constant intensity of electrons with momenta up to 0.3 a.u.. The differences in the momentum spectra are also visible in the kinetic energy spectra at very low energies below 0.2 eV. In fact, there is a clear peak structure at around 0.02 eV for electrons measured
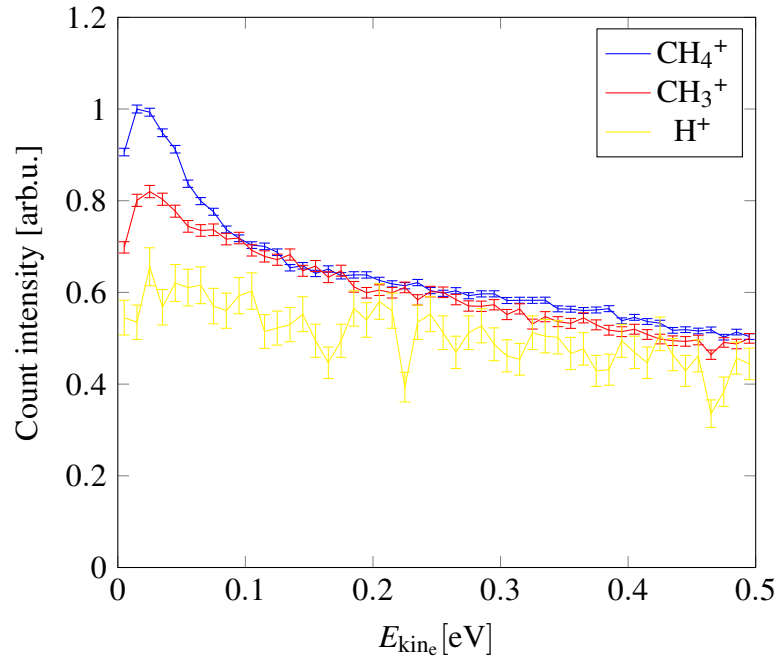
Figure 7.6: Kinetic energy spectra of photoelectrons measured in coincidence with different ions. The curves were scaled such that the spectra at high energies (beyond the energy range of this plot) have the same background levels.

in coincidence with a CH_4^+ ion. This peak is still present in the CH_3^+ photoelectron spectrum, although the peak height is lower. Furthermore, there are at least three more shoulders at the right flank of the low-energy peak, separated by about 0.02 to 0.03 eV. At least one of these shoulders can also be found for CH_3^+ photoelectrons at roughly 0.08 eV. The low-energy peak structure is not observed in the kinetic energy spectrum of H^+ photoelectrons. Contrary to the measurements of CH_4^+ and CH_3^+ ions, it is impossible to attribute an unambiguous ionization channel for the measured H^+ ions and so the final electron distribution is a superposition of every possible channel. However, since there is no indication of any low-energy peak below 0.5 eV in the spectrum, the existence

of such a structure can also be excluded for any of those channels, particularly for the dissociative ionization channel with the formation of an additional neutral CH_3 fragment. This channel is interesting because it represents the opposite case of the channel in which the $CH_3{}^+$ is created and where the electron is taken away from the larger fragment. As a remark about the data attributed to the measurement of $CH_3{}^+$ ions, it has to be recognized that a certain amount of the registered events can actually be falsely identified $CH_2{}^+$ and even a few CH^+ ions, because the ion species have a certain overlap in the time-of-flight spectrum (see figure 7.3). The data were selected such that the momentum of the assumed $CH_3{}^+$ was small meaning that only events close to the center of the $CH_3{}^+$ time-of-flight peak are taken into account. The contribution of $CH_2{}^+$ (and lighter ions) to counts at this peak can be estimated to be about one order of magnitude less than the contribution of the correct $CH_3{}^+$ ions, as can be seen in the time-of-flight spectrum.

The differences observed in the electron data are in contradiction to the two-step model described in section 4.3 and [37]. According to this model, the ionization and the release of the electron occurs in the first step. Any further interaction with the electric field of the laser leading to dissociation happens in the second step when the electron is already far away and so it should not be influenced by the laser-ion interaction. This would necessarily mean that the final state of the electron, which is represented by the measured momentum and kinetic energy distributions, should be the same, regardless of the corresponding ion. Since there are obvious differences, the two-step model might be false or at least incomplete, and further analysis is needed. To this end, the measurements of $CH_4{}^+$ ions and $CH_3{}^+$ ions on the one hand and the measurements of H^+ ions on the other hand can be opposed and compared to each other. The most obvious difference between these two branches is the type of ion that is created during the reaction. In the first case, the ion is of molecular kind whereas the H^+ ion is an atomic ion, in fact just a bare proton in this specific case. The differences in the respective electron momentum and kinetic energy distributions could contain information about the underlying ionization and dissociation mechanisms that lead to the formation of either a molecular ion or an atomic ion.

7.3   Parenthesis: Two-color photoionization of hydrogen

The results in the kinetic energy spectra of the photoelectrons are very similar to recent results observed in an experiment with the same setup and molecular hydrogen as the target [1]. In comparison to methane, the hydrogen experiment has the advantage that the outcome of the experiment is much less complicated and that hydrogen, as the simplest molecular system, has already been studied extensively. For the single ionization of hydrogen, there are only two possible reaction channels. Either there is no dissociation and an $H_2{}^+$ ion is created, or the molecule dissociates and a neutral H atom and a proton are created. The first channel is called bound ionization, the second one dissociative ionization. Again, according to the two-step model, the photoelectrons from either channel should be in the same final state. However there are differences both in the momentum and kinetic energy distributions between bound and dissociative ionization (see figure 7.7). Similar to the results of the methane experiment, the case in which a molecu-
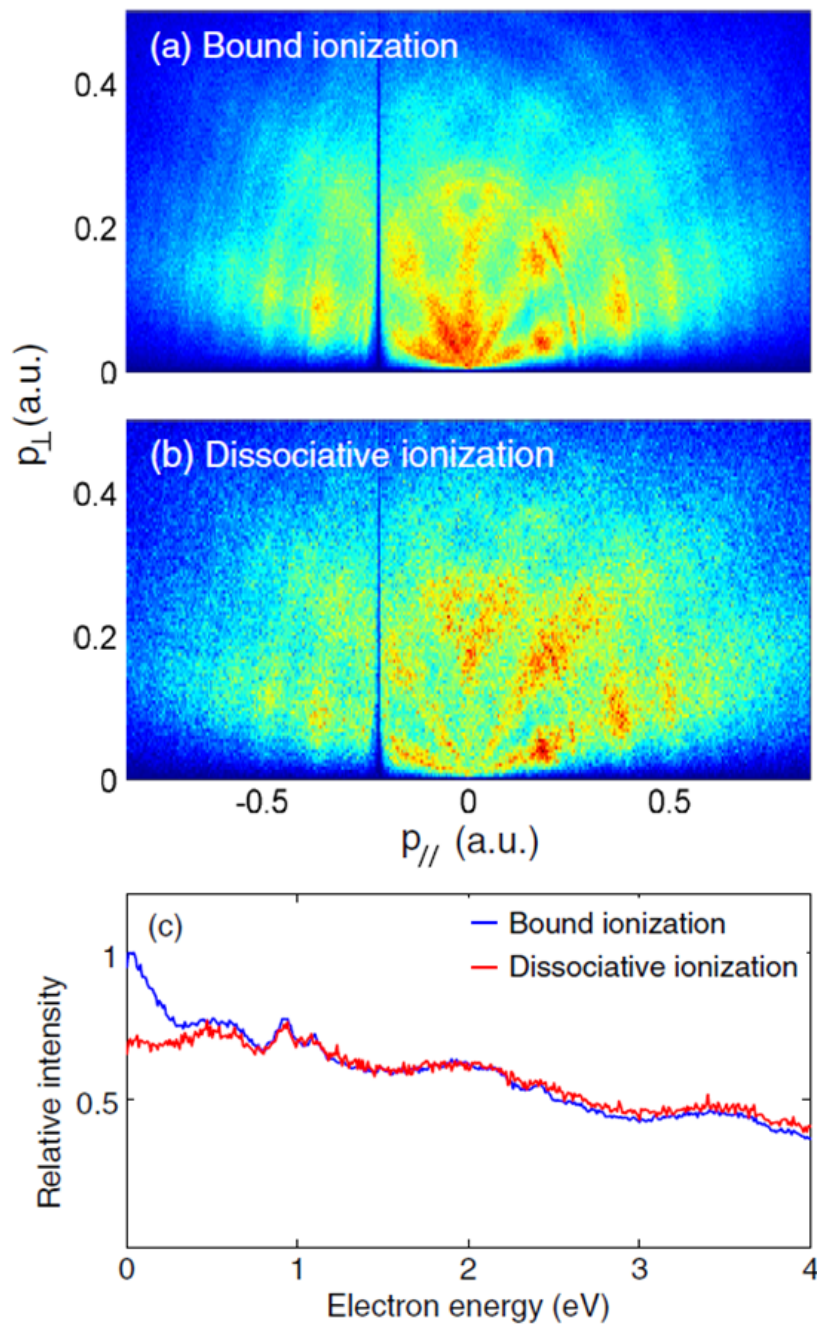
Figure 7.7: Photoelectron momentum and kinetic energy distributions of the two-color ionization of H_2 for the bound and dissociative channels, respectively (taken from [1]).

lar ion is formed exhibits a peak at low kinetic energies, and there is no such peak when only a proton is detected. For the results of the hydrogen experiment, an explanation that resolves the contradiction to the two-step model could be developed. In this model, the bound ionization takes a different pathway via an excited autoionizing state. Instead of directly ionizing the molecule in the first step, the laser pulse promotes the electron to a high-lying Rydberg state. The series of H_2 Rydberg states and their energy levels have been studied in [145–147]. The potential energy curves of these excited H_2^* states are lying slightly below the potential energy curve of the bound state of the molecular ion. At first sight, it seems that autoionization from such a state is forbidden. However, if the H_2^* state is excited vibrationally at the same time, its energy lies above the ionization threshold. From this electronically and vibrationally excited state autoionization is possible. The excess energy is in the order of the vibrational sublevels and it is transferred to the released electron. Since the states of the Rydberg series with vibrational excitation v converge to the bound H_2^+ state ($1s\sigma_g$) with the same vibrational quantum number v, their energy remains below the energy of the dissociative H_2^+ potential energy curve ($2p\sigma_u$). Therefore, the ionization mechanism via autoionization from a state with simultaneous electronic and vibrational excitation is an option only for the bound ionization channel. The potential energy curves and the relevant states for the comparison between the common two-step model and the proposed ionization mechanism are displayed in figure 7.8. Figure 7.9 shows the contributions to the autoionization process by various Rydberg states, which could be identified with the help of previous work [145–150]. The identified autoionization transitions are in agreement with the propensity rule, which states that autoionization by vibrational relaxation is most likely happening for transitions where the vibrational quantum numbers differ by 1 [146, 151, 152]:

$$\Delta v = v' - v = 1. \tag{7.1}$$

The alternative ionization mechanism via vibrational autoionization was also confirmed by analyzing for electrons of both ionization channels the longitudinal momentum asymmetry as a function of the two-color laser phase. In the two-step model, the electron is released early and is itself interacting with the laser field. A change of the pulse shape, induced by a relative phase shift between the IR and the SHG pulses should therefore also have an influence on the final state of the free electron. As a result, there should be a significant phase-dependent asymmetry. On the other hand, the lifetimes of the Rydberg states involved in the autoionization mechanism are longer than hundreds of femtoseconds, which means that the electron is released long after the electric field of the laser pulse has faded away. Electrons from this mechanism should not exhibit a strong asymmetry. Figure 7.10 shows the two-dimensional representation of the asymmetry function, which is not just depending on the two-color phase, as in equation 6.20, but also on the kinetic energy of the electrons. The two-dimensional function still compares the number of electrons with positive longitudinal momentum to the number of electrons with negative longitudinal momentum:

$$\tilde{A}(E_{\mathrm{kin_e}}, \varphi) = \frac{n_+(E_{\mathrm{kin_e}}, \varphi) - n_-(E_{\mathrm{kin_e}}, \varphi)}{n_+(E_{\mathrm{kin_e}}, \varphi) + n_-(E_{\mathrm{kin_e}}, \varphi)}. \tag{7.2}$$
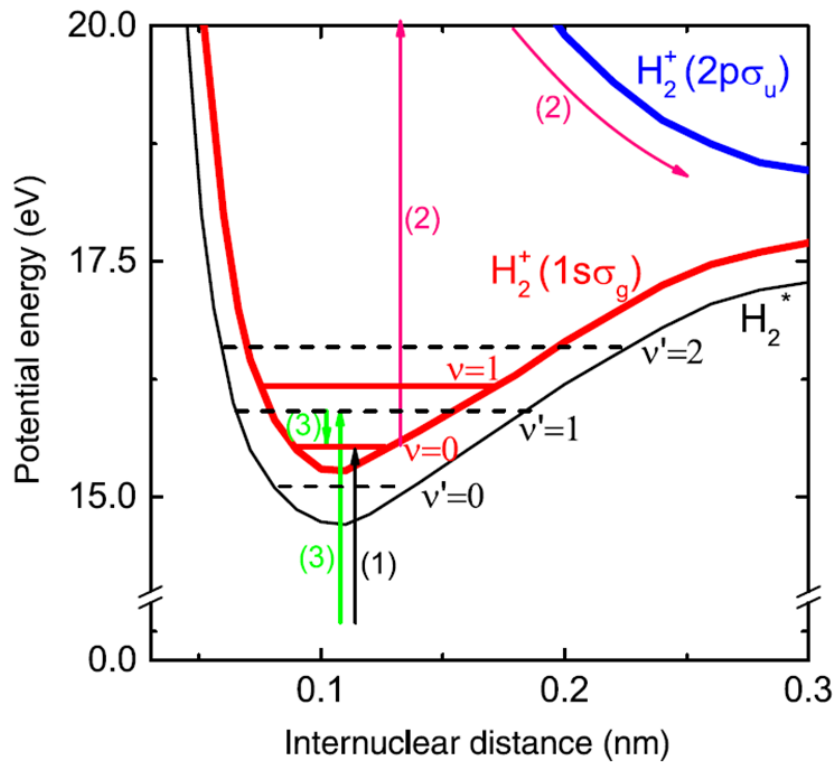
Figure 7.8: Comparison between photoionization of H_2 according to the two-step model (1,2) and via autoionization from a vibrationally excited Rydberg state (3). In the two-step model, the molecule is initially ionized (1). The dissociation is the result of further interaction with the laser field in step (2) promoting the system from the bound $1s\sigma_g$ state of the H_2^+ ion to the dissociative $2p\sigma_u$ state. In the alternative mechanism, the molecule is excited to a Rydberg state H_2^* with simultaneous vibrational excitation, from which autoionization to the $1s\sigma_g$ state is possible (taken from [1]).

At first glance, the two graphics in figure 7.10 look quite similar. As expected, the distributions are 2π-periodic with the phase of the two-color field. By taking each line of the matrices separately and fitting a sinusoidal function to the data points, the asymmetry amplitudes and offset phases could be retrieved for each kinetic energy value. In the phase offset, there was no significant difference between the two channels, which can already be seen in the two-dimensional graph. The asymmetry amplitudes of the two channels show a significant difference just in the energy range of the electrons from vibrational autoionization (see figure 7.11). The lower amplitude of the bound channel indicates that these electrons are less affected by the asymmetric laser field, which supports the hypothesis of a long-living intermediate state that is involved in the process of bound ionization. The fact that also in the bound case, there is a certain amount of asymmetry, could suggest that both mechanisms, the two-step model and the vibrational autoionization, contribute to it.
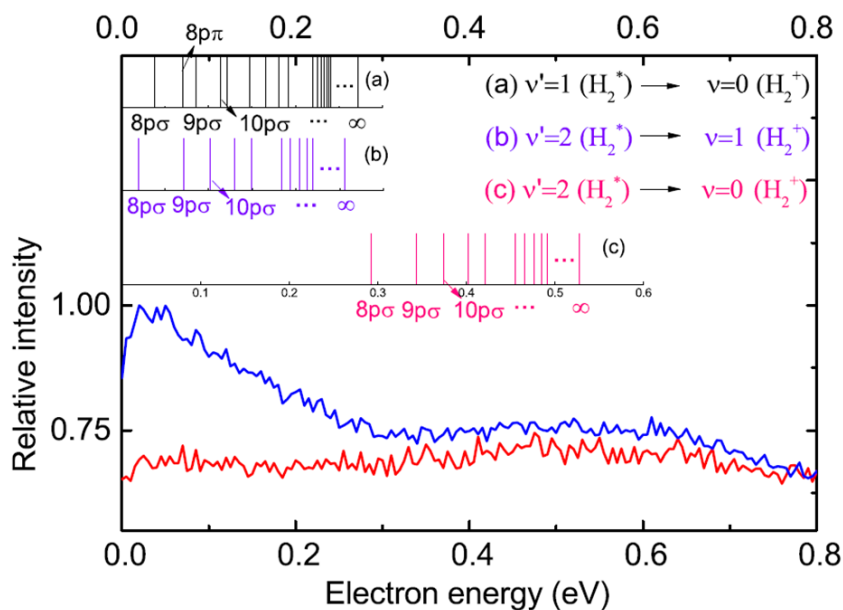
Figure 7.9: Transition energies for vibrational autoionization of H_2 from various Rydberg states to the $1s\sigma_g$ state of H_2^+ with $\Delta v = 1$ ((a) and (b)) and with $\Delta v = 2$ (c). Below are the electron kinetic energy distributions of the bound (blue curve) and dissociative ionization channels (red). The low-energy peak in the bound channel is mainly formed by photoelectrons from autoionization transitions with $\Delta v = 1$ (taken from [1]).
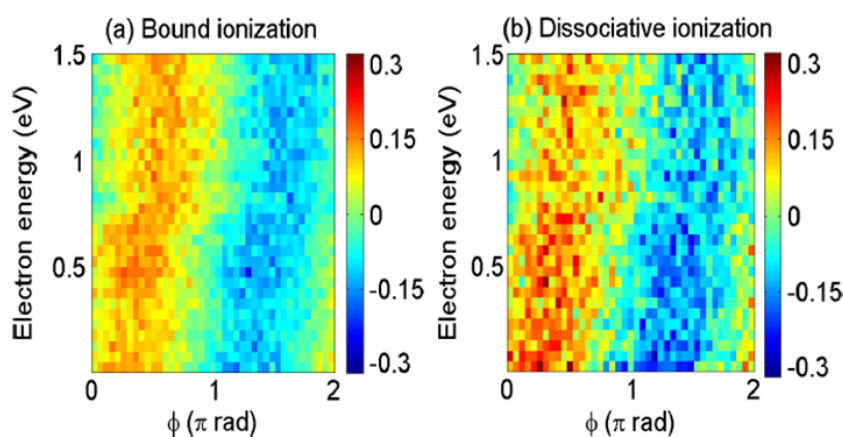
Figure 7.10: Phase- and energy-dependent momentum asymmetries of the bound and dissociative ionization channels of H_2 (taken from [1]).
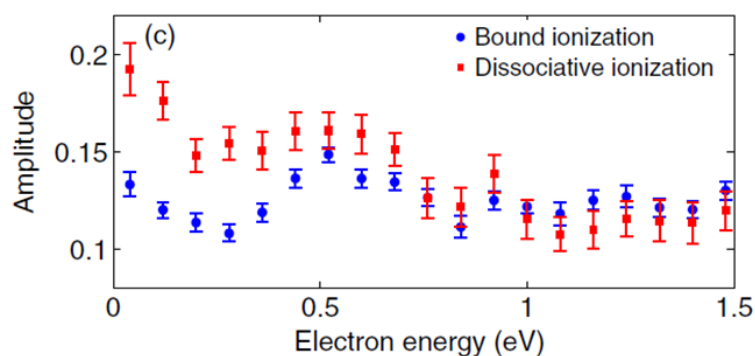
Figure 7.11: Comparison of the asymmetry amplitudes of electrons from bound and dissociative ionization of H_2 (taken from [1]).

7.4 Comparison of ionization channels of methane

The enhancement of electrons with low kinetic energies in certain ionization channels of methane (see figure 7.6) is similar to the findings in hydrogen and also in contradiction to the two-step model. Consequently, the goal of the further analysis of the CH_4 measurements was to find out if this could be explained by an alternative mechanism. The same analysis pathway was taken by first comparing the phase- and energy-resolved momentum asymmetries. The asymmetries are shown in figure 7.12. Due to the low count statistics of the H^+ photoelectrons, the asymmetry is plotted twice in figures 7.12c and 7.12d with different phase bin sizes. The comparison of the asymmetry amplitudes is plotted in figure 7.13a. Within the error bars there is no difference between the three channels, but there is a general trend that the amplitudes are increasing at higher electron energies. Similarly, the offset phase of the sinusoidal asymmetry function shows the same energy dependence for each channel, as can be seen in figure 7.13b. The curves are nearly identical within error bars. Interestingly, the phase offset is decreasing from about 1 rad to 0.3 rad in the range from 0 to 0.5 eV and remains constant beyond that energy. This trend is also observable in figure 7.12, where the distributions shift to the left below 0.5 eV. Although there is no obvious difference between the three channels, there is a clear difference between electrons below about 0.5 eV and electrons above. The different phase offset could be a hint to a different ionization mechanism for low energy electrons, probably involving an intermediate state with a lifetime shorter than the pulse duration. Due to the bad statistics of the H^+ photoelectrons and also because numerous ionization channels can lead to the production of a proton, a profound conclusion about these electrons is difficult to draw. To proceed with the analysis, the photoelectrons measured in coincidence with the molecular ions look more promising. In contrast to the results of the H_2 photoionization experiment, in the CH_4 data, there is no such convincing evidence for the alternative ionization mechanism so far. The low-energy peak, which was only observed in the electron spectra of the CH_4^+ and CH_3^+ ions, could suggest that there is a connection to the molecular nature and that an intermediate state with vibrational excitation could be involved.
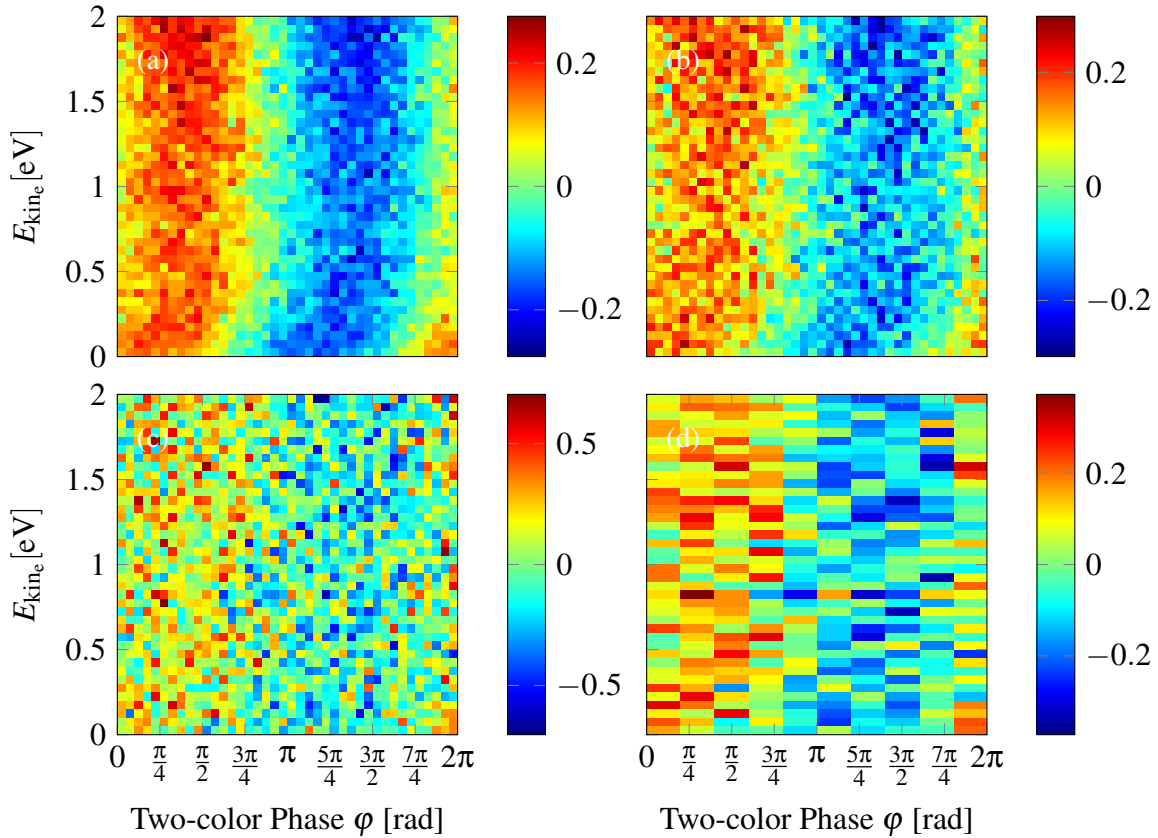
Figure 7.12: Phase- and energy-resolved longitudinal momentum asymmetries of photo-electrons measured in coincidence with CH_4^+ (a), CH_3^+ (b) and H^+ ions (c and d with lower phase resolution).

7.4.1 Methane photoionization at higher intensity

In order to have a broader set of data, the experiment was repeated with a higher laser intensity. The electron momentum (Figure 7.14) and kinetic energy spectra (Figure 7.15) look different to the results from lower intensity. The momentum distributions are broader, as can be expected from a higher intensity. From the width of the spectrum, an intensity of $1.1 \times 10^{14}\,\mathrm{W\,cm^{-2}}$ can be estimated. In figure 7.14, the vertical lines due to the cyclotron motion of the electrons in the magnetic field of the Remi are unusually broad, as compared to other measurements, for example the one with lower intensity (figure 7.5). The reason for this phenomenon could not be determined, but likely, the count rate was too high due to the laser intensity and the density of the gas jet. As all electrons return to their initial x- and y-positions after a full cyclotron cycle, they arrive at the same spot on the detector and this particular detector region is then blind for many electrons who arrive simultaneously with another one. All three electron distributions have the highest count density in a region with nearly vanishing longitudinal momentum and a transverse momentum of about 0.3 a.u.. In the electron spectra from molecular ions, below that region of highest count intensity, there is also a vertical structure of electrons with a total momentum much closer to zero. This vertical structure of low-momentum electrons is much less pronounced in the H^+ electron distribution. The maximum total
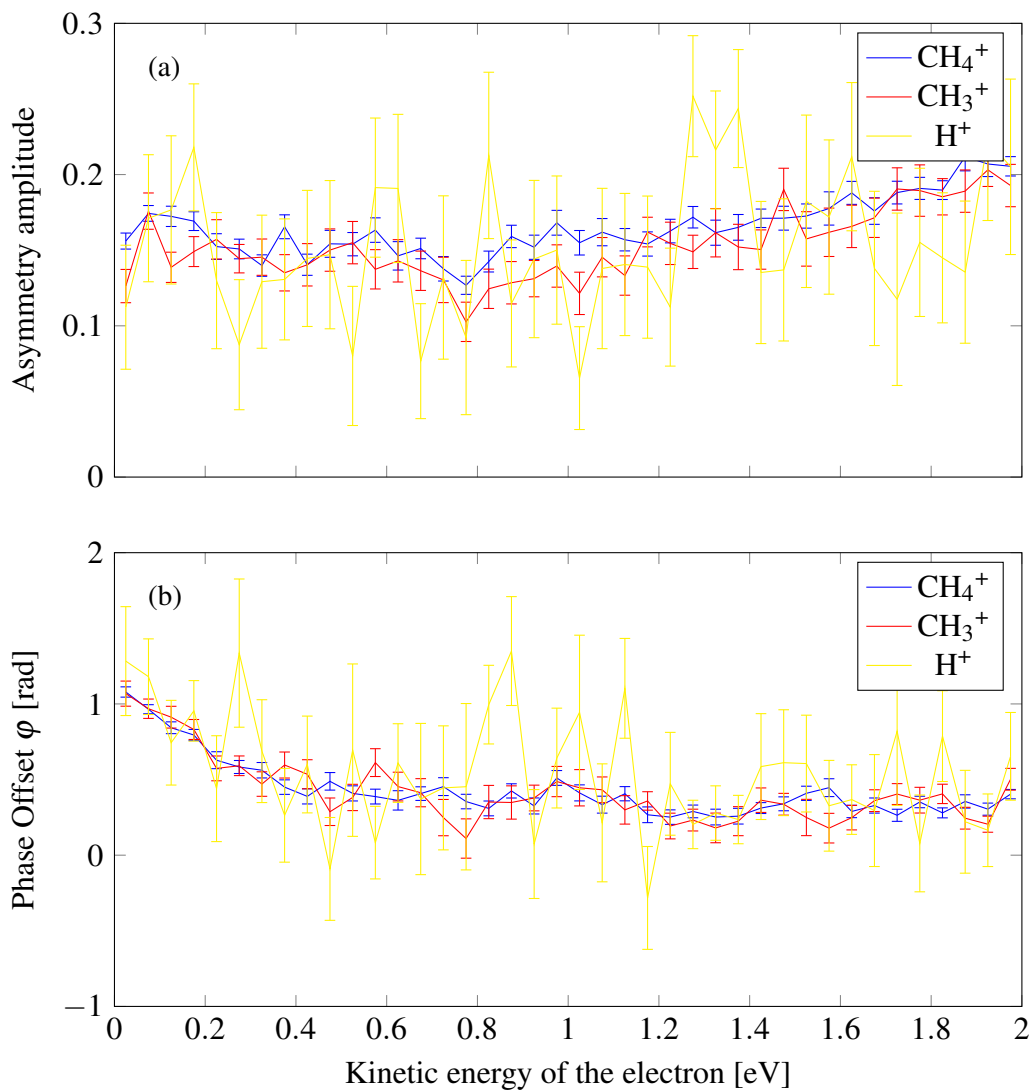
Figure 7.13: Amplitude (a) and phase offset (b) of the electron momentum assymetry obtained from a sinusoidal fit for each energy value for photelectrons detected in coincidence with CH_4^+ (blue), CH_3^+ (red), and H^+ (yellow). The electrons from the three ion species follow the same trend within error bars in both amplitude and phase offset. The amplitude is increasing at higher energies indicating that those electrons are more strongly influenced by the asymmetry of the two-color field. The phase offset is decreasing from 0 to $0.5\,eV$, and remains nearly constant at higher energies. This also supports the assumption that the low energy electrons interact differently with the asymmetric two-color field compared to electrons with higher kinetic energy.The phase shift could indicate the existence of an intermediate state which decays and causes the electron release before the end of the laser pulse.
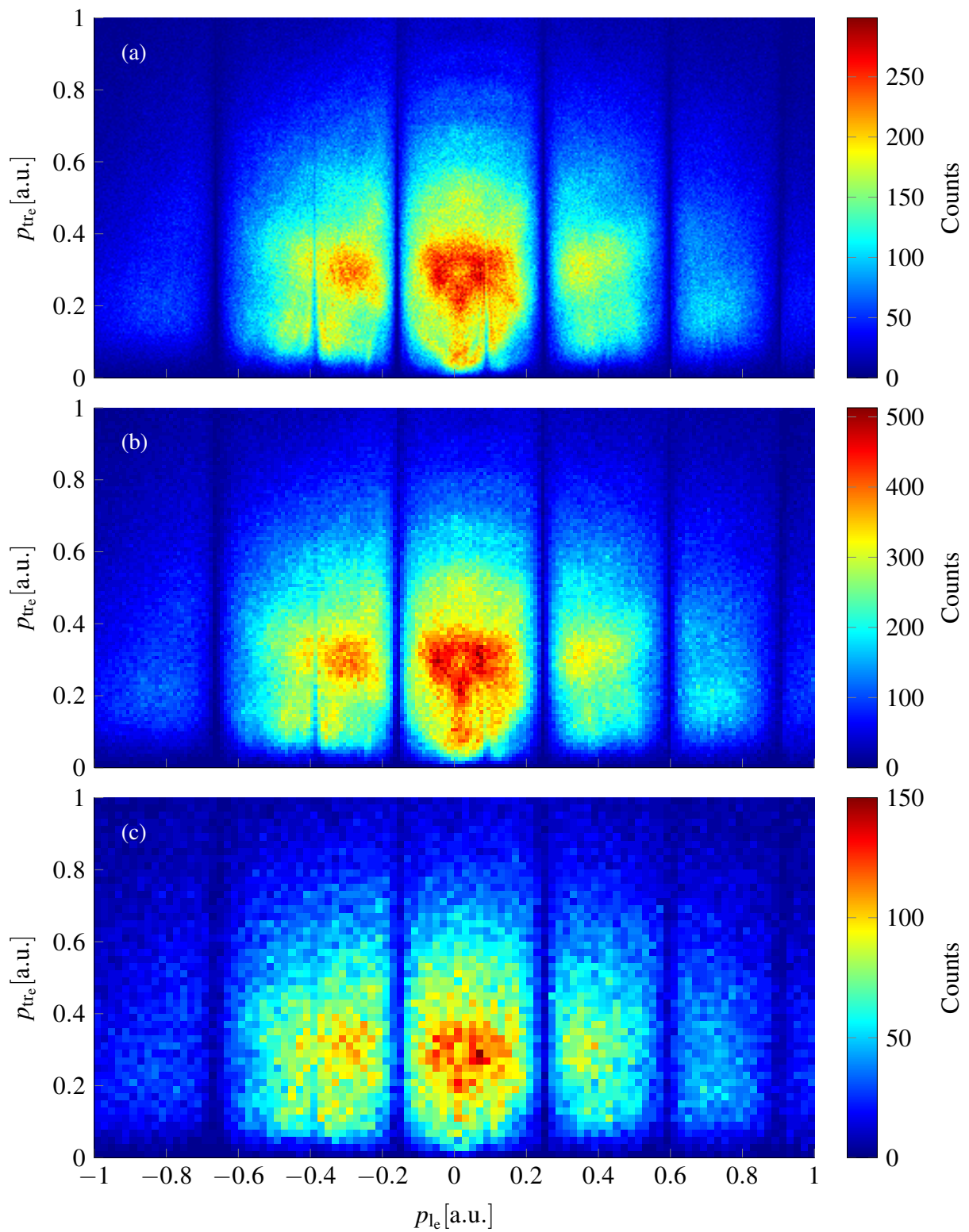
Figure 7.14: Photoelectron momentum distributions in coincidence with CH_4^+ (7.14a), CH_3^+ (7.14b) and H^+ (7.14a) ions at an approximate intensity of $1.1 \times 10^{14}\,W\,cm^{-2}$.

momentum of 0.2 a.u. of electrons within this structure corresponds to a maximum kinetic energy of about 0.55 eV. As the maximum is not anymore located at the origin of the 2D-momentum distribution, the low-energy peak has disappeared for all ion species. Nevertheless, the relative intensity of electrons with energies below 0.1 eV is higher for electrons detected in coincidence with CH_4^+ or CH_3^+ ions than H^+ electrons, in analogy to the results with lower intensity. The stronger suppression of low-energy electrons in
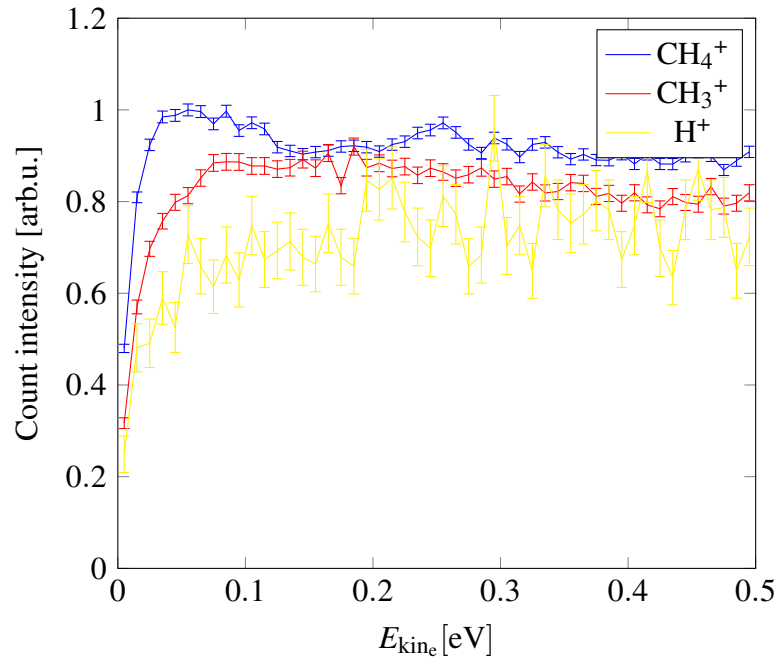
Figure 7.15: Energy spectra of photoelectrons measured in coincidence with CH_4^+ (blue), CH_3^+ (red), and H^+ (yellow) at a peak intensity of $\sim 1.1 \times 10^{14}\,W\,cm^{-2}$. Compared to the experiment with a weaker two-color pulse, the low-energy electron signal is suppressed.

coincidence with protons still allows the conclusion that the ionization process leading to CH_4^+ (and CH_3^+) ions is fundamentally different from the one leading to H^+ ions, or at least that there is a possible alternative process to the two-step mechanism.

7.4.2 Fallback to the argon-methane mixture

At this point, falling back to the experiments with the argon-methane mixture, whose analysis was initially skipped, was useful to substantiate the hypothesis of intermediate vibrational excitation in the process of molecular photoionization. The comparison of the low-energy electrons of the Ar^+ and CH_4^+ ions show clear differences between those from the atomic argon and the molecular methane. The two-dimensional photoelectron momentum distributions are plotted in 7.16. The intense signal of CH_4^+ photoelectrons at low momenta, especially the contrast of momenta below and above 0.1 a.u., is not that
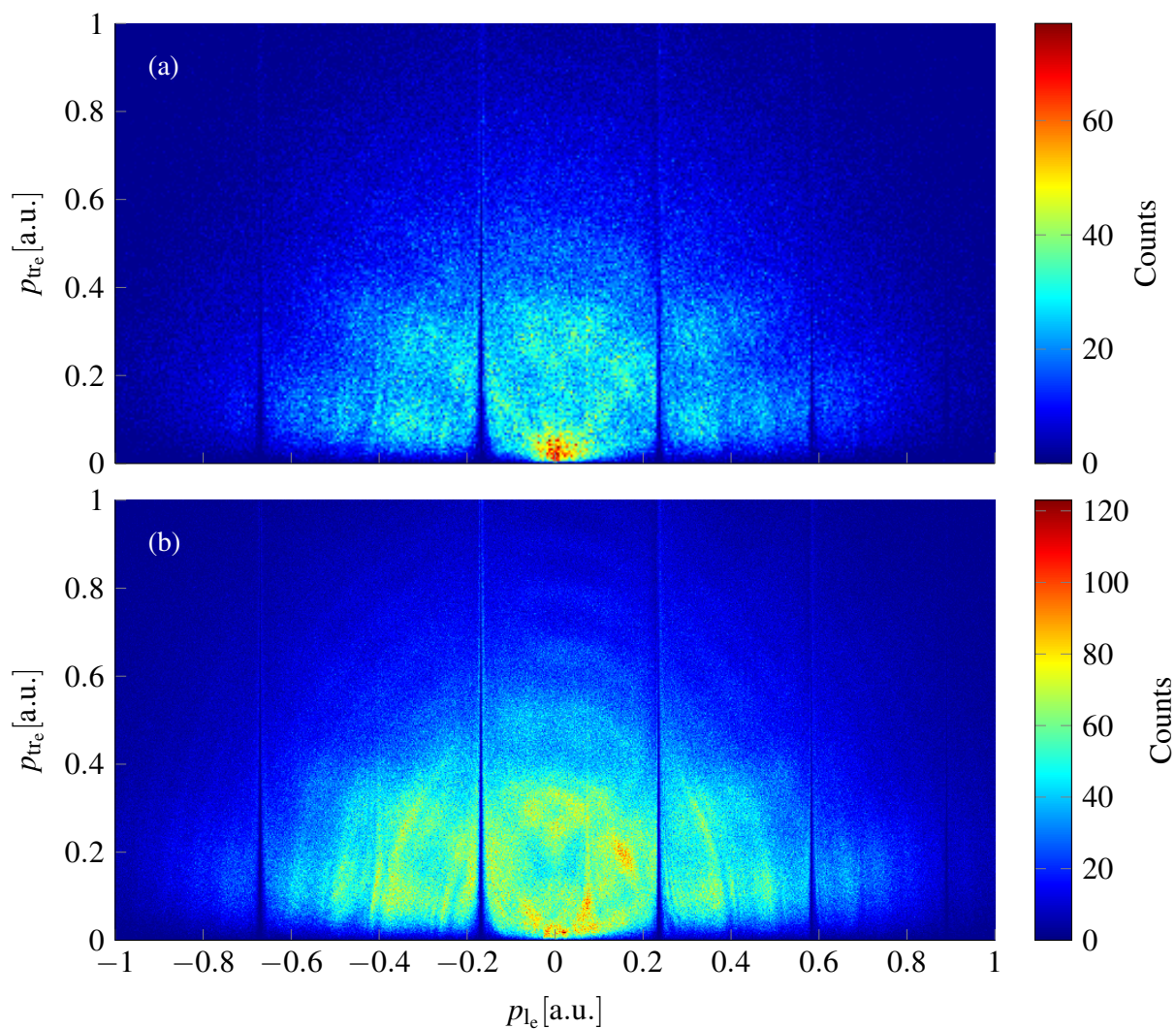
Figure 7.16: Photoelectron momentum spectra of electrons measured in coincidence with CH_4^+ (a) or Ar^+ ions (b) in a simultaneous measurement of both target gases mixed together. The CH_4^+ electron distribution looks very similar to the distribution from the measurement with pure methane (see figure 7.5a), as expected, with a clear enhancement at total momenta below 0.1 a.u.. In the Ar^+ electron distribution, there is a much broader momentum range with similar intensity up to about 0.4 a.u..

clearly present in the Ar$^+$ electron distribution. The argon distribution is much better resolved due to the higher gas concentration and many more fan- and ringlike features show up, which are for example explained in [58]. In the kinetic energy spectra, the difference between Ar$^+$ and CH$_4^+$ photoelectrons becomes much more obvious (see figure 7.17). In analogy to the analysis of the experiments with other target gases, the asymmetry
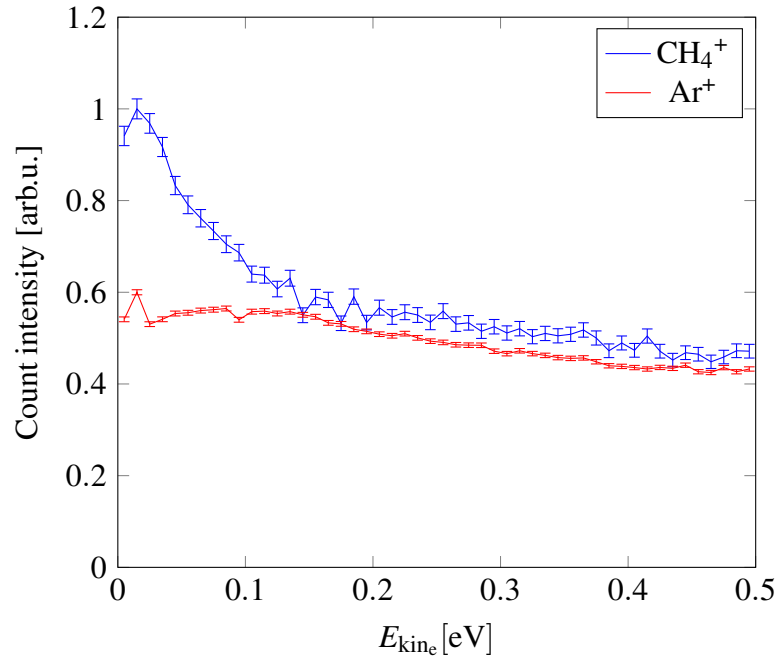
Figure 7.17: Kinetic energy spectra of CH$_4^+$ (blue) and Ar$^+$ photoelectrons (red). A low-energy amplification only exists in the methane case.

behavior is compared. The offset phases of the asymmetry function have a nearly constant
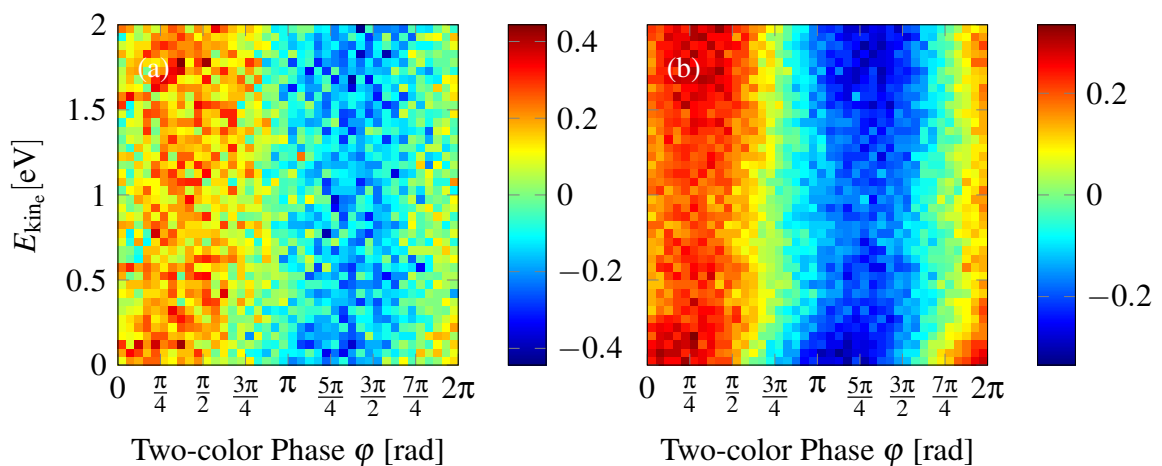
Figure 7.18: Phase- and energy-resolved longitudinal momentum asymmetries of photoelectrons measured in coincidence with CH$_4^+$ (a), and Ar$^+$ (b).

difference for all energies, the CH$_4^+$ data are shifted to the left by a phase difference of

about $\frac{\pi}{10}$, which is consistent with figure 7.2. The asymmetry amplitude is much more energy-dependent, as is shown in figure 7.19. The amplitude is in general higher for
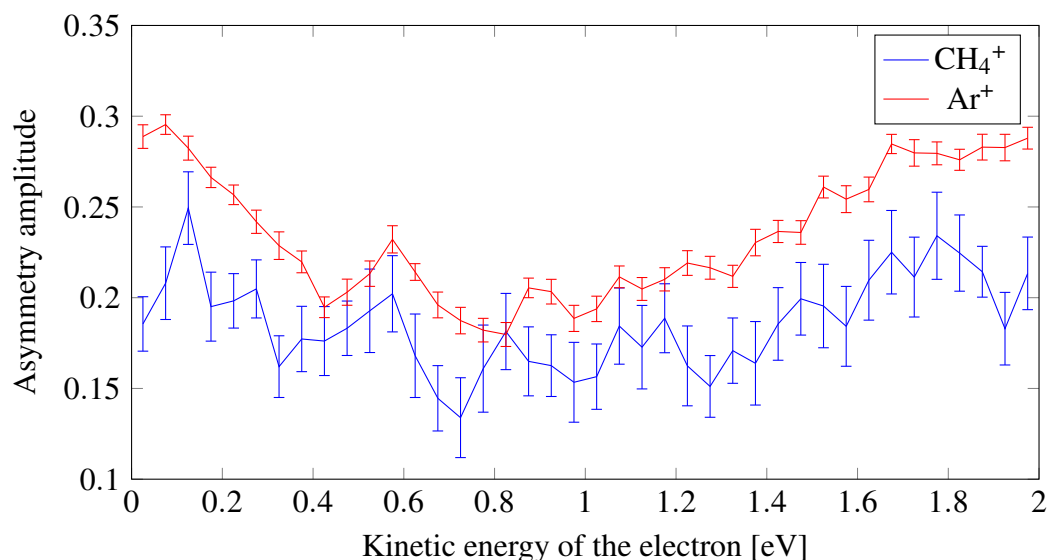
Figure 7.19: Energy-dependent amplitude of the photoelectron asymmetry of CH_4^+ (blue) and Ar^+ (red).

argon electrons, but especially at low energies below $0.2\,eV$, the difference between the two curves is increasing. This is again a hint that the CH_4^+ electrons in this energy range are less affected by the laser field, possibly because they are released at a later time from a metastable excited state.

7.5 Verification of alternative ionization mechanism

7.5.1 Analysis of the low-energy electron spectra

At this stage, there are certain indications for an ionization mechanism of CH_4 that differs from the two-step model. The low-energy peak is only found for electrons measured in coincidence with a molecular ion, but not for electrons measured together with proton fragments from the methane molecule. And the fact that the low-energy peak is not detected in the electron spectra of the singly charged ion of the atomic Ar target leads to the assumption that the origin of the peak lies in the molecular nature of the CH_4 system. The mechanism of autoionization from a vibrationally excited Rydberg state, which was proposed and proven for molecular hydrogen, looks appealing also for the interpretation of the methane measurement. To further substantiate this hypothesis, the structure of the low-energy peak of the CH_4^+ and CH_3^+ photoelectrons has to be investigated in more detail. Figure 7.20 displays the two peaks. The H^+ photoelectrons are not part of

the following discussion because there was no particular low-energy peak in the electron spectrum measured in coincidence with protonic fragments. The two peaks are quite dif-
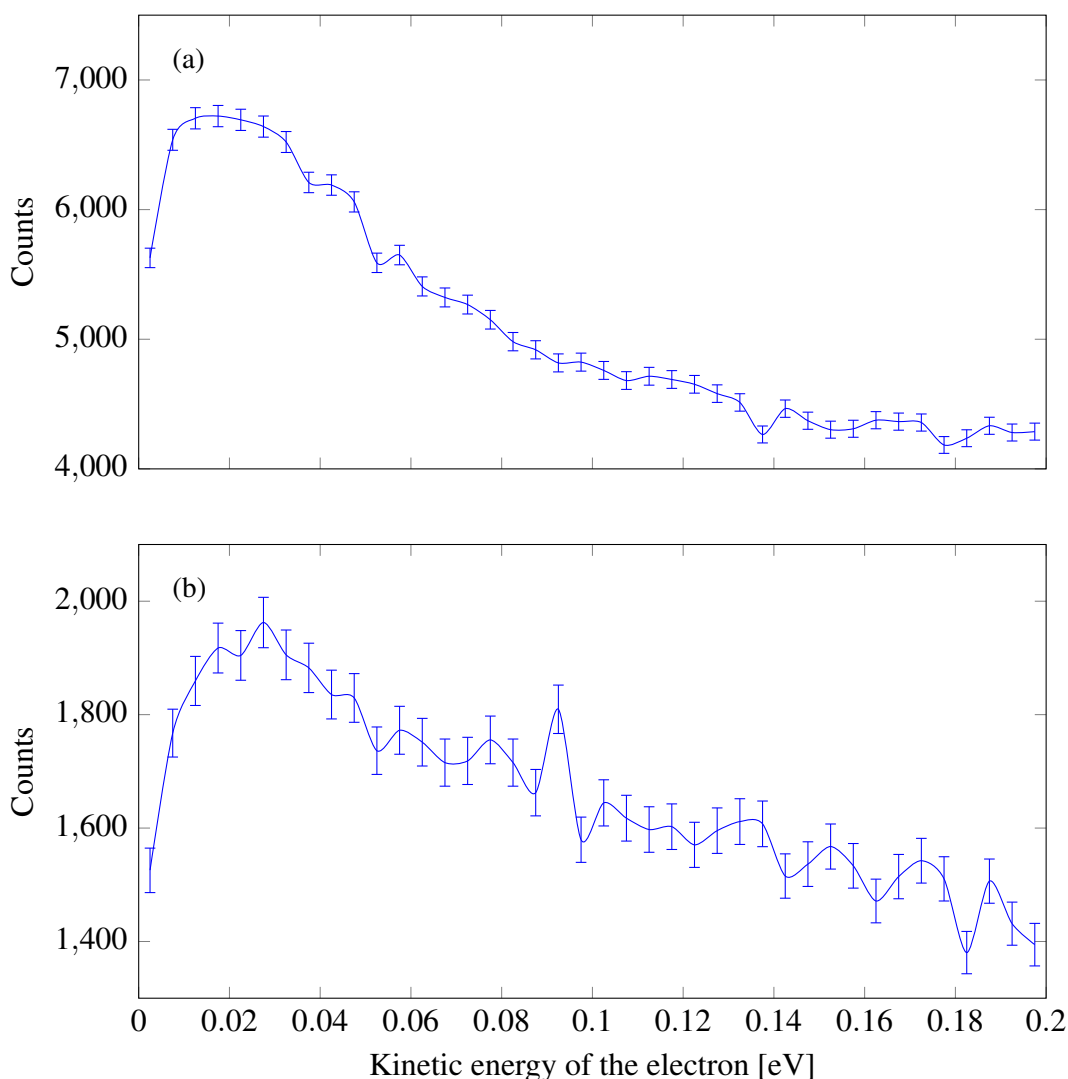
Figure 7.20: Low-energy photoelectron yields in coincidence with CH_4^+ (a) and CH_3^+ (b) cations. The data belong to the measurement presented in the beginning of this chapter with an approximate intensity of $7.5 \times 10^{13}\,\mathrm{W\,cm^{-2}}$.

ferent from each other. The CH_4^+ electron peak consists of the main maximum from 0.01 to 0.03 eV and at least two additional humps at 0.04 and 0.055 eV. Besides that, it looks much smoother than the CH_3^+ peak. There is a stronger rippling on the kinetic energy distribution of the CH_3^+ electrons, and apart from a pronounced spike at ∼0.09 eV, there are many oscillations with a spacing of about 20 meV in the range from 0.04 to 0.2 eV. In order to exclude that the rippling is just a statistical phenomenon, the data are compared to a second measurement performed under similar conditions, i.e. with comparable laser intensity of roughly $7.5 \times 10^{13}\,\mathrm{W\,cm^{-2}}$ (see figure 7.21). The pronounced humps in the falling edge of the CH_4^+ peak are smeared out in the second measurement but there are still visible shoulders. The main characteristics of the CH_3^+ electron distribution below 100 meV are featured in both figures, which allows the conclusion that the maxima at
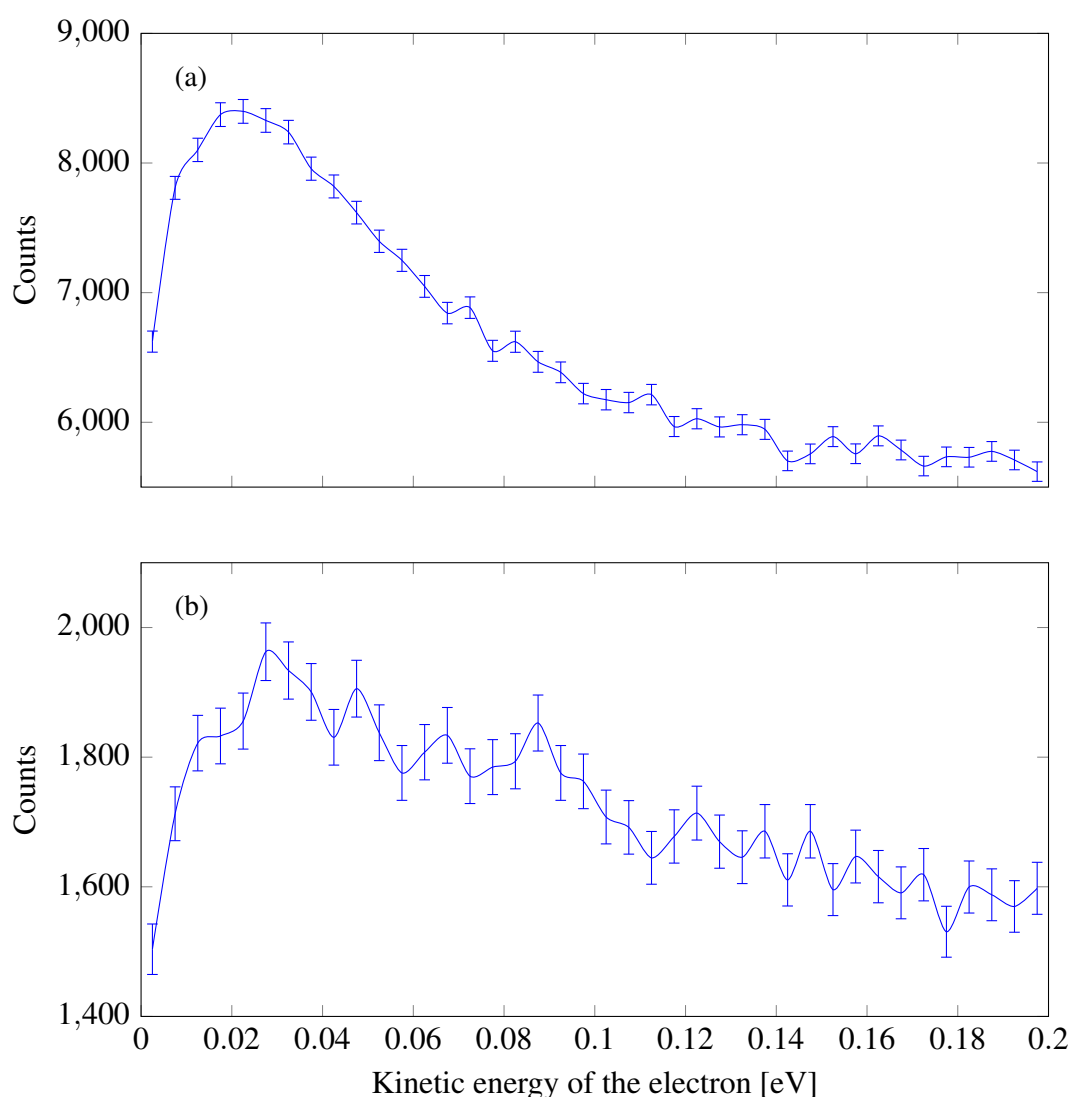
Figure 7.21: Low-energy photoelectron yields in coincidence with CH_4^+ (a) and CH_3^+ (b) cations for comparison with figure 7.20.

0.03, 0.045, 0.07 and 0.09 eV have a physical origin. Beyond 100 meV, it is difficult to find common structures between the two measurements because of the apparently different rippling frequencies. Despite these discrepancies, the overall shape of the peaks in figure 7.20 is reproduced by their respective counterparts in figure 7.21. For both ion peaks, the maximum count rate is reached at around 0.02 to 0.03 eV and the direct comparison of the scaled low-energy spectra shows that they are significantly different up to an energy of ∼200 meV (see figure 7.22). Beyond that value, the signal seems to belong to a continuous ion-unspecific background.
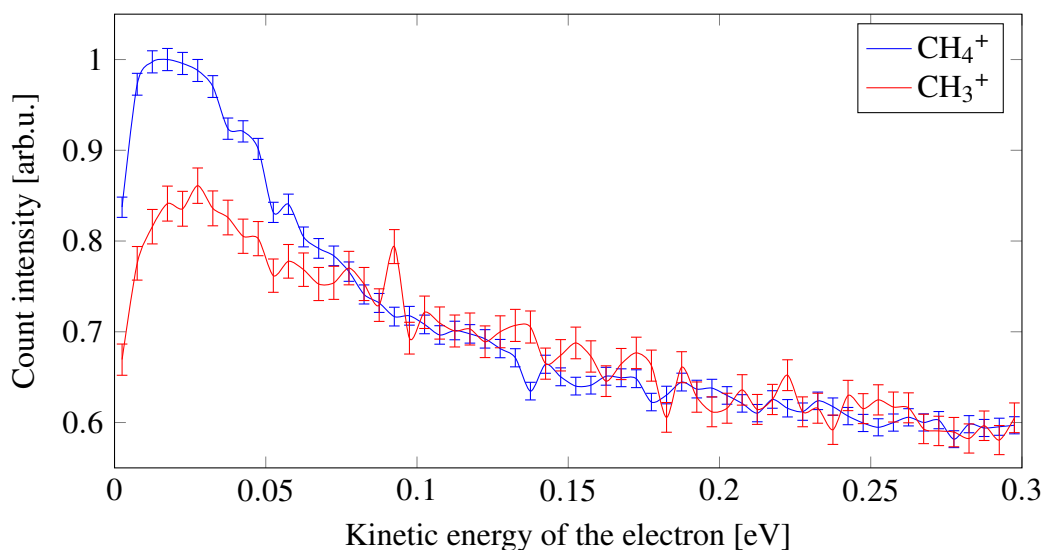
Figure 7.22: Comparison of the CH_4^+ (blue) and CH_3^+ (red) photoelectrons below 0.3 eV. In the energy region above 200 meV, the electron spectra follow the same trend. The value of 0.2 eV can be considered as an upper limit for the appearance of ion-specific low-energy electrons.

7.5.2 Rydberg series of methane

The estimated kinetic energy limit of 0.2 eV is in the order of the spacing between vibrational energy levels of the CH_4^+ and CH_3^+ cations found in previous experiments and calculations [97, 153–156]. The maximum kinetic energy of the slow electrons hence equals the energy difference of a vibrational transition with $\Delta v = 1$, which is a very interesting result. It is the expected energy range of electrons from autoionization that obey the propensity rule (equation 7.1). This is a strong argument for the hypothesis of an ionization mechanism via autoionization with simultaneous vibrational deexcitation from an intermediate Rydberg state of the molecule. A clear proof of the theory could be given if the involved intermediate states could be identified. There are three Rydberg series for the removal of a $1t_2$ electron converging to distinct states of the CH_4^+ cation, which have different ionization potentials (I_P) and molecular symmetries. According to the calculations by Velasco *et al.* [103], the energetically lowest series converges to a state in D_{2d} geometry with a vertical I_P of 13.8 eV. Vertical means that this ionization potential also includes the necessary energy to reach the vibrational excitation due to Jahn-Teller distortion. The two higher series converge to states in C_{3v} and C_{2v} symmetries, with ionization potentials of 14.4 and 15.0 eV, respectively. The possible ion geometries are not just representing different energy levels, each geometry also favors a certain fragmentation channel [103]: Since the D_{2d} geometry has the lowest energy, it is the stable ground state configuration of the cation. In the C_{3v} configuration, the bond length to one H atom is stretched while the other three C–H bonds are contracted [102] (cf. figure 5.2), which can lead to dissociation into CH_3^+ and H. In the C_{2v} symmetry, the angle between one pair of H atoms is reduced and their distance to the carbon atom is increased [102]. In this arrangement
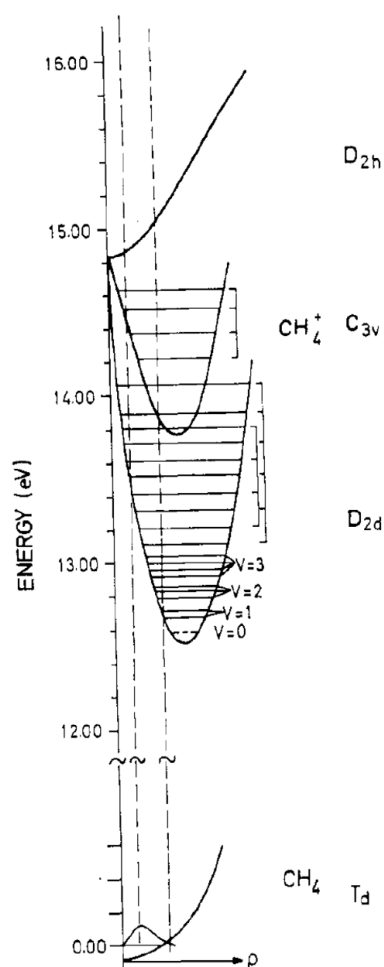
Figure 7.23: Vibrational energy levels of the methane cation for different geometries measured by Rabalais *et al.* [97]. The ground state of CH_4^+ has D_{2d} symmetry, the symmetry of the energetically higher state is C_{3v}.

a neutral hydrogen molecule can split off leaving behind a CH_2^+ ion. For the identification of intermediate Rydberg states, this implies that the energy spectra of CH_4^+ ions should mainly contain traces of the D_{2d}-symmetric Rydberg series, while the Rydberg series with C_{3v} symmetry contributes to the CH_3^+ electrons. Although there is a large pool of experimental and theoretical data about vibrational states of methane and its fragment ions [97, 157, 158] there is very few literature about Rydberg states. There are some reports on the $(2a_1)^{-1}$ Rydberg series, which converges to the excited A ion state, or on other so-called super-excited states with excitation energies up to 35 eV [105–107, 159–161]. Song *et al.* [162] observed neutral dissociation from $(1t_2)^{-1}$ Rydberg states in an intense laser field. In ref. [103], the energy levels of the three $(1t_2)^{-1}$ Rydberg series with the principal quantum number $n \leq 6$ were calculated. The theoretical Rydberg energies and the experimental data on CH_4^+ vibrational levels from refs. [103] and [97] were used to analyze the low-energy electron spectra. In the postulated mechanism of vibrational autoionization of a Rydberg state, the electron gets a well defined amount of release energy. In first approximation, the energies of the vibrational levels of a (highly excited) Ryd-

berg state and of the respective levels of the ion to which the Rydberg series converges, are identical. Under this assumption, the autoionization mechanism is displayed in figure 7.24. The electron energy after autoionization is given by
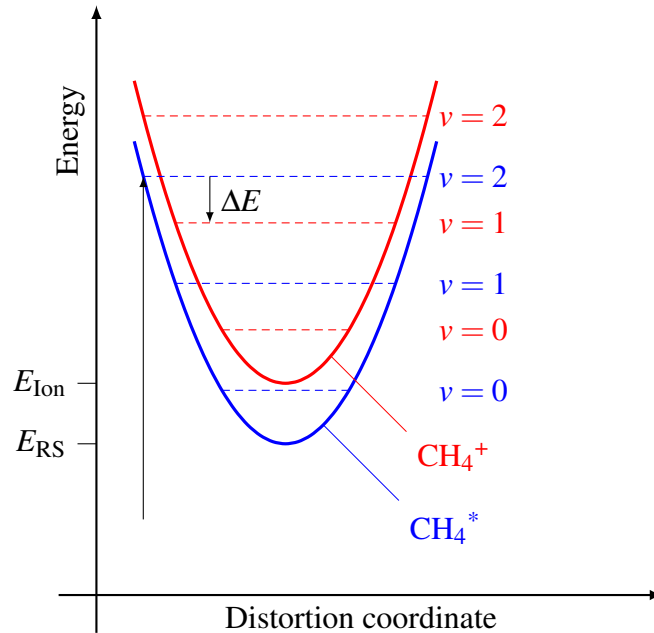
Figure 7.24: Symbolic representation of the mechanism of vibrational autoionization under the assumption that the vibrational structures of the Rydberg and ion states are the same. The methane molecule is excited to a Rydberg state (blue) by the intense laser field (long black arrow). As the tetrahedral symmetry of the molecular ground state is a strong deviation from the equilibrium position of the Jahn-Teller-distorted ion core, the Rydberg state is immediately in a vibrationally excited state v (here: $v = 2$). If the total energy of the state lies above the ion system (red potential curve) in the vibrational state $v - 1$, autoionization according to the propensity rule (equation 7.1) is possible (short arrow). The energy of the released electron is given by equation 7.4. See also refs. [1, 97]

$$\Delta E \approx E_{\text{RS}} + E_v - (E_{\text{Ion}} + E_{v-1}), \tag{7.3}$$

where E_{RS} and E_{Ion} denote the ground state energies of the Rydberg and ion states, respectively. E_v and E_{v-1} denote the vibrational excitation of the Rydberg state and of the ionic state.

$$\Delta E = E_{\text{RS}} - E_{\text{Ion}} + \Delta E_{\text{Vib}}, \tag{7.4}$$

$\Delta E_{\text{Vib}} = E_v - E_{v-1}$ is the energy difference between the two involved vibrational levels. Also under the assumption that the Rydberg states and its corresponding ionic state have

identical vibrational levels, ΔE_{Vib} is generally not a constant, but depends on v because of the anharmonic vibrational potential. If E_{Ion}, ΔE, and ΔE_{Vib} are known, it is possible to calculate the energy of the Rydberg state by solving equation 7.4.

$$E_{\text{RS}} = E_{\text{Ion}} + \Delta E - \Delta E_{\text{Vib}}. \qquad (7.5)$$

E_{Ion} is the ionization potential, which is well known experimentally and theoretically, ΔE is given by the experimentally measured photoelectron energies in this thesis and ΔE_{Vib} can be found in literature as well [97]. In order to compare results from equation 7.5 to the theoretical Rydberg energies from ref. [103], which also include the instantaneous vibrational excitation, the ionization potential for vertical transitions has to be used.

7.5.3   The D_{2d}-symmetric Rydberg series

For the D_{2d}-symmetric state of the ion, the I_{P} for vertical transitions lies between 13.6 and 13.8 eV [103, 163]. The use of 13.813 eV is appropriate because the theoretical Rydberg states in ref. [103] converge to an ion with that ionization potential. Rabalais $et\ al.$ [97] detected the vibrational states of the methane ion in an energy range from 12.6 to 14.7 eV. In the energy region of vertical ionization, between 13 and 14.1 eV, the spacing between adjacent vibrational levels was found to be nearly independent of the level of vibrational excitation and so, $\Delta E_{\text{Vib}} = 0.2$ eV can be treated as constant in further considerations. By inserting this value and $E_{\text{Ion}} = 13.81$ eV into equation 7.5 we obtain for electron energies ΔE between 0 and 200 meV

$$13.61\,\text{eV} \leq E_{\text{RS}} \leq 13.81\,\text{eV}. \qquad (7.6)$$

Ref. [103] provides no data in this energy range for the D_{2d} Rydberg series. The highest calculated state is a $6p_z b_2$ state with 13.33 eV. Even if an I_{P} of 13.6 eV was chosen, the energy of the Rydberg state would have to be higher than 13.4 eV. Nonetheless, it is possible to estimate the energy of the higher Rydberg series by guessing a reasonable quantum defect and using the Rydberg formula [105]

$$E_{\text{RS}} = I_{\text{P}} - \frac{R}{(n-\delta)^2}. \qquad (7.7)$$

R is the Rydberg energy of 13.606 eV, n is the principal quantum number and δ the quantum defect. Compared to the quantum defects given in table V of reference [103], a quantum defect of $\delta = 1.2 \pm 0.2$ seems to be an adequate guess for higher s-type ($l = 0$) Rydberg states. The uncertainty of the quantum defect is chosen arbitrarily but also in accordance to the fluctuations of the theoretical values provided by [103]. The energies calculated for Rydberg states up to $n = 15$ with this quantum defect are listed in table

n	δ	$E_{\min}$ [eV]	E_{RS} [eV]	$E_{\max}$ [eV]
3	1.11		10.02	
4	1.10		12.20	
5	1.12		12.91	
6	1.17		13.23	
7	1.2±0.2	13.379	13.409	13.435
8	1.2±0.2	13.501	13.519	13.535
9	1.2±0.2	13.577	13.589	13.600
10	1.2±0.2	13.629	13.637	13.645
11	1.2±0.2	13.665	13.671	13.677
12	1.2±0.2	13.692	13.696	13.701
13	1.2±0.2	13.712	13.715	13.719
14	1.2±0.2	13.727	13.730	13.733
15	1.2±0.2	13.739	13.742	13.744

Table 7.2: Calculated quantum defects and energies E_{RS} for s-type ($l = 0$) states in the D_{2d}-symmetric Rydberg series of methane up to $n = 15$. The values below $n = 7$ were computed in reference [103]. The higher states were calculated applying formula 7.7 with the I_P of 13.813 eV from the same reference, and an estimated quantum defect of $\delta = 1.2 \pm 0.2$. $E_{\min}$ and $E_{\max}$ are the upper and lower energy limits within the uncertainty of the guessed δ.

7.2. The energies of excited states with p ($l = 1$) and d ($l = 2$) character have also been estimated based on the data in ref. [103] (see tables 7.3 and 7.4), assuming a smaller quantum defect for these states with higher angular momentum. For completeness, the Rydberg series in the range between $n = 10$ and $n = 20$ were calculated by completely neglecting the quantum defect ($\delta = 0$, table 7.5). This is especially justified for the p and d series, where the results of the Rydberg energies for $n = 15$ with (tables 7.3 and 7.4) and without quantum defect (table 7.5) are nearly identical. Table 7.5 can also be used to deduce approximate energies of the higher s-type Rydberg levels: The value of the level with principal quantum number n is to be found in the row for $n - 1$ because according to reference [103], the quantum defect of the s-type Rydberg levels is $\delta \approx 1$. Inserting the energy values of every single state into equation 7.4, with $\Delta E_{Vib} = 0.2$ eV and $E_{Ion} = 13.81$ eV, yields the kinetic energy of an electron released by vibrational autoionization of the respective Rydberg state. Table 7.6 contains the obtained release energy results of the relevant states. In figure 7.25, the low-energy peak is plotted again, and the calculated release energies from table 7.6 are marked with indication of the corresponding Rydberg state. In the energy region below 100 meV, the positions of the Rydberg contributions fit quite well to the position of the main peak and the humps on its falling edge. Bearing in mind that the quantum defects had only been estimated with some uncertainty, whose effect on the release energy is also listed in table 7.6, the found Rydberg states starting from $n = 9$ can well be used to explain the formation of the low-energy peak. At least for the D_{2d}-Rydberg series, this result can be seen as a confirmation of the proposed autoionization mechanism.

n	δ	$E_{\min}$ [eV]	E_{RS} [eV]	$E_{\max}$ [eV]
7	0.8±0.2	13.435	13.459	13.481
8	0.8±0.2	13.535	13.551	13.565
9	0.8±0.2	13.600	13.611	13.620
10	0.8±0.2	13.645	13.652	13.659
11	0.8±0.2	13.677	13.682	13.687
12	0.8±0.2	13.701	13.705	13.708
13	0.8±0.2	13.719	13.722	13.725
14	0.8±0.2	13.733	13.735	13.737
15	0.8±0.2	13.744	13.746	13.747

Table 7.3: Estimated energy values for p-type Rydberg levels ($l = 1$) of methane converging to $I_{\text{P}} = 13.813$ eV. The quantum defect of $\delta = 0.8 \pm 0.2$ was guessed based on data for levels with $n < 7$ in reference [103].

n	δ	$E_{\min}$ [eV]	E_{RS} [eV]	$E_{\max}$ [eV]
6	0.45±0.25	13.329	13.371	13.409
7	0.45±0.25	13.470	13.496	13.519
8	0.45±0.25	13.558	13.574	13.589
9	0.45±0.25	13.616	13.627	13.637
10	0.45±0.25	13.656	13.664	13.671
11	0.45±0.25	13.685	13.691	13.696
12	0.45±0.25	13.706	13.711	13.715
13	0.45±0.25	13.723	13.727	13.730
14	0.45±0.25	13.736	13.739	13.742
15	0.45±0.25	13.747	13.749	13.751

Table 7.4: Estimated energy values for d-type Rydberg levels ($l = 2$) of methane converging to $I_{\text{P}} = 13.813$ eV. As for the Rydberg states with lower angular momentum, the quantum defect of $\delta = 0.45 \pm 0.25$ was guessed based on reference [103].

n	E_{R} [eV]
10	13.677
11	13.701
12	13.719
13	13.733
14	13.744
15	13.753
16	13.760
17	13.766
18	13.771
19	13.775
20	13.779

Table 7.5: Energies of higher Rydberg states converging to 13.813 eV with $\delta = 0$.

n	angular momentum	ΔE_{min} [eV]	ΔE [eV]	ΔE_{max} [eV]
9	p	-0.013	-0.002	0.007
9	d	0.003	0.014	0.024
10	s	0.016	0.024	0.032
10	p	0.032	0.039	0.046
10	d	0.043	0.051	0.058
11	s	0.052	0.058	0.064
11	p	0.064	0.069	0.074
11	d	0.072	0.078	0.083
12	s	0.079	0.083	0.088
12	p	0.088	0.092	0.095
12	d	0.093	0.098	0.102
13	s	0.099	0.102	0.106
13	p	0.106	0.109	0.112
13	d	0.11	0.114	0.117
14	s	0.114	0.117	0.12
14	p	0.12	0.122	0.124
14	d	0.123	0.126	0.129
15	s	0.126	0.129	0.131
15	p	0.131	0.133	0.134
15	d	0.134	0.136	0.138
16	spd		0.147	
17	spd		0.153	
18	spd		0.158	
19	spd		0.162	
20	spd		0.166	

Table 7.6: Electron release energies for vibrational autoionization of a D_2d-Rydberg state of methane characterized by the principal quantum number n and the angular momentum quantum number l, represented by s ($l = 0$), p ($l = 1$), and d ($l = 2$). ΔE_{min} and ΔE_{max} represent the lower and upper limits of the release energies due to the uncertainty of the quantum defect estimation. For $n \geq 16$, the Rydberg energies from table 7.5 without quantum defect were used.
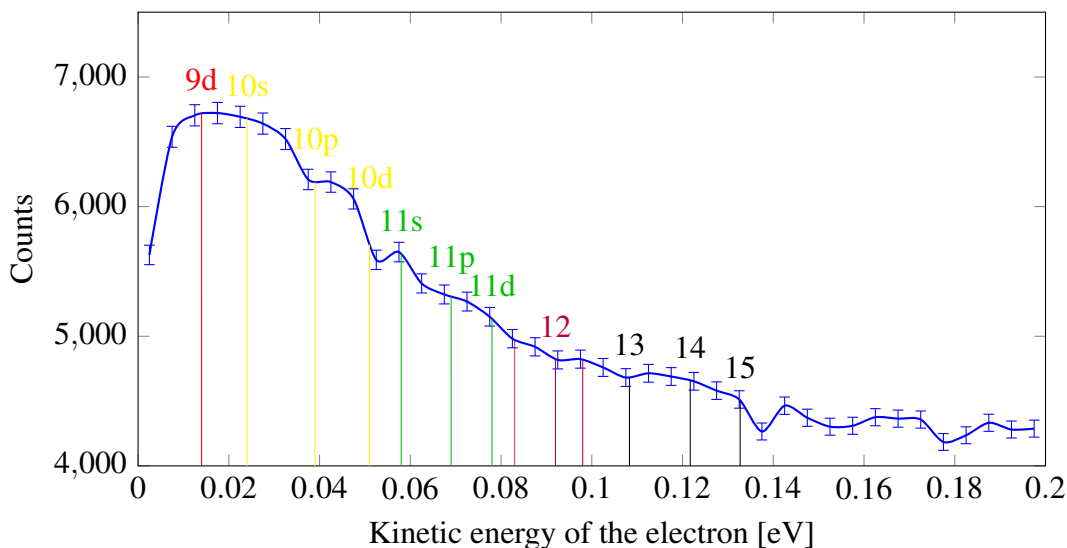
Figure 7.25: Low-energy photoelectron peak with contributions of the estimated Rydberg states converging to 13.813 eV. The series are represented in different colors ($n = 9$: red, $n = 10$: yellow, $n = 11$: green, $n = 12$: purple, $n \geq 13$: black). The features of the peak below 100 meV fit well to the position of the marked Rydberg states. The uncertainty of the release energies due to the estimation of the quantum defect depends on n. Within the range of uncertainties given in table 7.6, the peak structure can be explained by Rydberg states between $n = 9$ and $n = 12$.

7.5.4 The C_{3v}-symmetric Rydberg series

After succesfully relating the CH_4^+ electron energies to Rydberg states of the series with D_{2d}-symmetry, the low-energy peak in coincidence with CH_3^+ is analyzed in the same manner. As the CH_3^+ ion is supposed to be a daughter product of the CH_4^+ ion in C_{3v}-configuration [103], the Rydberg series with this symmetry is considered.

The energy range in which the Rydberg states in question are suspected is obtained by applying again equation 7.5. The parameters used for this series are $I_P = 14.42$ eV and $\Delta E_{Vib} = \sim 0.15$ eV, according to the findings in ref. [97] about the vibrational states at higher energies. This is again the upper limit for the energy of electrons that are released according to the proposed mechanism because the vibrational quantum number may only change by $\Delta v = 1$. The expected Rydberg series have to lie within the following boundaries:

$$14.27 \, \text{eV} \leq E_{RS} \leq 14.42 \, \text{eV}. \tag{7.8}$$

The provided Rydberg energies in refs. [103] and [164] are all below 14 eV. It is again possible to guess the energies of higher states with the Rydberg formula. This time, a quantum defect of $\delta = 1.3 \pm 0.2$ was chosen for the higher s-states, while $\delta = 0.75 \pm 0.25$

and $\delta = 0.4 \pm 0.4$ were assumed for the p- and d-states. The resulting Rydberg levels are found in tables 7.7, 7.8 and 7.9. For higher states above $n = 15$, the energy levels were again calculated neglecting the quantum defect (see table 7.10).

n	δ	E_{min} [eV]	E_{RS} [eV]	E_{max} [eV]
3	1.12		10.57	
4	1.11		12.79	
5	1.16		13.50	
6	1.24		13.82	
7	1.3±0.2	13.971	14.002	14.030
8	1.3±0.2	14.099	14.118	14.135
9	1.3±0.2	14.179	14.192	14.203
10	1.3±0.2	14.233	14.241	14.249
11	1.3±0.2	14.270	14.276	14.282
12	1.3±0.2	14.298	14.302	14.307
13	1.3±0.2	14.318	14.322	14.325
14	1.3±0.2	14.334	14.337	14.339
15	1.3±0.2	14.346	14.349	14.351

Table 7.7: Calculated quantum defects and energies for s-type states in the C_{3v}-symmetric Rydberg series of methane up to $n = 15$. The results up to $n = 6$ can again be found in [103], the higher Rydberg levels were calculated with an I_P of 14.421 eV [103] and $\delta = 1.3 \pm 0.2$.

n	δ	E_{min} [eV]	E_{RS} [eV]	E_{max} [eV]
7	0.75±0.25	14.043	14.073	14.099
8	0.75±0.25	14.143	14.162	14.179
9	0.75±0.25	14.208	14.221	14.233
10	0.75±0.25	14.253	14.262	14.270
11	0.75±0.25	14.285	14.292	14.298
12	0.75±0.25	14.309	14.314	14.318
13	0.75±0.25	14.327	14.330	14.334
14	0.75±0.25	14.341	14.344	14.346
15	0.75±0.25	14.352	14.350	14.356

Table 7.8: Energy levels of p-type ($l = 1$) excited states of the C_{3v}-symmetric Rydberg converging to 14.421 eV [103] with estimated $\delta = 0.75 \pm 0.25$.

The next step is again applying equation 7.4 to calculate the kinetic energies of electrons released by autoionization of the estimated excited states. The results are listed in table 7.11. The obtained release energies were also included into the electron distribution of coincident CH_3^+ ions to find out which Rydberg states contribute to the low-energy peak. In difference to the photoelectrons measured in coincidence with CH_4^+ ions, where the main characteristics of the low-energy peak were in agreement with the energy levels of certain states of the Rydberg series with D_{2d} symmetry, this is only partially the case for

n	δ	$E_{\min}$ [eV]	E_{RS} [eV]	$E_{\max}$ [eV]
6	0.4±0.4	13.918	13.987	14.043
7	0.4±0.4	14.067	14.109	14.143
8	0.4±0.4	14.159	14.185	14.208
9	0.4±0.4	14.219	14.237	14.253
10	0.4±0.4	14.260	14.273	14.285
11	0.4±0.4	14.290	14.300	14.309
12	0.4±0.4	14.313	14.320	14.327
13	0.4±0.4	14.330	14.335	14.341
14	0.4±0.4	14.343	14.347	14.352
15	0.4±0.4	14.354	14.357	14.361

Table 7.9: Energy levels of d-type ($l = 2$) excited states of the C_{3v}-symmetric Rydberg converging to 14.421 eV [103] with estimated $\delta = 0.4 \pm 0.4$.

n	E_R [eV]
10	14.285
11	14.309
12	14.327
13	14.341
14	14.352
15	14.361
16	14.368
17	14.374
18	14.379
19	14.383
20	14.387

Table 7.10: Higher Rydberg energy levels of the C_{3v}-symmetric Rydberg series of the methane molecule converging to 14.421 eV without quantum defect ($\delta = 0$).

the CH_3^+ photoelectrons and the C_{3v}-symmetric Rydberg series. As the lowest possible Rydberg state has already a principal quantum number of $n = 11$, the spacing between neighboring states is significantly smaller as was the case for the CH_4^+ photoelectrons and the states are more densely concentrated within the energy range of the peak. This could actually be one explanation for the stronger rippling, but it is hard to decide if the calculated Rydberg states are really the origin of the rippling structure. It could also be caused by contributions from autoionizing Rydberg states with a different symmetry even though the formation of a CH_3^+ ion is favored by the intermediate state in C_{3v} symmetry. In addition, the spectrum contains a certain amount of wrong coincidences because the data filtering was only possible by defining a time-of-flight condition.

n	angular momentum	$\Delta E_{\min}$ [eV]	ΔE [eV]	$\Delta E_{\max}$ [eV]
10	d	-0.011	0.002	0.014
11	s	-0.001	0.005	0.011
11	p	0.014	0.021	0.027
11	d	0.019	0.029	0.038
12	s	0.027	0.031	0.036
12	p	0.038	0.043	0.047
12	d	0.042	0.049	0.056
13	s	0.047	0.051	0.054
13	p	0.056	0.059	0.063
13	d	0.059	0.064	0.07
14	s	0.063	0.066	0.068
14	p	0.07	0.073	0.075
14	d	0.072	0.076	0.081
15	s	0.075	0.078	0.08
15	p	0.081	0.079	0.085
15	d	0.083	0.086	0.09
16	spd		0.097	
17	spd		0.103	
18	spd		0.108	
19	spd		0.112	
20	spd		0.116	

Table 7.11: Electron release energies for vibrational autoionization of the methane Rydberg series with C_{3v} symmetry. The release energies for $n \geq 16$ are based on the Rydberg levels with $\delta = 0$.
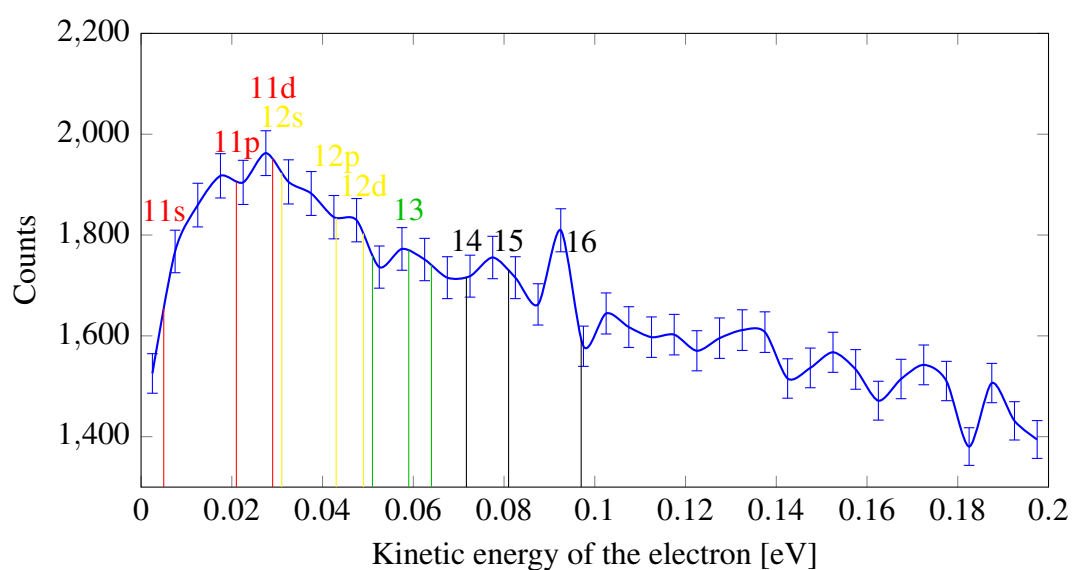
Figure 7.26: Low-energy electron peak measured in coincidence with CH_3^+. The vertical lines correspond to the expected electron release energies for vibrational autoionization of the respective Rydberg state. The colors correspond to the following principal quantum numbers: $n = 11$: red, $n = 12$: yellow, $n = 13$: green, $n \geq 14$: black.

Chapter 8

Conclusion and Outlook

The work in this thesis deals with several variations of (ultrafast) light-matter interaction. In the main experiment, the photoionization of various gas targets was investigated using a 25 fs two-color pulse. The generation of such a pulse includes itself another important phenomenon, namely second-harmonic generation (SHG) in a nonlinear crystal. And finally, a beamline to generate higher harmonics was built to use it as a light source for experiments with solids.

The two-color photoionization experiments in methane and other targets revealed differences in the electron spectra, depending on the ionization and fragmentation channel, in contradiction to the established two-step model of molecular photoionization and dissociation [37]. A significant increase of slow electrons with kinetic energies below 200 meV was observed for events with a coincident molecular ion, i.e. CH_4^+ or CH_3^+. An enhancement of low-energy electrons was neither observed in methane together with a coincident proton, nor in a comparison measurement with atomic argon. This finding is a strong hint that the slow electrons are released in a different mechanism related to the molecular nature of the ion. The same phenomenon was also found in the much simpler system of molecular hydrogen, and could be explained by autoionization via vibrational relaxation of intermediate Rydberg states [1]. Analyzing the dependence of the electron spectra on the two-color phase did not show a difference between the ionization channels, but a shift of the asymmetry phase offset was found at electron energies below 500 meV. This phase shift suggests the electron release from an intermediate state with a lifetime shorter than the pulse duration, while electrons above 500 meV are emitted directly. The absence of a clear low-energy peak at higher laser intensity could imply that in this regime, the two-step model is valid. The evaluation of the methane data and comparison to former experiments [97] indicated that the width of the low-energy peak was in the order of the vibrational level spacing of the methane cation, the expected upper limit for most electrons released in the postulated autoionization mechanism. The final identification of specific Rydberg states was partially successful even without any available reference data. By guessing the quantum defects for higher Rydberg states, their energies could be estimated and an electron release energy could be calculated for each of these states. The calculated release energies matched fairly well the characteristic features of the low-energy peak of

electrons in coincidence with CH_4^+ ions. The analysis of the CH_3^+ low-energy electron spectrum did not provide the same agreement with calculated Rydberg energies. Because of the strong rippling, a clear assignment of a Rydberg state to a certain feature of the peak was impossible. It was found that the minimum principal quantum number for a Rydberg state to contribute to the low-energy peak of CH_3^+ has to be at least $n = 11$. The small spacing between the Rydberg states in question could explain the rippling on the spectrum. Even though by guessing of quantum defects and Rydberg energies it was possible to identify some of the Rydberg states, there is need for more reference data, and theoreticians are asked to systematically calculate the energy levels of higher Rydberg states of methane. In comparison to the results with H_2, additional autoionization pathways are possible in methane, for example via relaxation from a Rydberg state of the energetically higher C_{3v} series to the ionic D_{2d} state, which could cause the release of electrons with energies in the order of the energy gap between the two ion configurations of $\sim 0.6\,eV$. This energy difference could explain the detection of electrons with nearly zero longitudinal momentum and a transverse momentum below $0.2\,a.u.$ that were detected at higher intensities in coincidence with CH_4^+ and CH_3^+ (cf. figure 7.14).

As a possible future experiment, the evolution of the Jahn-Teller deformation of the methane molecule could be investigated using Coulomb explosion imaging [165] in a pump-probe scheme. In such a proposed experiment, the molecule is ionized by an IR or two-color pulse as in the work of this thesis and releases a (slow) electron. After a variable time delay, the system is probed by a very intense second pulse, possibly a free-electron laser pulse with high photon energy, or an XUV pulse from the high-harmonics beamline. If the probe pulse is able to ionize and detach each of the hydrogen atoms from the intermediate CH_4^+ ion, the complex will Coulomb explode. The momentum of each charged fragment would allow to determine the geometry of the intermediate ion at the arrival of the probe pulse. The variation of the pump-probe delay could show how the molecular ion is distorted by the Jahn-Teller effect in time. In addition it could be investigated if certain slow electrons only appear when the molecule is excited to a certain state of symmetry. Another appealing future project could be the investigation of other highly excited states of the molecule via attosecond transient absorption spectroscopy [137, 138] and to compare the results to experiments with neon [166], which has the same number of electrons as methane.

It would also be interesting to investigate the intensity dependence of the enhanced low-energy electron signal. In the present work, only two intensity regimes were studied, and the low-energy spectra of both regimes were very different from each other. In a systematic study, the yield of low-energy electrons could be measured as a function of the laser intensity. Theoretical calculations taking into account the additional degrees of freedom of the methane molecule and the possible couplings between electronically and vibrationally excited states near the ionization threshold would be very helpful to understand the release of low-energy photoelectrons. In order to prove that the proposed autoionization mechanism is not specific to hydrogen and methane, the experiments have to be repeated with other gases. Due to the difficulty of determining the high-n Rydberg states of methane, it is probably a good approach to look for low-energy photoelectrons in the spectra of well-studied diatomic molecules like O_2, N_2 or CO. In order to investigate the

influence of additional degrees of freedom of larger molecules, the measurements should also be performed with molecules of that type, such as NH_3, C_2H_4 or C_2H_6. Alternatively, the results of the methane experiment could be compared to CF_4, a molecule with the same geometry but different vibrational levels due to the heavier fluorine atoms. Proceeding to yet larger molecules is of course desirable but the data acquisition, analysis and theoretical description will be more and more challenging due to the increasing number of possible ionization and dissociation channels.

Appendix A

Atomic Units

The system of atomic units is frequently used in the field of atomic and molecular physics. It is related to the physical properties of the hydrogen atom. The system uses the convention of $m_e = e = \hbar = a_0 = \frac{1}{4\pi\varepsilon_0} = 1$. In the following table, the basic physical quantities, their atomic units and the respective values in SI units are given.

Quantity	Unit	Value
Mass	Electron mass m_e	9.109×10^{-31} kg
Charge	Elementary charge e	1.602×10^{-19} C
Angular momentum	Reduced Planck constant $\hbar$	1.055×10^{-34} J s
Length	First Bohr radius a_0	5.292×10^{-11} m
Velocity	$v_0 = \alpha c_0$	$2.188 \times 10^6 \, \mathrm{m\,s^{-1}}$
Momentum	$p_0 = m_e v_0$	$1.993 \times 10^{-24} \, \mathrm{kg\,m\,s^{-1}}$
Time	$\frac{a_0}{v_0}$	2.419×10^{-17} s
Energy	$E_h = \frac{e^2}{4\pi\varepsilon_0 a_0} = \alpha^2 m_e c_0^2$	4.360×10^{-18} J=27.2114 eV
Electric potential	$E_h/e = \frac{e}{4\pi\varepsilon_0 a_0}$	27.2114 V
Electric field	$E_0 = \frac{e}{4\pi\varepsilon_0 a_0^2}$	$5.142 \times 10^{11} \, \mathrm{V\,m^{-1}}$
(Laser) Intensity	$I_0 = \frac{1}{2}\varepsilon_0 c_0 E_0^2$	$3.509 \times 10^{16} \, \mathrm{W\,cm^{-2}}$

Table A.1: Relationship between physical quantities in the system of atomic units and the SI.

More information about the system of atomic units can be found in [167].

Bibliography

[1] Y. Mi, N. Camus, L. Fechner, M. Laux, R. Moshammer, and T. Pfeifer.
Electron-Nuclear Coupling through Autoionizing States after Strong-Field Excitation of H_2 Molecules.
Phys. Rev. Lett. **118**, 183201 (May 2017).
URL https: //link.aps.org/doi/10.1103/PhysRevLett.118.183201.

[2] C. Ott, A. Kaldun, L. Argenti, P. Raith, K. Meyer, M. Laux, Y. Zhang, A. Blättermann, S. Hagstotz, T. Ding, R. Heck, J. Madroñero, F. Martin, and T. Pfeifer.
Reconstruction and control of a time-dependent two-electron wave packet.
Nature **516**, 374–378 (Dec 2014).
URL http://www.nature.com/nature/journal/v516/n7531/full/nature14026.html.

[3] C. Ott, A. Kaldun, P. Raith, K. Meyer, M. Laux, J. Evers, C. H. Keitel, C. H. Greene, and T. Pfeifer.
Lorentz Meets Fano in Spectral Line Shapes: A Universal Phase and Its Laser Control.
Science **340**, 716–720 (2013).
URL http://science.sciencemag.org/content/340/6133/716.

[4] A. Blättermann, C. Ott, A. Kaldun, T. Ding, V. Stooß, M. Laux, M. Rebholz, and T. Pfeifer.
In situ characterization of few-cycle laser pulses in transient absorption spectroscopy.
Opt. Lett. **40**, 3464–3467 (Aug 2015).
URL http://ol.osa.org/abstract.cfm?URI=ol-40-15-3464.

[5] A. Kaldun, C. Ott, A. Blättermann, M. Laux, K. Meyer, T. Ding, A. Fischer, and T. Pfeifer.
Extracting Phase and Amplitude Modifications of Laser-Coupled Fano Resonances.
Phys. Rev. Lett. **112**, 103001 (Mar 2014).
URL https: //link.aps.org/doi/10.1103/PhysRevLett.112.103001.

[6] P. Raith, C. Ott, K. Meyer, A. Kaldun, M. Laux, M. Ceci, C. P. Anderson, and T. Pfeifer.

Carrier-envelope phase- and spectral control of fractional high-harmonic combs.
Journal of Applied Physics **114**, 173102 (2013).
URL http://dx.doi.org/10.1063/1.4827194.

[7] C. Ott, M. Schönwald, P. Raith, A. Kaldun, G. Sansone, M. Krüger,
P. Hommelhoff, Y. Patil, Y. Zhang, K. Meyer, M. Laux, and T. Pfeifer.
Strong-field spectral interferometry using the carrier-envelope phase.
New J. Phys. **15**, 073031 (2013).
URL http://stacks.iop.org/1367-2630/15/i=7/a=073031.

[8] P. Raith, C. Ott, C. P. Anderson, A. Kaldun, K. Meyer, M. Laux, Y. Zhang, and
T. Pfeifer.
*Fractional high-order harmonic combs and energy tuning by attosecond-precision
split-spectrum pulse control.*
Applied Physics Letters **100**, 121104 (2012).
URL http://dx.doi.org/10.1063/1.3693615.

[9] R. Berera, R. van Grondelle, and J. T. M. Kennis.
*Ultrafast transient absorption spectroscopy: principles and application to
photosynthetic systems.*
Photosynthesis Research **101**, 105–118 (2009).
URL http://dx.doi.org/10.1007/s11120-009-9454-y.

[10] C. J. Garvey and R. Hanlon.
Computed tomography in clinical practice.
BMJ **324**, 1077–1080 (2002).
URL http://www.bmj.com/content/324/7345/1077.

[11] J. Thariat, J.-M. Hannoun-Levi, A. S. Myint, T. Vuong, and J.-P. Gerard.
Past, present, and future of radiotherapy for the benefit of patients.
Nature Reviews Clinical Oncology **10**, 52–60 (Jan 2013).
URL http://www.nature.com/nrclinonc/journal/v10/n1/
full/nrclinonc.2012.203.html.

[12] C. S. Cockell.
Ultraviolet radiation, evolution and the π-electron system.
Biological Journal of the Linnean Society **63**, 449 – 457 (1998).
URL http://www.sciencedirect.com/science/article/pii/
S0024406697902017.

[13] T. H. Maiman.
Stimulated Optical Radiation in Ruby.
Nature **187**, 493–494 (1960).
URL http://www.nature.com/nature/journal/v187/n4736/
abs/187493a0.html.

[14] E. Goulielmakis, M. Schultze, M. Hofstetter, V. S. Yakovlev, J. Gagnon,
M. Uiberacker, A. L. Aquila, E. M. Gullikson, D. T. Attwood, R. Kienberger,
F. Krausz, and U. Kleineberg.
Single-Cycle Nonlinear Optics.
Science **320**, 1614–1617 (2008).

URL
`http://science.sciencemag.org/content/320/5883/1614.`

[15] M. Lewenstein, P. Balcou, M. Y. Ivanov, A. L'Huillier, and P. B. Corkum.
Theory of high-harmonic generation by low-frequency laser fields.
Phys. Rev. A **49**, 2117–2132 (Mar 1994).
URL `https://link.aps.org/doi/10.1103/PhysRevA.49.2117.`

[16] T. Brabec and F. Krausz.
Intense few-cycle laser fields: Frontiers of nonlinear optics.
Rev. Mod. Phys. **72**, 545–591 (Apr 2000).
URL `https://link.aps.org/doi/10.1103/RevModPhys.72.545.`

[17] F. Krausz and M. Ivanov.
Attosecond physics.
Rev. Mod. Phys. **81**, 163–234 (Feb 2009).
URL `https://link.aps.org/doi/10.1103/RevModPhys.81.163.`

[18] K. Zhao, Q. Zhang, M. Chini, Y. Wu, X. Wang, and Z. Chang.
Tailoring a 67 attosecond pulse through advantageous phase-mismatch.
Opt. Lett. **37**, 3891–3893 (Sep 2012).
URL `http://ol.osa.org/abstract.cfm?URI=ol-37-18-3891.`

[19] A. H. Zewail.
Laser Femtochemistry.
Science **242**, 1645–1653 (1988).
URL
`http://science.sciencemag.org/content/242/4886/1645.`

[20] W. Li, A. A. Jaroń-Becker, C. W. Hogle, V. Sharma, X. Zhou, A. Becker, H. C. Kapteyn, and M. M. Murnane.
Visualizing electron rearrangement in space and time during the transition from a molecule to atoms.
Proceedings of the National Academy of Sciences **107**, 20219–20222 (2010).
URL `http://www.pnas.org/content/107/47/20219.abstract.`

[21] A. H. Zewail.
Femtochemistry: Atomic-Scale Dynamics of the Chemical Bond.
The Journal of Physical Chemistry A **104**, 5660–5694 (2000).
URL `http://dx.doi.org/10.1021/jp001460h.`

[22] H. J. Wörner, J. B. Bertrand, D. V. Kartashov, P. B. Corkum, and D. M. Villeneuve.
Following a chemical reaction using high-harmonic interferometry.
Nature **466**, 604–607 (Jul 2010).
URL `http://www.nature.com/nature/journal/v466/n7306/full/nature09185.html.`

[23] P. Brumer and M. Shapiro.
Control of unimolecular reactions using coherent light.
Chemical Physics Letters **126**, 541 – 546 (1986).

URL `http://www.sciencedirect.com/science/article/pii/`
`S0009261486801713`.

[24] A. M. Weiner.
Femtosecond pulse shaping using spatial light modulators.
Review of Scientific Instruments **71**, 1929–1960 (2000).
URL `http://dx.doi.org/10.1063/1.1150614`.

[25] A. M. Weiner.
Ultrafast optical pulse shaping: A tutorial review.
Optics Communications **284**, 3669 – 3692 (2011).
URL `http://www.sciencedirect.com/science/article/pii/`
`S0030401811003750`.
Special Issue on Optical Pulse Shaping, Arbitrary Waveform Generation, and
Pulse Characterization.

[26] T. Baumert, T. Brixner, V. Seyfried, M. Strehle, and G. Gerber.
Femtosecond pulse shaping by an evolutionary algorithm with feedback.
Applied Physics B **65**, 779–782 (1997).
URL `http://dx.doi.org/10.1007/s003400050346`.

[27] G. G. Paulus, F. Grasbon, H. Walther, P. Villoresi, M. Nisoli, S. Stagira, E. Priori,
and S. D. Silvestri.
Absolute-phase phenomena in photoionization with few-cycle laser pulses.
Nature **414**, 182–184 (November 2001).
URL `http://www.nature.com/nature/journal/v414/n6860/`
`full/414182a0.html`.

[28] T. Wittmann, B. Horvath, W. Helml, M. G. Schatzel, X. Gu, A. L. Cavalieri, G. G.
Paulus, and R. Kienberger.
Single-shot carrier-envelope phase measurement of few-cycle laser pulses.
Nature Physics **5**, 357–362 (May 2009).
URL `http://www.nature.com/nphys/journal/v5/n5/full/`
`nphys1250.html`.

[29] D. J. Jones, S. A. Diddams, J. K. Ranka, A. Stentz, R. S. Windeler, J. L. Hall, and
S. T. Cundiff.
*Carrier-Envelope Phase Control of Femtosecond Mode-Locked Lasers and Direct
Optical Frequency Synthesis.*
Science **288**, 635–639 (2000).
URL `http://science.sciencemag.org/content/288/5466/635`.

[30] P. M. Kraus, A. Rupenyan, and H. J. Wörner.
*High-Harmonic Spectroscopy of Oriented OCS Molecules: Emission of Even and
Odd Harmonics.*
Phys. Rev. Lett. **109**, 233903 (Dec 2012).
URL `https:`
`//link.aps.org/doi/10.1103/PhysRevLett.109.233903`.

[31] R. Dörner, V. Mergel, O. Jagutzki, L. Spielberger, J. Ullrich, R. Moshammer, and
H. Schmidt-Böcking.

Cold Target Recoil Ion Momentum Spectroscopy: a 'momentum microscope' to view atomic collision dynamics.
Physics Reports **330**, 95 – 192 (2000).
URL http://www.sciencedirect.com/science/article/pii/S037015739900109X.

[32] J. Ullrich, R. Moshammer, A. Dorn, R. Dörner, L. P. H. Schmidt, and H. Schmidt-Böcking.
Recoil-ion and electron momentum spectroscopy: reaction-microscopes.
Reports on Progress in Physics **66**, 1463 (2003).
URL http://stacks.iop.org/0034-4885/66/i=9/a=203.

[33] M. V. Ammosov, N. B. Delone, and V. P. Krainov.
Tunnel ionization of complex atoms and of atomic ions in an alternating electromagnetic field.
Soviet Physics JETP **64**, 1191–1194 (1986).
URL http://www.jetp.ac.ru/cgi-bin/e/index/e/64/6/p1191?a=list.

[34] L. V. Keldysh.
Ionization in the field of a strong electromagnetic wave.
Soviet Physics JETP **20**, 1307 (1965).
URL http://www.jetp.ac.ru/cgi-bin/e/index/e/20/5/p1307?a=list.

[35] R. H. Reiss.
Foundations of the Strong-Field Approximation, pp. 1–31.
Springer Berlin Heidelberg, Berlin, Heidelberg (2008).
URL http://dx.doi.org/10.1007/978-3-540-73794-0_1.

[36] P. B. Corkum.
Plasma perspective on strong field multiphoton ionization.
Phys. Rev. Lett. **71**, 1994–1997 (Sep 1993).
URL http://link.aps.org/doi/10.1103/PhysRevLett.71.1994.

[37] M. F. Kling, C. Siedschlag, A. J. Verhoef, J. I. Khan, M. Schultze, T. Uphues, Y. Ni, M. Uiberacker, M. Drescher, F. Krausz, and M. J. J. Vrakking.
Control of Electron Localization in Molecular Dissociation.
Science **312**, 246–248 (2006).
URL http://science.sciencemag.org/content/312/5771/246.

[38] C. I. Blaga, F. Catoire, P. Colosimo, G. G. Paulus, H. G. Muller, P. Agostini, and L. F. DiMauro.
Strong-field photoionization revisited.
Nature Physics **5**, 335–338 (May 2009).
URL http://www.nature.com/nphys/journal/v5/n5/full/nphys1228.html.

[39] B. Zhang and Z. Zhao.
Strong-field approximation for the ionization of N_2 and CO_2.

Phys. Rev. A **82**, 035401 (Sep 2010).
URL
https://link.aps.org/doi/10.1103/PhysRevA.82.035401.

[40] L. Fechner, N. Camus, J. Ullrich, T. Pfeifer, and R. Moshammer.
Strong-Field Tunneling from a Coherent Superposition of Electronic States.
Phys. Rev. Lett. **112**, 213001 (May 2014).
URL https:
//link.aps.org/doi/10.1103/PhysRevLett.112.213001.

[41] P. Eckle, M. Smolarski, P. Schlup, J. Biegert, A. Staudte, M. Schöffler, H. G.
Muller, R. Dörner, and U. Keller.
Attosecond angular streaking.
Nature Physics **4**, 565–570 (Jul 2008).
URL http://www.nature.com/nphys/journal/v4/n7/full/
nphys982.html.

[42] B. Boudaïffa, P. Cloutier, D. Hunting, M. A. Huels, and L. Sanche.
Resonant Formation of DNA Strand Breaks by Low-Energy (3 to 20 eV) Electrons.
Science **287**, 1658–1660 (2000).
URL
http://science.sciencemag.org/content/287/5458/1658.

[43] H. A. Jahn and E. Teller.
*Stability of Polyatomic Molecules in Degenerate Electronic States. I. Orbital
Degeneracy.*
Proceedings of the Royal Society of London A: Mathematical, Physical and
Engineering Sciences **161**, 220–235 (1937).
URL http:
//rspa.royalsocietypublishing.org/content/161/905/220.

[44] A. Javan, W. R. Bennett, and D. R. Herriott.
*Population Inversion and Continuous Optical Maser Oscillation in a Gas
Discharge Containing a He-Ne Mixture.*
Phys. Rev. Lett. **6**, 106–110 (Feb 1961).
URL https://link.aps.org/doi/10.1103/PhysRevLett.6.106.

[45] R. Ell, U. Morgner, F. X. Kärtner, J. G. Fujimoto, E. P. Ippen, V. Scheuer,
G. Angelow, T. Tschudi, M. J. Lederer, A. Boiko, and B. Luther-Davies.
*Generation of 5-fs pulses and octave-spanning spectra directly from a Ti:sapphire
laser.*
Opt. Lett. **26**, 373–375 (Mar 2001).
URL http://ol.osa.org/abstract.cfm?URI=ol-26-6-373.

[46] B. Xu, Y. Coello, V. V. Lozovoy, D. A. Harris, and M. Dantus.
Pulse shaping of octave spanning femtosecond laser pulses.
Opt. Express **14**, 10939–10944 (Oct 2006).
URL http://www.opticsexpress.org/abstract.cfm?URI=
oe-14-22-10939.

[47] H. W. Mocker and R. J. Collins.

Mode competition and self-locking effects in a q-switched ruby laser.
Applied Physics Letters **7**, 270–273 (1965).
URL `http://dx.doi.org/10.1063/1.1754253`.

[48] A. J. DeMaria, C. M. Ferrar, and G. E. Danielson Jr.
Mode locking of a Nd^{3+}-doped glass laser.
Applied Physics Letters **8**, 22–24 (1966).
URL `http://dx.doi.org/10.1063/1.1754411`.

[49] J.-C. Diels and W. Rudolph.
5 - Ultrashort Sources I: Fundamentals.
In J.-C. Diels and W. Rudolph (Eds.), *Ultrashort Laser Pulse Phenomena (Second Edition)*, second edition edition, pp. 277 – 339. Academic Press, Burlington (2006).
URL `http://www.sciencedirect.com/science/article/pii/B9780122154935500069`.

[50] M. Wollenhaupt, A. Assion, and T. Baumert.
Short and Ultrashort Laser Pulses.
In F. Träger (Ed.), *Springer Handbook of Lasers and Optics*, chapter 12, pp. 1047–1094. Springer Berlin Heidelberg, Berlin, Heidelberg (2012).
URL `http://dx.doi.org/10.1007/978-3-642-19409-2_12`.

[51] P. Georges, F. Estable, F. Salin, J. P. Poizat, P. Grangier, and A. Brun.
High-efficiency multipass Ti:sapphire amplifiers for a continuous-wave single-mode laser.
Opt. Lett. **16**, 144–146 (Feb 1991).
URL `http://ol.osa.org/abstract.cfm?URI=ol-16-3-144`.

[52] U. Keller.
Ultrafast solid-state laser oscillators: a success story for the last 20 years with no end in sight.
Applied Physics B **100**, 15–28 (2010).
URL `http://dx.doi.org/10.1007/s00340-010-4045-3`.

[53] J.-C. Diels and W. Rudolph.
6 - Ultrashort Sources II: Examples.
In J.-C. Diels and W. Rudolph (Eds.), *Ultrashort Laser Pulse Phenomena (Second Edition)*, second edition edition, pp. 341 – 394. Academic Press, Burlington (2006).
URL `http://www.sciencedirect.com/science/article/pii/B9780122154935500070`.

[54] D. E. Spence, P. N. Kean, and W. Sibbett.
60-fsec pulse generation from a self-mode-locked Ti:sapphire laser.
Opt. Lett. **16**, 42–44 (Jan 1991).
URL `http://ol.osa.org/abstract.cfm?URI=ol-16-1-42`.

[55] R. W. Boyd.
Chapter 4 - The Intensity-Dependent Refractive Index.
In R. W. Boyd (Ed.), *Nonlinear Optics (Third Edition)*, third edition edition, pp. 207 – 252. Academic Press, Burlington (2008).

URL http://www.sciencedirect.com/science/article/pii/B9780123694706000046.

[56] R. W. Boyd.
Chapter 7 - Processes Resulting from the Intensity-Dependent Refractive Index.
In R. W. Boyd (Ed.), *Nonlinear Optics (Third Edition)*, third edition edition, pp. 329 – 390. Academic Press, Burlington (2008).
URL http://www.sciencedirect.com/science/article/pii/B9780123694706000071.

[57] M. Terazima.
Ultrafast transient Kerr lens in solution detected by the dual-beamthermal-lens method.
Opt. Lett. **20**, 25–27 (Jan 1995).
URL http://ol.osa.org/abstract.cfm?URI=ol-20-1-25.

[58] L. Fechner.
High resolution experiments on strong-field ionization of atoms and molecules: test of tunneling theory, the role of doubly excited states, and channel-selective electron spectra.
Ph.D. thesis, Universität Heidelberg (2014).

[59] R. L. Fork, O. E. Martinez, and J. P. Gordon.
Negative dispersion using pairs of prisms.
Opt. Lett. **9**, 150–152 (May 1984).
URL http://ol.osa.org/abstract.cfm?URI=ol-9-5-150.

[60] R. Szipöcs, C. Spielmann, F. Krausz, and K. Ferencz.
Chirped multilayer coatings for broadband dispersion control in femtosecond lasers.
Opt. Lett. **19**, 201–203 (Feb 1994).
URL http://ol.osa.org/abstract.cfm?URI=ol-19-3-201.

[61] P. A. Franken, A. E. Hill, C. W. Peters, and G. Weinreich.
Generation of Optical Harmonics.
Phys. Rev. Lett. **7**, 118–119 (Aug 1961).
URL http://link.aps.org/doi/10.1103/PhysRevLett.7.118.

[62] R. W. Boyd.
Chapter 1 - The Nonlinear Optical Susceptibility.
In R. W. Boyd (Ed.), *Nonlinear Optics (Third Edition)*, third edition edition, pp. 1 – 67. Academic Press, Burlington (2008).
URL http://www.sciencedirect.com/science/article/pii/B9780123694706000010.

[63] M. Bass, P. A. Franken, J. F. Ward, and G. Weinreich.
Optical Rectification.
Phys. Rev. Lett. **9**, 446–448 (Dec 1962).
URL https://link.aps.org/doi/10.1103/PhysRevLett.9.446.

[64] R. W. Boyd.
Chapter 2 - Wave-Equation Description of Nonlinear Optical Interactions.

In R. W. Boyd (Ed.), *Nonlinear Optics (Third Edition)*, third edition edition, pp. 69 – 133. Academic Press, Burlington (2008).
URL http://www.sciencedirect.com/science/article/pii/B9780123694706000022.

[65] D. Poelman and P. F. Smet.
Methods for the determination of the optical constants of thin films from single transmission measurements: a critical review.
Journal of Physics D: Applied Physics **36**, 1850 (2003).
URL http://stacks.iop.org/0022-3727/36/i=15/a=316.

[66] K. Kato, N. Umemura, and T. Mikami.
Sellmeier and thermo-optic dispersion formulas for β-BaB_2O_4 (revisited).
In P. E. Powers (Ed.), *Nonlinear Frequency Generation and Conversion: Materials, Devices, and Applications IX*, volume 7582 of *Proceedings of SPIE*, pp. 75821L–1–75821L–6 (2010).
URL http://dx.doi.org/10.1117/12.841913.

[67] M. Hobden and J. Warner.
The temperature dependence of the refractive indices of pure lithium niobate.
Physics Letters **22**, 243 – 244 (1966).
URL http://www.sciencedirect.com/science/article/pii/0031916366905919.

[68] A. Einstein.
Über einen die Erzeugung und Verwandlung des Lichtes betreffenden heuristischen Gesichtspunkt.
Annalen der Physik **322**, 132–148 (1905).
URL http://dx.doi.org/10.1002/andp.19053220607.

[69] M. Protopapas, C. H. Keitel, and P. L. Knight.
Atomic physics with super-high intensity lasers.
Reports on Progress in Physics **60**, 389 (1997).
URL http://stacks.iop.org/0034-4885/60/i=4/a=001.

[70] F. Fabre, G. Petite, P. Agostini, and M. Clement.
Multiphoton above-threshold ionisation of xenon at 0.53 *and* 1.06 μm.
Journal of Physics B: Atomic and Molecular Physics **15**, 1353 (1982).
URL http://stacks.iop.org/0022-3700/15/i=9/a=012.

[71] P. Agostini, F. Fabre, G. Mainfray, G. Petite, and N. K. Rahman.
Free-Free Transitions Following Six-Photon Ionization of Xenon Atoms.
Phys. Rev. Lett. **42**, 1127–1130 (Apr 1979).
URL
http://link.aps.org/doi/10.1103/PhysRevLett.42.1127.

[72] R. R. Freeman, P. H. Bucksbaum, H. Milchberg, S. Darack, D. Schumacher, and M. E. Geusic.
Above-threshold ionization with subpicosecond laser pulses.
Phys. Rev. Lett. **59**, 1092–1095 (Sep 1987).
URL
http://link.aps.org/doi/10.1103/PhysRevLett.59.1092.

[73] E. Mevel, P. Breger, R. Trainham, G. Petite, P. Agostini, J. P. Chambaret,
A. Migus, and A. Antonetti.
Contrasted behaviour of Stark-induced resonances in multiphoton ionization of krypton.
Journal of Physics B: Atomic, Molecular and Optical Physics **25**, L401 (1992).
URL http://stacks.iop.org/0953-4075/25/i=17/a=001.

[74] A. M. Perelomov, V. S. Popov, and M. V. Terent'ev.
Ionization of atoms in an alternating electric field.
Soviet Physics JETP **23**, 924–934 (1966).
URL http:
//www.jetp.ac.ru/cgi-bin/e/index/e/23/5/p924?a=list.

[75] A. M. Perelomov, V. S. Popov, and M. V. Terent'ev.
Ionization of atoms in an alternating electric field II.
Soviet Physics JETP **24**, 207–217 (1967).
URL http:
//www.jetp.ac.ru/cgi-bin/e/index/e/24/1/p207?a=list.

[76] A. M. Perelomov and V. S. Popov.
Ionization of atoms in an alternating electric field III.
Soviet Physics JETP **25**, 336–343 (1967).
URL http:
//www.jetp.ac.ru/cgi-bin/e/index/e/25/2/p336?a=list.

[77] V. S. Popov.
Tunnel and multiphoton ionization of atoms and ions in a strong laser field (Keldysh theory).
Physics-Uspekhi **47**, 855 (2004).
URL http://stacks.iop.org/1063-7869/47/i=9/a=R01.

[78] W. Becker, X. Liu, P. J. Ho, and J. H. Eberly.
Theories of photoelectron correlation in laser-driven multiple atomic ionization.
Rev. Mod. Phys. **84**, 1011–1043 (Jul 2012).
URL http://link.aps.org/doi/10.1103/RevModPhys.84.1011.

[79] P. B. Corkum, N. H. Burnett, and F. Brunel.
Above-threshold ionization in the long-wavelength limit.
Phys. Rev. Lett. **62**, 1259–1262 (Mar 1989).
URL
http://link.aps.org/doi/10.1103/PhysRevLett.62.1259.

[80] G. G. Paulus, W. Becker, W. Nicklich, and H. Walther.
Rescattering effects in above-threshold ionization: a classical model.
Journal of Physics B: Atomic, Molecular and Optical Physics **27**, L703 (1994).
URL http://stacks.iop.org/0953-4075/27/i=21/a=003.

[81] A. N. Pfeiffer, C. Cirelli, A. S. Landsman, M. Smolarski, D. Dimitrovski, L. B.
Madsen, and U. Keller.
Probing the Longitudinal Momentum Spread of the Electron Wave Packet at the Tunnel Exit.

Phys. Rev. Lett. **109**, 083002 (Aug 2012).
URL
http://link.aps.org/doi/10.1103/PhysRevLett.109.083002.

[82] C. Hofmann, A. S. Landsman, C. Cirelli, A. N. Pfeiffer, and U. Keller.
Comparison of different approaches to the longitudinal momentum spread after tunnel ionization.
Journal of Physics B: Atomic, Molecular and Optical Physics **46**, 125601 (2013).
URL http://stacks.iop.org/0953-4075/46/i=12/a=125601.

[83] W. Becker and H. Rottke.
Many-electron strong-field physics.
Contemporary Physics **49**, 199–223 (2008).
URL http://dx.doi.org/10.1080/00107510802332908.

[84] B. Feuerstein, R. Moshammer, and J. Ullrich.
Nonsequential multiple ionization in intense laser pulses: interpretation of ion momentum distributions within the classical 'rescattering' model.
Journal of Physics B: Atomic, Molecular and Optical Physics **33**, L823 (2000).
URL http://stacks.iop.org/0953-4075/33/i=21/a=105.

[85] G. G. Paulus and H. Walther.
The Classical and the Quantum Face of Above-Threshold Ionization.
In D. Batani, C. J. Joachain, S. Martellucci, and A. N. Chester (Eds.), *Atoms, Solids, and Plasmas in Super-Intense Laser Fields*, chapter 15, pp. 285–301.
Springer US, Boston, MA (2001).
URL http://dx.doi.org/10.1007/978-1-4615-1351-3_15.

[86] P. Agostini and L. F. DiMauro.
The physics of attosecond light pulses.
Reports on Progress in Physics **67**, 813 (2004).
URL http://stacks.iop.org/0034-4885/67/i=6/a=R01.

[87] S. L. Miller and H. C. Urey.
Organic Compound Synthesis on the Primitive Earth.
Science **130**, 245–251 (1959).
URL http://science.sciencemag.org/content/130/3370/245.

[88] X. Liu and D. E. Shemansky.
Analysis of electron impact ionization properties of methane.
Journal of Geophysical Research: Space Physics **111**, n/a–n/a (2006).
URL http://dx.doi.org/10.1029/2005JA011454.
A04303.

[89] S. M. Hörst, R. V. Yelle, A. Buch, N. Carrasco, G. Cernogora, O. Dutuit, E. Quirico, E. Sciamma-O'Brien, M. A. Smith, Á. Somogyi, C. Szopa, R. Thissen, and V. Vuitton.
Formation of Amino Acids and Nucleotide Bases in a Titan Atmosphere Simulation Experiment.
Astrobiology **12**, 809–817 (sep 2012).
URL http://online.liebertpub.com/doi/abs/10.1089/ast.2011.0623.

[90] M. A. K. Khalil.
Non-CO$_2$ Greenhouse Gases in The Atmosphere.
Annual Review of Energy and the Environment **24**, 645–661 (1999).
URL http://dx.doi.org/10.1146/annurev.energy.24.1.645.

[91] L. Pauling.
The nature of the chemical bond. Application of results obtained from the quantum mechanics and from a theory of paramagnetic susceptibility to the structure of molecules.
Journal of the American Chemical Society **53**, 1367–1400 (1931).
URL http://dx.doi.org/10.1021/ja01355a027.

[92] S. Hood, E. Weigold, I. McCarthy, and P. Teubner.
Momentum Space Wave Functions and Binding Energies of the Valence Electrons in Methane measured by the (e,2e) Technique.
Nature-Physical Science **245**, 65–68 (1973).
URL http://www.nature.com/nature-physci/journal/v245/n144/abs/physci245065a0.html.

[93] M. van der Wiel, W. Stoll, A. Hamnett, and C. Brion.
Partial oscillator strengths (25 - 50 eV) of the one-electron states of CH$_4^+$, measured in an (e, 2e) experiment.
Chemical Physics Letters **37**, 240 – 242 (1976).
URL http://www.sciencedirect.com/science/article/pii/0009261476802060.

[94] S. Clark, T. Reddish, C. Brion, E. Davidson, and R. Frey.
The valence orbital momentum distributions and binding energy spectra of methane by electron momentum spectroscopy: Quantitative comparisons using near Hartree-Fock limit and correlated wavefunctions.
Chemical Physics **143**, 1 – 10 (1990).
URL http://www.sciencedirect.com/science/article/pii/030101049085001D.

[95] F. Wang.
Molecular orbitals of methane: symmetry or hybridization?
Journal of Molecular Structure: THEOCHEM **678**, 105 – 111 (2004).
URL http://www.sciencedirect.com/science/article/pii/S0166128004001721.

[96] O. Dutuit, M. Aït-Kaci, J. Lemaire, and M. Richard-Viard.
Dissociative Photoionisation of Methane and its Deuterated Compounds in the A State Region.
Physica Scripta **1990**, 223 (1990).
URL http://stacks.iop.org/1402-4896/1990/i=T31/a=030.

[97] J. W. Rabalais, T. Bergmark, L. O. Werme, L. Karlsson, and K. Siegbahn.
The Jahn-Teller Effect in the Electron Spectrum of Methane.
Physica Scripta **3**, 13 (1971).
URL http://stacks.iop.org/1402-4896/3/i=1/a=004.

[98] A. W. Potts and W. C. Price.
The Photoelectron Spectra of Methane, Silane, Germane and Stannane.
Proceedings of the Royal Society of London A: Mathematical, Physical and
Engineering Sciences **326**, 165–179 (1972).
URL http:
//rspa.royalsocietypublishing.org/content/326/1565/165.

[99] L. B. Knight, J. Steadman, D. Feller, and E. R. Davidson.
*Experimental Evidence for a C_{2v} ($^2B_1$) Ground-State Structure of the Methane
Cation Radical: ESR and ab Initio CI Investigations $CH_4{}^+$ and $CD_2H_2{}^+$ in Neon
Matrices at* 4 K.
Journal of the American Chemical Society **106**, 3700–3701 (1984).
URL http://dx.doi.org/10.1021/ja00324a066.

[100] M. N. Paddon-Row, D. J. Fox, J. A. Pople, K. N. Houk, and D. W. Pratt.
*Dynamic Jahn-Teller Effects in $CH_4{}^+$. Location of the Transition Structures for
Hydrogen Scrambling and Inversion.*
Journal of the American Chemical Society **107**, 7696–7700 (1985).
URL http://dx.doi.org/10.1021/ja00311a078.

[101] Z. Vager, E. P. Kanter, G. Both, P. J. Cooney, A. Faibis, W. Koenig, B. J.
Zabransky, and D. Zajfman.
Direct Determination of the Stereochemical Structure of $CH_4{}^+$.
Phys. Rev. Lett. **57**, 2793–2795 (Dec 1986).
URL
https://link.aps.org/doi/10.1103/PhysRevLett.57.2793.

[102] R. J. Boyd, K. V. Darvesh, and P. D. Fricker.
Energy component analysis of the Jahn-Teller effect in the methane radical cation.
The Journal of Chemical Physics **94**, 8083–8088 (1991).
URL http://dx.doi.org/10.1063/1.460142.

[103] A. M. Velasco, J. Pitarch-Ruiz, A. M. J. S. de Merás, J. Sánchez-Marín, and
I. Martin.
*Lower Rydberg series of methane: A combined coupled cluster linear response
and molecular quantum defect orbital calculation.*
The Journal of Chemical Physics **124**, 124313 (2006).
URL http://dx.doi.org/10.1063/1.2179069.

[104] M. Carlsson Göthe, B. Wannberg, L. Karlsson, S. Svensson, P. Baltzer, F. T. Chau,
and M.-Y. Adam.
*X-ray, ultraviolet, and synchrotron radiation excited inner-valence photoelectron
spectra of CH_4.*
The Journal of Chemical Physics **94**, 2536–2542 (1991).
URL http://dx.doi.org/10.1063/1.459880.

[105] J. W. Au, G. Cooper, G. R. Burton, T. N. Olney, and C. Brion.
*The valence shell photoabsorption of the linear alkanes, C_nH_{2n+2} (n=1 - 8):
absolute oscillator strengths (7 - 220 eV).*
Chemical Physics **173**, 209 – 239 (1993).

URL `http://www.sciencedirect.com/science/article/pii/030101049380142V`.

[106] K. Furuya, K. Kimura, Y. Sakai, T. Takayanagi, and N. Yonekura.
Dissociation dynamics of CH_4^+ core ion in the $^2A_1$ state.
The Journal of Chemical Physics **101**, 2720–2728 (1994).
URL `http://dx.doi.org/10.1063/1.467653`.

[107] K. Furuya, K. Ishikawa, and T. Ogawa.
Mass analysis of polyatomic high-Rydberg fragments produced by electron impact on methane.
Chemical Physics Letters **319**, 335 – 340 (2000).
URL `http://www.sciencedirect.com/science/article/pii/S00009261400001494`.

[108] R. Moshammer, M. Unverzagt, W. Schmitt, J. Ullrich, and H. Schmidt-Böcking.
A 4π recoil-ion electron momentum analyzer: a high-resolution "microscope" for the investigation of the dynamics of atomic, molecular and nuclear reactions.
Nuclear Instruments and Methods in Physics Research Section B: Beam Interactions with Materials and Atoms **108**, 425 – 445 (1996).
URL `http://www.sciencedirect.com/science/article/pii/0168583X95012591`.

[109] N. Camus.
Non-sequential double ionization of atoms with phase-controlled ultra-short laser pulses.
Ph.D. thesis, Universität Heidelberg (2013).

[110] O. Svelto.
Solid-State, Dye, and Semiconductor Lasers, chapter 9, pp. 375–430.
Springer US, Boston, MA (2010).
URL `http://dx.doi.org/10.1007/978-1-4419-1302-9_9`.

[111] A. Stingl, R. Szipöcs, M. Lenzner, C. Spielmann, and F. Krausz.
Sub-10-fs mirror-dispersion-controlled Ti:sapphire laser.
Opt. Lett. **20**, 602–604 (Mar 1995).
URL `http://ol.osa.org/abstract.cfm?URI=ol-20-6-602`.

[112] D. Strickland and G. Mourou.
Compression of amplified chirped optical pulses.
Optics Communications **56**, 219 – 221 (1985).
URL `http://www.sciencedirect.com/science/article/pii/0030401885901208`.

[113] C. Spielmann, M. Lenzner, F. Krausz, and R. Szipöcs.
Compact, high-throughput expansion-compression scheme for chirped pulse amplification in the 10 fs range.
Optics Communications **120**, 321 – 324 (1995).
URL `http://www.sciencedirect.com/science/article/pii/003040189500494S`.

[114] S. Sartania, Z. Cheng, M. Lenzner, G. Tempea, C. Spielmann, F. Krausz, and K. Ferencz.
Generation of 0.1-TW 5-fs optical pulses at a 1-kHz repetition rate.
Opt. Lett. **22**, 1562–1564 (Oct 1997).
URL http://ol.osa.org/abstract.cfm?URI=ol-22-20-1562.

[115] T. Ergler.
Zeitaufgelöste Untersuchungen zur Fragmentationsdynamik von H_2 (D_2) in ultra-kurzen Laserpulsen.
Ph.D. thesis, Universität Heidelberg (2006).

[116] A. Krupp.
Two-color pump-probe experiments on single and double ionization of noble gas atoms in strong laser fields.
Master's thesis, University of Heidelberg (2013).

[117] R. Moshammer, D. Fischer, and H. Kollmus.
Recoil-Ion Momentum Spectroscopy and "Reaction Microscopes".
In J. Ullrich and V. Shevelko (Eds.), *Many-Particle Quantum Dynamics in Atomic and Molecular Fragmentation*, volume 35 of *Springer Series on Atomic, Optical, and Plasma Physics*, chapter 2, pp. 33–58. Springer Berlin Heidelberg (2003).
URL http://link.springer.com/chapter/10.1007/978-3-662-08492-2_2.

[118] D. R. Miller.
Free Jet Sources.
In G. Scoles (Ed.), *Atomic and Molecular Beam Methods*, volume 1, chapter 2, pp. 14–53. Oxford University Press, New York, Oxford (1988).

[119] H. Schmidt, H. Cederquist, R. Schuch, L. Bagge, A. Källberg, J. Hilke, K.-G. Rensfelt, V. Mergel, M. Achler, R. Dörner, L. Spielberger, O. Jagutzki, H. Schmidt-Böcking, J. Ullrich, H. Reich, M. Unverzagt, W. Schmitt, and R. Moshammer.
A design study for an internal gas-jet target for the heavy-ion storage ring CRYRING.
Hyperfine Interactions **108**, 339–354 (1997).
URL http://dx.doi.org/10.1023/A:1012635418262.

[120] M. Laux.
Construction and characterization of a new Reaction Microscope.
Diploma thesis, Universität Heidelberg (2011).

[121] R. Moshammer, J. Ullrich, M. Unverzagt, W. Schmidt, P. Jardin, R. E. Olson, R. Mann, R. Dörner, V. Mergel, U. Buck, and H. Schmidt-Böcking.
Low-Energy Electrons and Their Dynamical Correlation with Recoil Ions for Single Ionization of Helium by Fast, Heavy-Ion Impact.
Phys. Rev. Lett. **73**, 3371–3374 (Dec 1994).
URL
http://link.aps.org/doi/10.1103/PhysRevLett.73.3371.

[122] RoentDek Handels GmbH.

MCP Delay Line Detector Manual (Version 11.0.1601.1) (January 2016).
URL `http://www.roentdek.com/manuals/MCP%20Delay%20Line%20manual.pdf`.

[123] Q. Zhang, K. Zhao, and Z. Chang.
Determining time resolution of microchannel plate detectors for electron time-of-flight spectrometers.
Review of Scientific Instruments **81** (2010).
URL `http://scitation.aip.org/content/aip/journal/rsi/81/7/10.1063/1.3463690`.

[124] J. L. Wiza.
Microchannel plate detectors.
Nuclear Instruments and Methods **162**, 587 – 601 (1979).
URL `http://www.sciencedirect.com/science/article/pii/0029554X79907341`.

[125] J. T. Baines, C. D. Garner, S. S. Hasnain, and C. Morrell.
A detection system for fluorescence EXAFS at the SRS wiggler beam line.
Nuclear Instruments and Methods in Physics Research Section A: Accelerators, Spectrometers, Detectors and Associated Equipment **246**, 565 – 568 (1986).
URL `http://www.sciencedirect.com/science/article/pii/0168900286901543`.

[126] H. Keller, G. Klingelhöfer, and E. Kankeleit.
A position sensitive microchannelplate detector using a delay line readout anode.
Nuclear Instruments and Methods in Physics Research Section A: Accelerators, Spectrometers, Detectors and Associated Equipment **258**, 221 – 224 (1987).
URL `http://www.sciencedirect.com/science/article/pii/0168900287900593`.

[127] S. E. Sobottka and M. B. Williams.
Delay line readout of microchannel plates.
IEEE Transactions on Nuclear Science **35**, 348–351 (Feb 1988).
URL `http://ieeexplore.ieee.org/xpl/articleDetails.jsp?arnumber=12740`.

[128] J. H. D. Eland.
Simple two-dimensional position sensitive detector with short dead-time for coincidence experiments.
Measurement Science and Technology **5**, 1501 (1994).
URL `http://stacks.iop.org/0957-0233/5/i=12/a=011`.

[129] O. Jagutzki, A. Cerezo, A. Czasch, R. Dörner, M. Hattass, M. Huang, V. Mergel, U. Spillmann, K. Ullmann-Pfleger, T. Weber, H. Schmidt-Böcking, and G. Smith.
Multiple hit read-out of a microchannel plate detector with a three-layer delay-line anode.
In *Nuclear Science Symposium Conference Record, 2001 IEEE*, volume 2, pp. 850–854 vol.2 (Nov 2001).
URL `http://ieeexplore.ieee.org/xpls/abs_all.jsp?arnumber=1009689&tag=1`.

[130] V. Mergel, O. Jagutzki, L. Spielberger, K. Ullmann-Pfleger, R. Dörner, and
H. Schmidt-Böcking.
Particle and UV-Imaging with Position Sensitive
MCP-Detectors-Three-Dimensional Momentum Space Imaging.
In *Symposium II – In Situ Process Diagnostics & Intelligent Materials Processing*,
volume 502 of *MRS Proceedings*, pp. 171–176 (1997).
URL `http:`
`//journals.cambridge.org/article_S1946427400246216`.

[131] RoentDek Handels GmbH.
The fADC8 fast sampling ADC unit.
URL `http://www.roentdek.com/products/electronics_`
`description/fADC8%20%20description.pdf`.

[132] X. Ren, T. Pflüger, M. Weyland, W. Y. Baek, H. Rabus, J. Ullrich, and A. Dorn.
An (e, 2e + ion) study of low-energy electron-impact ionization and fragmentation
of tetrahydrofuran with high mass and energy resolutions.
The Journal of Chemical Physics **141** (2014).
URL `http://scitation.aip.org/content/aip/journal/jcp/`
`141/13/10.1063/1.4896614`.

[133] D. Fischer.
Aufbau eines Reaktionsmikroskops zur Untersuchung von Ion-Atom-Stößen.
Diploma thesis, Albert-Ludwigs-Universität, Freiburg im Breisgau (2000).

[134] A. Senftleben.
Kinematically complete study on electron impact ionisation of aligned hydrogen
molecules.
Ph.D. thesis, Universität Heidelberg (2009).

[135] C. Ott.
Attosecond multidimensional interferometry of single and two correlated
electrons in atoms.
Ph.D. thesis, Universität Heidelberg (2012).

[136] M. Chini, K. Zhao, and Z. Chang.
The generation, characterization and applications of broadband isolated
attosecond pulses.
Nature Photonics **8**, 178–186 (Mar 2014).
URL `http://www.nature.com/nphoton/journal/v8/n3/full/`
`nphoton.2013.362.html`.

[137] E. Goulielmakis, Z. H. Loh, A. Wirth, R. Santra, N. Rohringer, V. S. Yakovlev,
S. Zherebtsov, T. Pfeifer, A. M. Azzeer, M. F. Kling, S. R. Leone, and F. Krausz.
Real-time observation of valence electron motion.
Nature **466**, 739–743 (2010).
URL `http://www.nature.com/nature/journal/v466/n7307/`
`full/nature09212.html`.

[138] M. Holler, F. Schapper, L. Gallmann, and U. Keller.
Attosecond Electron Wave-Packet Interference Observed by Transient Absorption.

Phys. Rev. Lett. **106**, 123601 (Mar 2011).
URL https://link.aps.org/doi/10.1103/PhysRevLett.106.123601.

[139] U. Fano.
Sullo spettro di assorbimento dei gas nobili presso il limite dello spettro d'arco.
Il Nuovo Cimento (1924-1942) **12**, 154–161 (1935).
URL http://dx.doi.org/10.1007/BF02958288.

[140] U. Fano.
Effects of Configuration Interaction on Intensities and Phase Shifts.
Phys. Rev. **124**, 1866–1878 (Dec 1961).
URL https://link.aps.org/doi/10.1103/PhysRev.124.1866.

[141] M. Hattass, T. Jalowy, A. Czasch, T. Weber, T. Jahnke, S. Schössler, L. P. Schmidt, O. Jagutzki, R. Dörner, and H. Schmidt-Böcking.
A 2π spectrometer for electron-electron coincidence studies on surfaces.
Review of Scientific Instruments **75**, 2373–2378 (2004).
URL http://dx.doi.org/10.1063/1.1765764.

[142] M. Hattass, T. Jahnke, S. Schössler, A. Czasch, M. Schöffler, L. P. H. Schmidt, B. Ulrich, O. Jagutzki, F. O. Schumann, C. Winkler, J. Kirschner, R. Dörner, and H. Schmidt-Böcking.
Dynamics of two-electron photoemission from Cu(111).
Phys. Rev. B **77**, 165432 (Apr 2008).
URL
https://link.aps.org/doi/10.1103/PhysRevB.77.165432.

[143] R. Wallauer, S. Voss, L. Foucar, T. Bauer, D. Schneider, J. Titze, B. Ulrich, K. Kreidi, N. Neumann, T. Havermeier, M. Schöffler, T. Jahnke, A. Czasch, L. Schmidt, A. Kanigel, J. C. Campuzano, H. Jeschke, R. Valenti, A. Müller, G. Berner, M. Sing, R. Claessen, H. Schmidt-Böcking, and R. Dörner.
Momentum spectrometer for electron-electron coincidence studies on superconductors.
Review of Scientific Instruments **83**, 103905 (2012).
URL http://dx.doi.org/10.1063/1.4754470.

[144] K. A. Kouzakov and J. Berakdar.
Photoinduced Emission of Cooper Pairs from Superconductors.
Phys. Rev. Lett. **91**, 257007 (Dec 2003).
URL
https://link.aps.org/doi/10.1103/PhysRevLett.91.257007.

[145] G. Herzberg and C. Jungen.
Rydberg series and ionization potential of the H_2 molecule.
Journal of Molecular Spectroscopy **41**, 425 – 486 (1972).
URL http://www.sciencedirect.com/science/article/pii/0022285272900641.

[146] M. Glass-Maujean, C. Jungen, H. Schmoranzer, I. Haar, A. Knie, P. Reiss, and A. Ehresmann.

The transition probabilities from the ground state to the excited J = 0 $^1\Sigma_u^+$ levels of H$_2$: Measurements and ab initio quantum defect study.
The Journal of Chemical Physics **135**, 144302 (2011).
URL http://dx.doi.org/10.1063/1.3646734.

[147] D. Sprecher, C. Jungen, and F. Merkt.
Determination of the binding energies of the np Rydberg states of H$_2$, HD, and D$_2$ from high-resolution spectroscopic data by multichannel quantum-defect theory.
The Journal of Chemical Physics **140**, 104303 (2014).
URL http://dx.doi.org/10.1063/1.4866809.

[148] W. A. Chupka and J. Berkowitz.
High-Resolution Photoionization Study of the H$_2$ Molecule near Threshold.
The Journal of Chemical Physics **51**, 4244–4268 (1969).
URL http://dx.doi.org/10.1063/1.1671787.

[149] S. Takezawa.
Absorption Spectrum of H$_2$ in the Vacuum-uv Region. I. Rydberg States and Ionization Energies.
The Journal of Chemical Physics **52**, 2575–2590 (1970).
URL http://dx.doi.org/10.1063/1.1673345.

[150] M. Beyer and F. Merkt.
Observation and Calculation of the Quasibound Rovibrational Levels of the Electronic Ground State of H$_2{}^+$.
Phys. Rev. Lett. **116**, 093001 (Feb 2016).
URL https://link.aps.org/doi/10.1103/PhysRevLett.116.093001.

[151] R. S. Berry.
Ionization of Molecules at Low Energies.
The Journal of Chemical Physics **45**, 1228–1245 (1966).
URL http://dx.doi.org/10.1063/1.1727742.

[152] C. Jungen and S. T. Pratt.
Low-energy dissociative recombination in small polyatomic molecules.
The Journal of Chemical Physics **133**, 214303 (2010).
URL http://dx.doi.org/10.1063/1.3518039.

[153] C. R. Brundle, M. B. Robin, and H. Basch.
Electronic Energies and Electronic Structures of the Fluoromethanes.
The Journal of Chemical Physics **53**, 2196–2213 (1970).
URL http://dx.doi.org/10.1063/1.1674313.

[154] W. Kraemer and V. Špirko.
Potential energy function and rotation-vibration energy levels of CH$_3{}^+$.
Journal of Molecular Spectroscopy **149**, 235 – 241 (1991).
URL http://www.sciencedirect.com/science/article/pii/0022285291901554.

[155] A. M. Mebel and S.-H. Lin.

Excited electronic states of the methyl radical. Ab initio molecular orbital study of geometries, excitation energies and vibronic spectra.
Chemical Physics **215**, 329 – 341 (1997).
URL http://www.sciencedirect.com/science/article/pii/S0301010496003631.

[156] T. Mondal and A. J. C. Varandas.
The Jahn-Teller effect in the triply degenerate electronic state of methane radical cation.
The Journal of Chemical Physics **135**, 174304 (2011).
URL http://dx.doi.org/10.1063/1.3658641.

[157] V. Boudon, M. Rey, and M. Loëte.
The vibrational levels of methane obtained from analyses of high-resolution spectra.
Journal of Quantitative Spectroscopy and Radiative Transfer **98**, 394 – 404 (2006).
URL http://www.sciencedirect.com/science/article/pii/S0022407305002608.

[158] A. V. Nikitin, M. Rey, and V. G. Tyuterev.
Rotational and vibrational energy levels of methane calculated from a new potential energy surface.
Chemical Physics Letters **501**, 179 – 186 (2011).
URL http://www.sciencedirect.com/science/article/pii/S0009261410014715.

[159] M. Kato, K. Kameta, T. Odagiri, N. Kouchi, and Y. Hatano.
Single-hole one-electron superexcited states and doubly excited states of methane in the vacuum ultraviolet range as studied by dispersed fluorescence spectroscopy.
Journal of Physics B: Atomic, Molecular and Optical Physics **35**, 4383 (2002).
URL http://stacks.iop.org/0953-4075/35/i=21/a=305.

[160] F. Kong, Q. Luo, H. Xu, M. Sharifi, D. Song, and S. L. Chin.
Explosive photodissociation of methane induced by ultrafast intense laser.
The Journal of Chemical Physics **125**, 133320 (2006).
URL http://dx.doi.org/10.1063/1.2204919.

[161] A. Azarm, H. L. Xu, Y. Kamali, J. Bernhardt, D. Song, A. Xia, Y. Teranishi, S. H. Lin, F. Kong, and S. L. Chin.
Direct observation of super-excited states in methane created by a femtosecond intense laser field.
Journal of Physics B: Atomic, Molecular and Optical Physics **41**, 225601 (2008).
URL http://stacks.iop.org/0953-4075/41/i=22/a=225601.

[162] D. Song, K. Liu, F. Kong, and A. Xia.
Neutral dissociation of methane in the ultra-fast laser pulse.
Chinese Science Bulletin **53**, 1946–1950 (2008).
URL http://dx.doi.org/10.1007/s11434-008-0232-6.

[163] G. Bieri and L. Åsbrink.
30.4-nm He(II) photoelectron spectra of organic molecules.

Journal of Electron Spectroscopy and Related Phenomena **20**, 149 – 167 (1980).
URL `http://www.sciencedirect.com/science/article/pii/0368204880850134`.

[164] I. Cacelli, V. Carravetta, and R. Moccia.
Transition probability and photoionisation cross section calculations for CH$_4$ and HF by one-centre expansion and Stieltjes technique.
Journal of Physics B: Atomic and Molecular Physics **18**, 1375 (1985).
URL `http://stacks.iop.org/0022-3700/18/i=7/a=018`.

[165] Z. Vager, R. Naaman, and E. P. Kanter.
Coulomb Explosion Imaging of Small Molecules.
Science **244**, 426–431 (1989).
URL `http://science.sciencemag.org/content/244/4903/426`.

[166] T. Ding, C. Ott, A. Kaldun, A. Blättermann, K. Meyer, V. Stooss, M. Rebholz, P. Birk, M. Hartmann, A. Brown, H. V. D. Hart, and T. Pfeifer.
Time-resolved four-wave-mixing spectroscopy for inner-valence transitions.
Opt. Lett. **41**, 709–712 (Feb 2016).
URL `http://ol.osa.org/abstract.cfm?URI=ol-41-4-709`.

[167] B. H. Bransden and C. J. Joachain.
Physics of atoms and molecules.
Second edition. Prentice Hall, Harlow (2003).

Danksagung

Zum Abschluss möchte ich herzlich all denjenigen danken, ohne die das Gelingen dieser Arbeit nicht möglich gewesen wäre:

- den Beteiligten an der Kooperation mit der Universität Frankfurt, in deren Rahmen die HHG-Beamline aufgebaut wurde, **Philipp Klaus**, **Maksim Kunitski**, **Robert Wallauer** und **Reinhard Dörner**.

- allen, die hier nicht explizit genannt sind und trotzdem ihren Beitrag zum erfolgreichen Abschluss dieser Arbeit geleistet haben.

Ganz besonders möchte ich meiner Familie und meinen Freunden danken, die mich mein ganzes Leben begleitet und unterstützt haben.